SPIRE HERSCHEL SPACE OBSERVATORY

HERSCHEL EXPLANATORY SUPPLEMENT

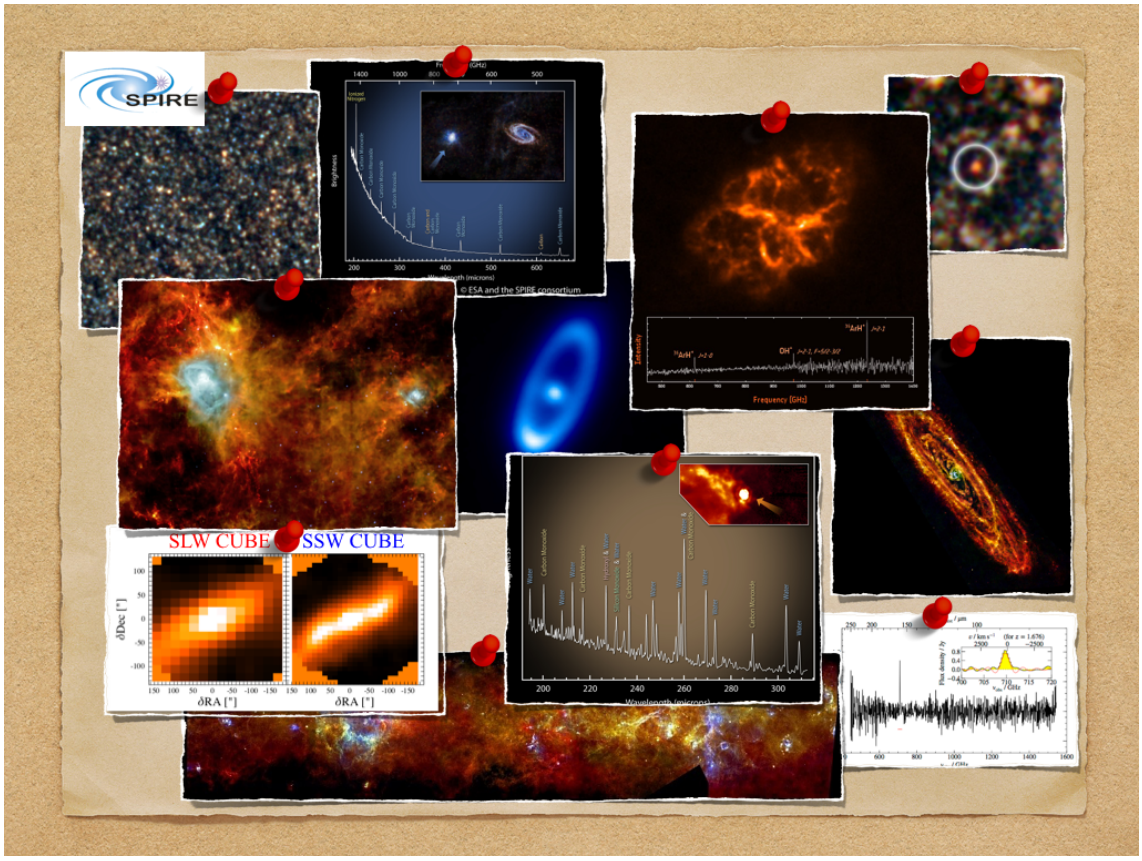

VOLUME IV

THE SPECTRAL AND PHOTOMETRIC IMAGING RECEIVER (SPIRE)

HERSCHEL-DOC-0798, version 3.0, June 3, 2016

SPIRE Handbook

Version 3.0, June 3, 2016

Document editor and custodian: Ivan Valtchanov, Herschel Science Centre, European Space Astronomy Centre, European Space Agency

This document is based on inputs from the SPIRE Consortium and the SPIRE Instrument Control Centre with significant contribution, in alphabetic order, by George Bendo (Manchester), Luca Conversi (ESA), Trevor Fulton (Lethbridge), Matt Griffin (Cardiff), Rosalind Hopwood (Imperial), Sarah Leeks (RAL), Tanya Lim (RAL, ESA), Chris North (Cardiff), Chris Pearson (RAL), Ed Polehampton (RAL), Bernhard Schulz (IPAC) and Bruce Swinyard (RAL).

The name of this document during the active observing phase of *Herschel* was *SPIRE Observers' Manual*. The versioning is continued with the new name.

Contents

Chapter 1

Introduction

1.1 The Observatory

The *Herschel* Space Observatory (Pilbratt et al., 2010) is the fourth cornerstone mission in ESA's science programme. *Herschel* was successfully launched on 14^{th} May 2009 from Kourou, French Guiana, and performed science and engineering observations until 29^{th} Apr 2013 when the liquid Helium coolant boiled off. *Herschel* was in an extended orbit around the second Lagrangian point (L2) of the system Sun-Earth. After the end of operations, with the last command sent on 17^{th} June 2013, the satellite was put into a safe disposal orbit around the Sun. *Herschel* telescope's passively cooled 3.5 m diameter primary mirror is currently the largest one ever flown in space. The three on-board instruments: the Heterodyne Instrument for Far Infrared (HIFI, De Graauw et al. 2010), the Photodetector Array Camera and Spectrometer (PACS, Poglitch et al. 2010) and the Spectral and Photometric Imaging Receiver (SPIRE, Griffin et al. 2010) performed photometry and spectroscopy observations in the infrared and the far-infrared domains, from $\sim$ 60 μm to $\sim$ 700 μm. This spectral domain covers the cold and the dusty universe: from dust-enshrouded galaxies at cosmological distances down to scales of stellar formation, planetary system bodies and our own solar system objects.

A high-level description of the *Herschel* Space Observatory is given in Pilbratt et al. (2010). The first scientific results were presented in 2010 in a special volume 518 of *Astronomy & Astrophysics* journal. More details on the observatory and its instruments are given in the different volumes of the *Herschel* Explanatory Supplement, available from the *Herschel* Science Centre web portal[1], where one can find additional information regarding the latest *Herschel* news, data processing tools, user provided data products, the *Herschel* publications library and access to the *Herschel* Science Archive (HSA).

1.2 Purpose and Structure of Document

The purpose of this handbook is to provide relevant information about the SPIRE instrument, in order to help astronomers understand and use the scientific observations that were performed with it.

The structure of the document is as follows: first we describe the SPIRE instrument (Chapter 2), followed by the description of the observing modes (Chapter 3) and their in-flight performance. The same chapter includes also the SPIRE and PACS Parallel mode and its performance. The SPIRE

[1]The *Herschel* web portal URL is http://www.cosmos.esa.int/web/herschel/home

calibration sources are presented in Chapter 4. The flux calibration scheme for the Photometer is in Chapter 5, where we also describe the framework and practical guidelines for the different conversion factors that are applied to SPIRE timelines and maps. This chapter also includes description of the calibration of SPIRE maps using *Planck*-HFI all sky maps. The Spectrometer calibration is described in Chapter 6. The overall SPIRE sub-instruments calibration accuracies are summarised in Chapter 7. The access to SPIRE observations from the *Herschel* Science Archive are outlined briefly in Chapter 8. The Handbook ends with the Bibliography.

1.3 Acknowledgements

This handbook is provided by the *Herschel Science Centre*, based on inputs by the SPIRE Consortium and by the SPIRE instrument team.

To cite the Handbook please use the following reference:

SPIRE Handbook 2016, Herschel Explanatory Supplement vol. IV, HERSCHEL-HSC-DOC-0798

1.4 Changes to Document

There were significant changes in the structure of the document as well as many corrections to the text with respect to the previous v2.5 from March 2014. The major ones are given below:

- SPIRE and PACS Parallel Mode is now part of this document, section in Chapter 3, presenting the mode and its performance.
- The previous section on "SPIRE in-flight performance" was absorbed in a section at the end of Chapter 3.
- All numbers in the flux calibration chapters 5 & 6 are applicable for the latest SPIRE public calibration tree (spire_cal_14_3, March 2016).
- The calibration targets are now introduced in a separated Chapter 4.
- The Photometer and the spectrometer calibration schemes are split into separate chapters.
- We introduce a short chapter summarising the overall calibration accuracy for both SPIRE instruments. In the same chapter we add a section with a forecast for expected future changes in the calibration.
- The guidelines for derivation of Photometer colour corrections for semi-extended sources in Section 5.8 are provided in more detail, and a link to the available HIPE useful script (as of HIPE v13) is provided.
- In many places we added references to the latest papers on SPIRE calibration, notably those from the special *Herschel* issue of Experimental Astronomy, 2014, Volume 37.
- A new section on *HiRes* maps for the Photometer in Chapter 5.
- New sections in the Spectrometer calibration chapter (Chapter 6):

  - added the framework for correcting spectra of sources that are neither point-like nor fully extended, i.e. semi-extended sources.
  - added the correction for the far-field feedhorn efficiency for extended source calibrated spectra.
  - added the current empirical calibration for low resolution (LR) spectra.

- Previous Chapter 6: *SPIRE data products* was renamed to *SPIRE Observations in the Herschel Science Archive* and provides a short guide on the details on how to get SPIRE data from the *Herschel* science archive.

1.5 List of Acronyms

AOR	Astronomical Observation Request
AOT	Astronomical Observation Template
BSM	Beam Steering Mirror
DCU	Detector Control Unit
DP	Data Processing
DPU	Digital Processing Unit
ESA	European Space Agency
ESAC	European Space Astronomy Centre, based near Madrid, Spain
FCU	FPU Control Unit
FIR	Far Infrared Radiation
FOV	Field of View
FPU	Focal Plane Unit
FTS	Fourier-Transform Spectrometer
HCSS	Herschel Common Software System
HIFI	Heterodyne Instrument for the Far Infrared
HIPE	*Herschel* Interactive Processing Environment
HSA	The *Herschel* Science Archive
HSC	The *Herschel Science Centre* (based in ESAC)
HSpot	*Herschel* Observation Planning Tool
IA	Interactive Analysis
ILT	Instrument Level Test (i.e. ground tests of the instrument without the spacecraft)
ISM	Inter Stellar Medium
JFET	Junction Field-Effect Transistor
LSR	Local Standard of Rest
NEP	Noise-Equivalent Power
OD	Operational Day
OPD	Optical Path Difference
PACS	Photodetector Array Camera and Spectrometer
PCAL	Photometer Calibration Source
PFM	Proto-Flight Model of the instrument
PLW	SPIRE Photometer Long (500 μm) Wavelength Array
PMW	SPIRE Photometer Medium (350 μm) Wavelength Array
PSW	SPIRE Photometer Short (250 μm) Wavelength Array
PTC	Photometer Thermal Control Unit
RMS,*rms*	Root Mean Square
RSRF	Relative Spectral Response Function
SCAL	Spectrometer Calibration Source
SED	Spectral Energy Distribution
SLW	SPIRE Long (294-671 μm, 1018-447 GHz) Wavelength Spectrometer Array
SMEC	Spectrometer Mechanism
SNR, S/N	Signal-to-Noise Ratio
SPG	Standard Product Generation
SPIRE	Spectral and Photometric Imaging REceiver
SSW	SPIRE Short (191-318 μm, 1568-944 GHz) Wavelength Spectrometer Array
ZPD	Zero Path Difference

Chapter 2

The SPIRE Instrument

2.1 Instrument Overview

SPIRE consists of a three-band imaging photometer and an imaging Fourier Transform Spectrometer (FTS). The photometer carries out broad-band photometry ($\lambda/\Delta\lambda \approx 3$) in three spectral bands centred on approximately 250, 350 and 500 μm, and the FTS uses two overlapping bands to cover 191-671 μm (447-1568 GHz).

Figure 2.1 shows a block diagram of the instrument. The SPIRE focal plane unit (FPU) is approximately $700\times400\times400$ mm in size and is supported from the 10 K *Herschel* optical bench by thermally insulating mounts. The FPU contains the optics, detector arrays (three for the photometer, and two for the spectrometer), an internal ^{3}He cooler to provide the required detector operating temperature of $\sim$ 0.3 K, filters, mechanisms, internal calibrators, and housekeeping thermometers. It has three temperature stages: the *Herschel* cryostat provides temperatures of 4.5 K and 1.7 K via high thermal conductance straps to the instrument, and the ^{3}He cooler serves all five detector arrays.

Both the photometer and the FTS have cold pupil stops conjugate with the *Herschel* secondary mirror, which is the telescope system pupil, defining a 3.29 m diameter used portion of the primary. Conical feedhorns (Chattopadhyay et al., 2003) provide a roughly Gaussian illumination of the pupil, with an edge taper of around 8 dB in the case of the photometer. The ^{3}He cooler (Duband et al., 1998), used in both SPIRE and PACS instruments, has two heater-controlled gas gap heat switches. Thus one of its main features is the absence of any moving parts. Liquid confinement in zero-g is achieved by a porous material that holds the liquid by capillary attraction. A Kevlar wire suspension system supports the cooler during launch whilst minimising the parasitic heat load. The cooler contains 6 STP litres of ^{3}He, fits in a $200 \times 100 \times 100$ mm envelope and has a mass of $\sim$ 1.7 kg. Copper straps connect the 0.3-K stage to the five detector arrays, and are held rigidly at various points by Kevlar support modules (Hargrave et al., 2006). The supports at the entries to the 1.7-K boxes are also light-tight.

All five detector arrays use hexagonally close-packed feedhorn-coupled spider-web Neutron Transmutation Doped (NTD) bolometers (Turner et al., 2001). The bolometers are AC-biased with frequency adjustable between 50 and 200 Hz, avoiding 1/f noise from the cold JFET readouts. There are three SPIRE warm electronics units: the Detector Control Unit (DCU) provides the bias and signal conditioning for the arrays and cold electronics, and demodulates and digitises the detector signals; the FPU Control Unit (FCU) controls the cooler and the mechanisms, and reads out all the FPU thermometers;

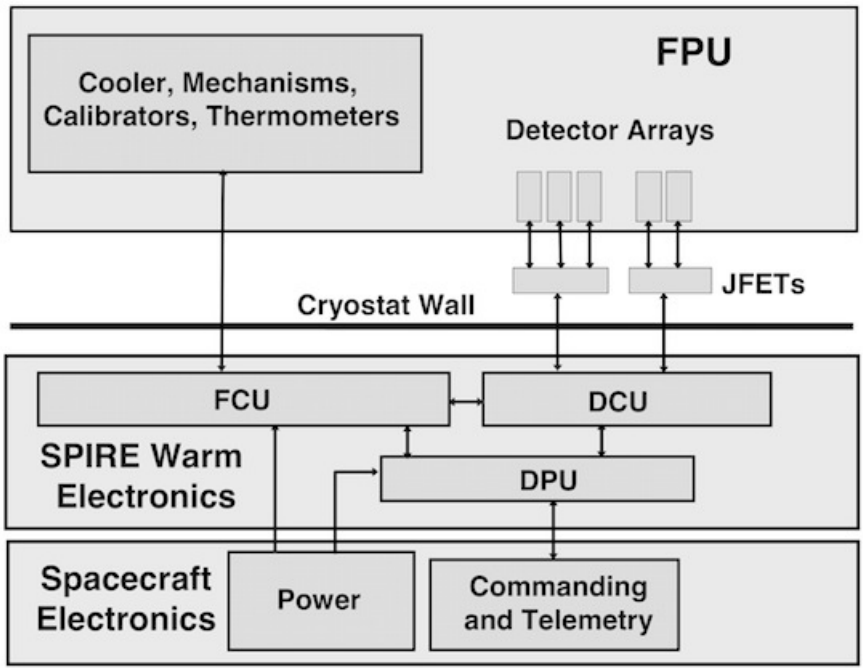

Figure 2.1: SPIRE instrument architecture

and the Digital Processing Unit (DPU) runs the on-board software and interfaces with the spacecraft for commanding and telemetry.

A summary of the most important instrument characteristics is shown in Table 2.1 and the operational parts of SPIRE are presented in the subsequent sections. A more detailed description of SPIRE can be found in Griffin et al. (2010).

SPIRE shares the *Herschel* focal plane with HIFI and PACS and it relative position with respect to the other two instruments is shown in Figure 2.2.

2.2 Photometer design

2.2.1 Optics and layout

The photometer opto-mechanical layout is shown in Figure 2.3. It is an all-reflective design (Dohlen et al. 2000) except for the dichroics used to direct the three bands onto the bolometer arrays, and the filters used to define the passbands (Ade et al. 2006). The input mirror M3, lying below the telescope focus, receives the $f/8.7$ telescope beam and forms an image of the secondary at the flat beam steering mirror (BSM), M4. Mirror M5 converts the focal ratio to $f/5$ and provides an intermediate focus at M6, which re-images the M4 pupil to a cold stop. The input optics are common to the photometer and spectrometer and the separate spectrometer field of view is directed to the other side of the optical bench panel by a pick-off mirror close to M6. The 4.5-K optics are mounted on the SPIRE internal optical bench. Mirrors M7, M8 and a subsequent mirror inside the 1.7-K box form a one-to-one optical relay to bring the M6 focal plane to the detectors. The 1.7-K enclosure also contains the three

Table 2.1: SPIRE overall characteristics.

Sub-instrument	**Photometer**			**Spectrometer**	
Array	**PSW**	**PMW**	**PLW**	**SSW**	**SLW**
Band (μm)	250	350	500	191-318	294-671
Resolution ($\lambda/\Delta\lambda$)	3.3	3.4	2.5	$\sim 40 - 1000$ at 250 μm (variable)[a]	
Unvignetted field of view	$4' \times 8'$			$2.0'$ (diameter)	
Beam FWHM size (arcsec)[b]	17.6	23.9	35.2	16.5-20.5	31.0-42.8

(a) – the spectral resolution can be low (LR, Δf=25 GHz), medium (MR, Δf=7.2 GHz) or high (HR, Δf=1.2 GHz). Only HR and LR were used in science observations. See Section 3.5.3 for details.
(b) – The photometer beam FWHM were measured using fine scan observations of Neptune, on beam maps with $1''$ pixels, see Section 5.9. The FTS beam size depends on wavelength, see Section 6.3 for more details.

detector arrays and two dichroic beam splitters to direct the same field of view onto the arrays so that it can be observed simultaneously in the three bands. The images in each band are diffraction-limited over the $4' \times 8'$ field of view.

2.2.2 Beam steering mirror (BSM)

The BSM (M4 in Figure 2.3) is located in the optical path before any subdivision of the incident radiation into photometer and spectrometer optical chains, and is used both for photometer and FTS observations. For photometric observations the BSM is moved on a pattern around the nominal position of the source. For the FTS, the BSM is moved on a specific pattern to create intermediate or fully sampled spectral maps. It can chop up to $\pm 2'$along the long axis of the Photometer's $4' \times 8'$ field of view and simultaneously chop in the orthogonal direction by up to $30''$. This two-axis motion allows "jiggling" of the pointing to create fully sampled image of the sky. The nominal BSM chop frequency for the photometer is 1 Hz, however this chop and jiggle mode was never used for science observations. For scanning observations the BSM is kept at its home position.

2.2.3 Filters and passbands

The photometric passbands are defined by quasi-optical edge filters (Ade et al. 2006) located at the instrument input, at the 1.7-K cold stop, and directly in front of the detector arrays, the reflection-transmission edges of the dichroics, and the cut-off wavelengths of the feedhorn output waveguides. The filters also serve to minimise the thermal loads on the 1.7-K and 0.3-K stages. The three bands are centred at approximately 250, 350 and 500 μm and their relative spectral response curves (RSRF) are given in much more detail in Section 5.1 (see Figure 5.1).

2.2.4 Photometer calibration source (PCAL)

PCAL is a thermal source used to provide a repeatable signal for the bolometers (Pisano et al., 2005). It operates as an inverse bolometer: applied electrical power heats up an emitting element to a temperature of around 80 K, causing it to emit FIR radiation, which is seen by the detectors. It is not designed

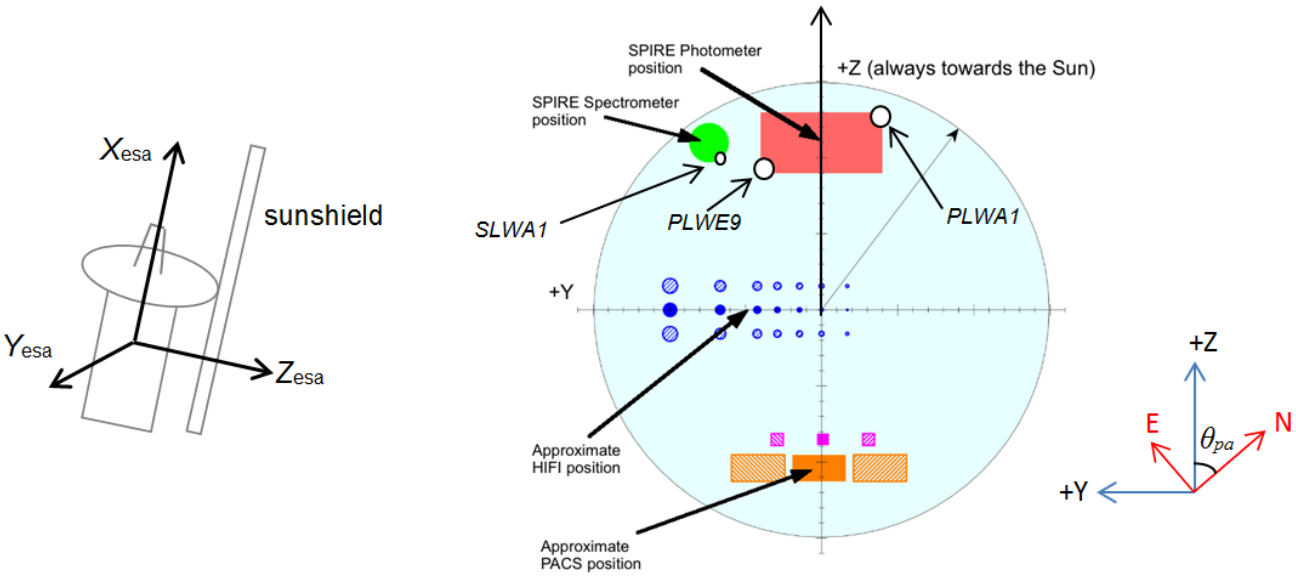

Figure 2.2: SPIRE location on sky with respect to the other two instruments sharing the *Herschel* focal plane. The centre of the SPIRE photometer is offset by $\approx 11'$ from the centre of the highly curved focal surface of the *Herschel* telescope, shown by the large shaded circle. The definition of the spacecraft X, Y, Z axes and position angle, θ_{pa} are also shown. The relative positions of some bolometer detectors from the Photometer (PLWA1 and PLWE9) and from the Spectrometer (SLWA1) are indicated for reference.

to provide an absolute calibration of the system; this will be done by observations of standard astronomical sources. The PCAL radiates through a 2.8 mm hole in the centre of the BSM (occupying an area contained within the region of the pupil obscured by the hole in the primary). Although optimised for the photometer detectors, it can also be viewed by the FTS arrays. PCAL is operated at regular intervals in-flight in order to check the health and the responsivity of the arrays.

2.2.5 Photometer detector arrays

The three arrays contain 139 (250 μm), 88 (350 μm) and 43 (500 μm) detectors, each with their own individual feedhorn. The feedhorn array layouts are shown schematically in Figure 2.4. The design features of the detectors and feedhorns are described in more detail in Section 2.4.1.

The relative merits of feedhorn-coupled detectors, as used by SPIRE, and filled array detectors, which are used by PACS and some ground-based instruments such as SCUBA-2 (Audley et al., 2007) and SHARC-II (Dowell et al., 2003), are discussed in detail in Griffin et al. (2002). In the case of SPIRE, the feedhorn-coupled architecture was chosen as the best option given the achievable sensitivity, the requirements for the largest possible field of view and high stray light rejection, and limitations on the number of detectors imposed by spacecraft resource budgets. The detector feedhorns are designed for maximum aperture efficiency, requiring an entrance aperture close to $2F\lambda$, where λ is the wavelength and F is the final optics focal ratio. This corresponds to a beam spacing on the sky of $2\lambda/D$, where D is the telescope diameter. The array layouts are shown schematically in Figure 2.4, and a photograph of an array module is show in Figure 2.8.

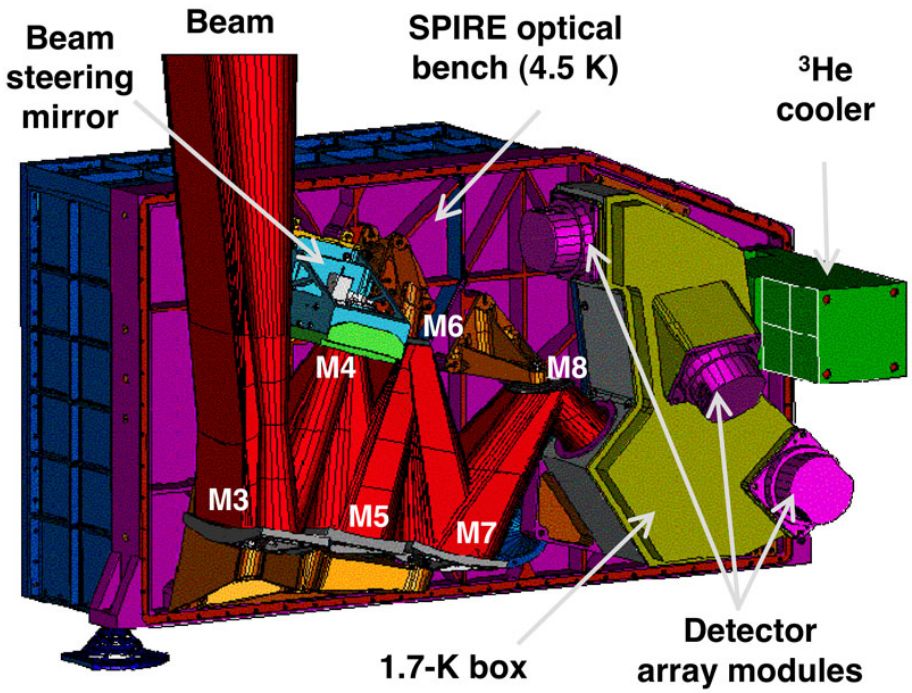

Figure 2.3: SPIRE FPU: photometer side layout.

2.3 Spectrometer design

2.3.1 Fourier-Transform Spectrometer Concept and Mode of Operation

The SPIRE Fourier-Transform Spectrometer (FTS) uses the principle of interferometry: the incident radiation is separated by a beam splitter into two beams that travel different optical paths before recombining. By changing the Optical Path Difference (OPD) of the two beams with a moving mirror, an interferogram of signal versus OPD is created. This interferogram is the Fourier transform of the incident radiation, which includes the combined contribution from the telescope, the instrument and the source spectrum. The signal that is registered by the Spectrometer detectors is not a measurement of the integrated flux density within the passband, like in the case of the Photometer, but rather the Fourier component of the full spectral content. Performing the inverse Fourier transform thus produces a spectrum as a function of the frequency.

The nominal mode of operation of the FTS involves moving the scan mirror continuously (nominally at 0.5 mm s^{-1}, giving an optical path rate of 2 mm s^{-1} due to the factor of four folding in the optics). Radiation frequencies of interest are encoded as detector output electrical frequencies in the range 3-10 Hz. For an FTS, the resolution element in wavenumbers is given by $\Delta\sigma = 1/(2 \times OPD_{max})$, where OPD_{max} is the maximum optical path difference of the scan mirror. In frequency, the resolution element is $\Delta f = c\Delta\sigma$, where c is the speed of light. The maximum mechanical scan length is 3.5 cm, equivalent to an OPD_{max} of 14 cm, hence the highest resolution available is $\Delta\sigma = 0.04$ cm^{-1}, or Δf=1.2 GHz in frequency space. The frequency sampling of the final spectrum can be made arbitrarily small, by zero padding the interferogram before the Fourier transformation, but the number of independent points in the spectrum are separated in frequency space by Δf and

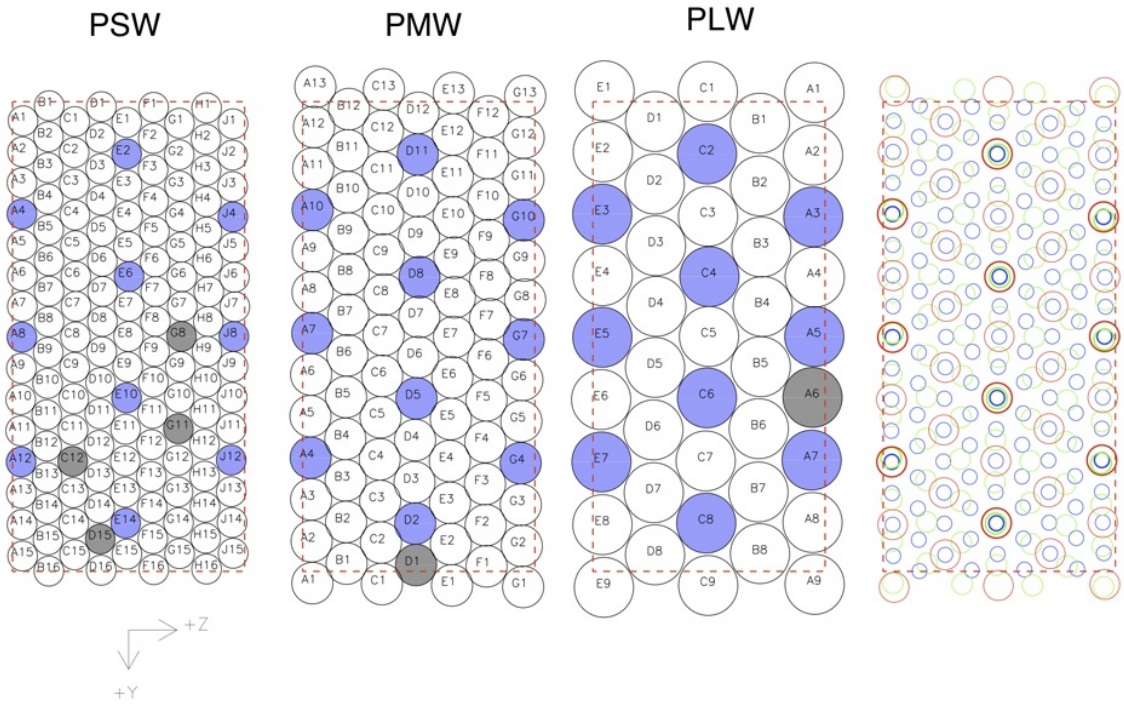

Figure 2.4: A schematic view of the photometer bolometer arrays, the bolometer names are also shown. Each circle represents a detector feedhorn. Those detectors centred on same sky positions are shaded in *blue*, the dead bolometers are shaded in *grey*. The $4' \times 8'$ unvignetted field of view of each array is delineated by a *red* dashed rectangle. The three arrays overlap on the sky as shown in the rightmost figure, where the PLW (500 μm), PMW (350 μm) and PSW (250 μm) are depicted by red, green and blue circles respectively. The circle sizes in the rightmost figure correspond to the FWHM of the beam. The spacecraft coordinate system (Y,Z) is also shown.

this is constant throughout the frequency range from 447-1568 GHz, covered by the FTS.

2.3.2 Spectrometer optics and layout

The FTS (Swinyard et al., 2003; Dohlen et al., 2000) uses two broadband intensity beam splitters in a Mach-Zehnder configuration which has spatially separated input and output ports. This configuration leads to a potential increase in efficiency from 50% to 100% in comparison with a Michelson interferometer. One input port views the $2.6'$ diameter field-of-view on the sky and the other an on-board reference source (SCAL). Two bolometer arrays at the output ports cover overlapping bands of 944-1568 GHz (SSW, 191-318 μm) and 447-1018 GHz (SLW, 294-671 μm). As with any FTS, each scan of the moving mirror produces an interferogram in which the spectrum of the entire band is encoded with the spectral resolution corresponding to the maximum mirror travel.

The FTS focal plane layout is shown in Figure 2.5. A single back-to-back scanning roof-top mirror serves both interferometer arms. It has a frictionless mechanism using double parallelogram linkage and flex pivots, and a Moiré fringe sensing system. A filtering scheme similar to the one used in the photometer restricts the passbands of the detector arrays at the two ports, defining the two overlapping FTS bands.

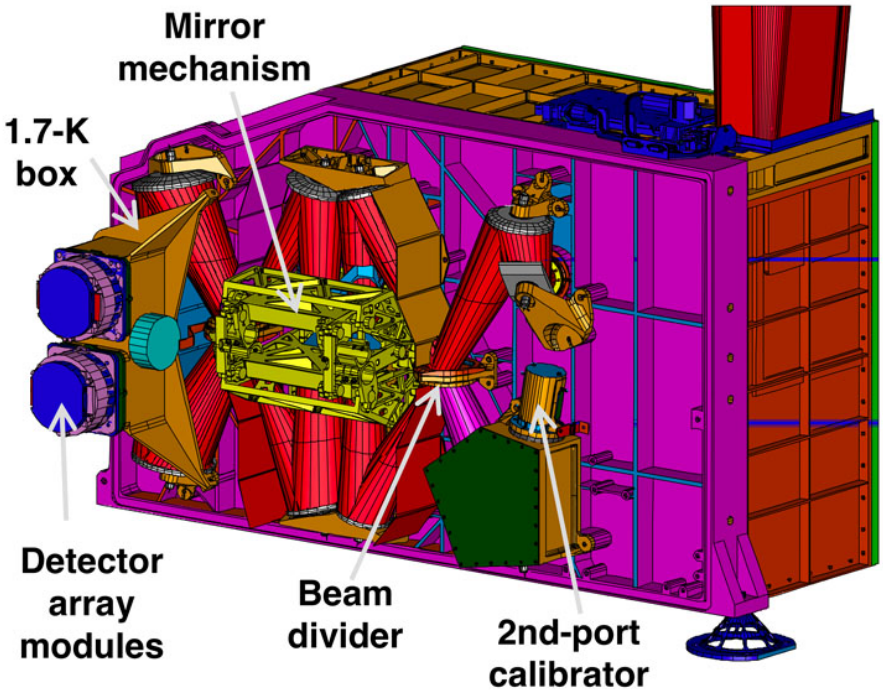

Figure 2.5: SPIRE FPU: spectrometer side layout.

2.3.3 Spectrometer calibration source (SCAL)

A thermal source, the Spectrometer Calibrator (SCAL, Hargrave et al. 2006), is available as an input to the second FTS port to allow the background power from the telescope to be nulled, thus reducing the dynamic range (because the central maximum of the interferogram is proportional to the difference of the power from the two input ports). SCAL is located at the pupil image at the second input port to the FTS, and has two sources which can be used to simulate different possible emissivities of the telescope: 2% and 4%.

The in-flight FTS calibration measurements of Vesta, Neptune and Uranus with SCAL turned off showed that the signal at the peak of the interferogram is not saturated or at most only a few samples are saturated, which means that SCAL is not required to reduce the dynamic range. This is a consequence of the lower emissivity of the telescope and the low straylight in comparison with the models available during the design of the FTS. Using the SCAL adds photon noise to the measurements and it was decided that it will not be used during routine science observations. An additional benefit from having the SCAL off is that it, and the rest of the instrument, are at a temperature between 4.5-5 K and the thermal emission from these components is limited to the low frequencies only detectable in the SLW band[1].

2.3.4 Filters and passbands

The spectral passbands are defined by a sequence of metal mesh filters at various locations and by the waveguide cut-offs and provide two overlapping bands of 944-1568 GHz (SSW) and 447-1018 GHz

[1]The peak emission of a blackbody of $\sim$ 5 K, using Wien's displacement law, is at 500 GHz (600 μm).

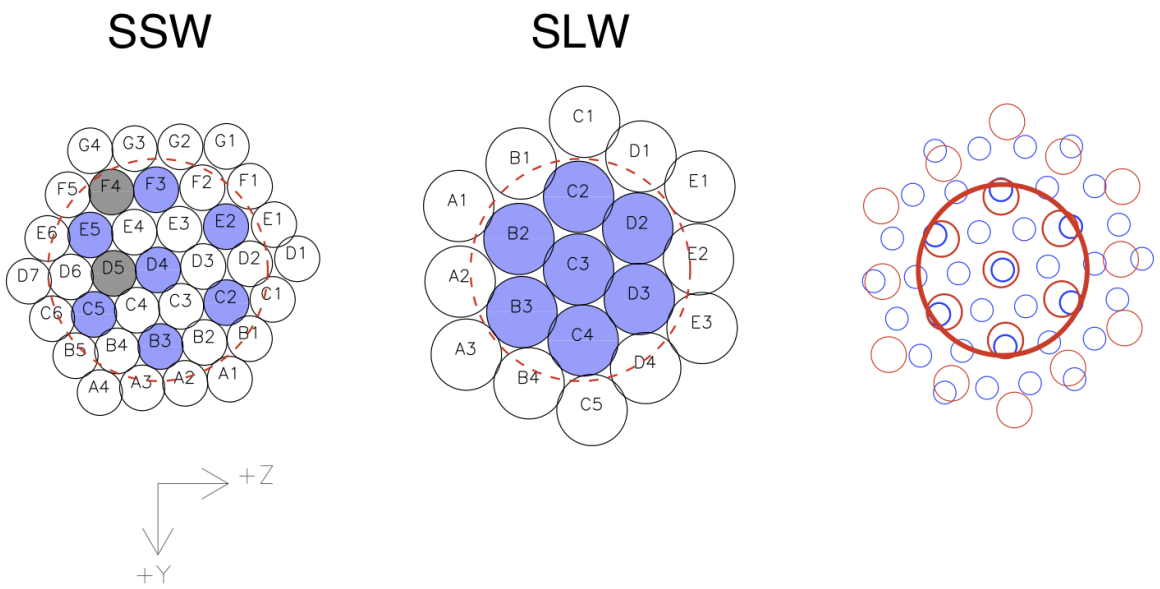

Figure 2.6: A schematic view of the FTS bolometer arrays, the bolometer names are also shown. Each circle represents a detector feedhorn. Those detectors centred on same sky positions are shaded in *blue*, the dead bolometers are shaded in *grey*. The 2.6′ diameter unvignetted field of view of each array is delineated by a *red* dashed circle. The two arrays overlap on the sky as shown in the rightmost figure, where the SLW and SSW are depicted by *red* and *blue* circles respectively. The bold *red* circle delineates the 2′ diameter unvignetted field of view for FTS observations. The circle sizes in the rightmost figure correspond to the FWHM of the beam. The spacecraft coordinate system (Y,Z) is also shown.

(SLW). The spectrometer filters transmissions are not actually used in the spectrometer processing or calibration. More useful information is provided by the relative spectral response functions (RSRF), presented in greater details in Fulton et al. (2014) and in Section 6.

2.3.5 Spectrometer detector arrays

The two spectrometer arrays contain 19 (SLW) and 37 (SSW) hexagonally packed detectors, each with its own individual feedhorn, see Figure 2.6. The array modules are similar to those used for the photometer, with an identical interface to the 1.7-K enclosure. The feedhorn and detector cavity designs are optimised to provide good sensitivity across the whole wavelength range of the FTS. The SSW feedhorns are sized to give $2F\lambda$ spacing at $\lambda = 225\mu$m (1332.4 GHz) and the SLW horns are $2F\lambda$ at $\lambda = 389\mu$m (770.7 GHz). This arrangement has the advantage that there are many co-aligned detectors in the combined field of view. The SSW beams on the sky are 33″ apart, and the SLW beams are separated by 51″. Figure 2.6 also shows the overlap of the two arrays on the sky with circles representing the FWHM of the response of each detector. The unvignetted footprint on the arrays (diameter 2′) contains 7 detectors for SLW and 19 detectors for SSW, outside this circle the data are with higher noise. The design features of the detectors and feedhorns are described in more detail in Section 2.4.1.

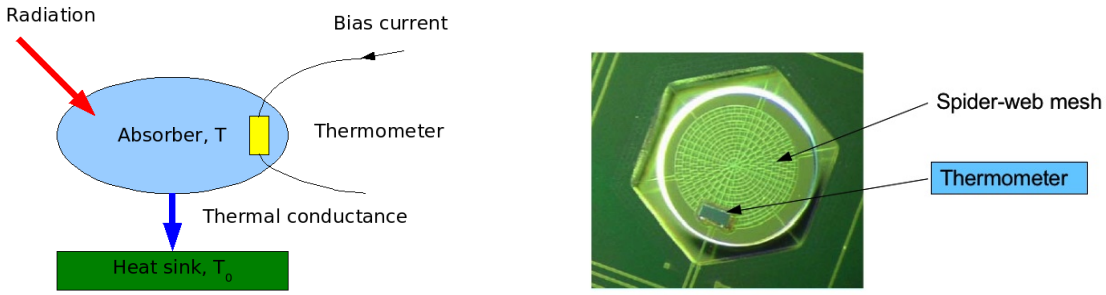

Figure 2.7: Basic principles of bolometer operation (left) and a magnified view of a SPIRE bolometer (right). The thermometer size is 10x100x300 μm.

2.4 Common Instrument Parts

2.4.1 Basic bolometer operations

The SPIRE detectors are semiconductor bolometers for both the photometer and the spectrometer. The general theory of bolometer operation is described in Mather (1982) and Sudiwala et al. (2002), and details of the SPIRE bolometers are given in Turner et al. (2001); Rownd et al. (2003) and Chattopadhyay et al. (2003).

The basic features of a bolometer and the principles of bolometer operation are outlined here, and are illustrated in Figure 2.7. The radiant power to be detected is incident on an absorber of heat capacity C. Heat is allowed to flow from the absorber to a heat sink at a fixed temperature T_0 by a thermal conductance, G (the higher G, the more rapidly the heat leaks away). A thermometer is attached to the absorber, to sense its temperature. A bias current, I, is passed throughout the thermometer, and the corresponding voltage, V, is measured. The bias current dissipates electrical power, which heats the bolometer to a temperature, T, slightly higher than T_0. With a certain level of absorbed radiant power, Q, the absorber will be at some temperature T, dictated by the sum of the radiant and electrical power dissipation. If Q changes, the absorber temperature will change accordingly, leading to a corresponding change in resistance and hence in output voltage.

In the case of the SPIRE detectors, the absorber is a spider-web mesh composed of silicon nitride with a thin resistive metal coating to absorb and thermalise the incident radiation. The thermometers are crystals of Neutron Transmutation Doped (NTD) germanium, which has very high temperature coefficient of resistance. A magnified view of an actual SPIRE bolometer is shown in Figure 2.7, right panel.

The main performance parameters for bolometric detectors are the responsivity ($\mathrm{d}V/\mathrm{d}Q$), the noise-equivalent power (NEP) and the time constant ($\tau \sim C/G$). In order to achieve high sensitivity (low NEP) and good speed of response, operation at low temperature is needed. The photon noise level, arising from unavoidable statistical fluctuations in the amount of background radiation incident on the detector, dictates the required sensitivity. In the case of SPIRE, this radiation is due to thermal emission from the telescope, and results in a photon noise limited NEP on the order of a few $\times 10^{-17}$ W Hz$^{-1/2}$. The bolometers are designed to have an overall NEP dominated by this contribution. To achieve this, the operating temperature for the SPIRE arrays must be of the order of 300 mK.

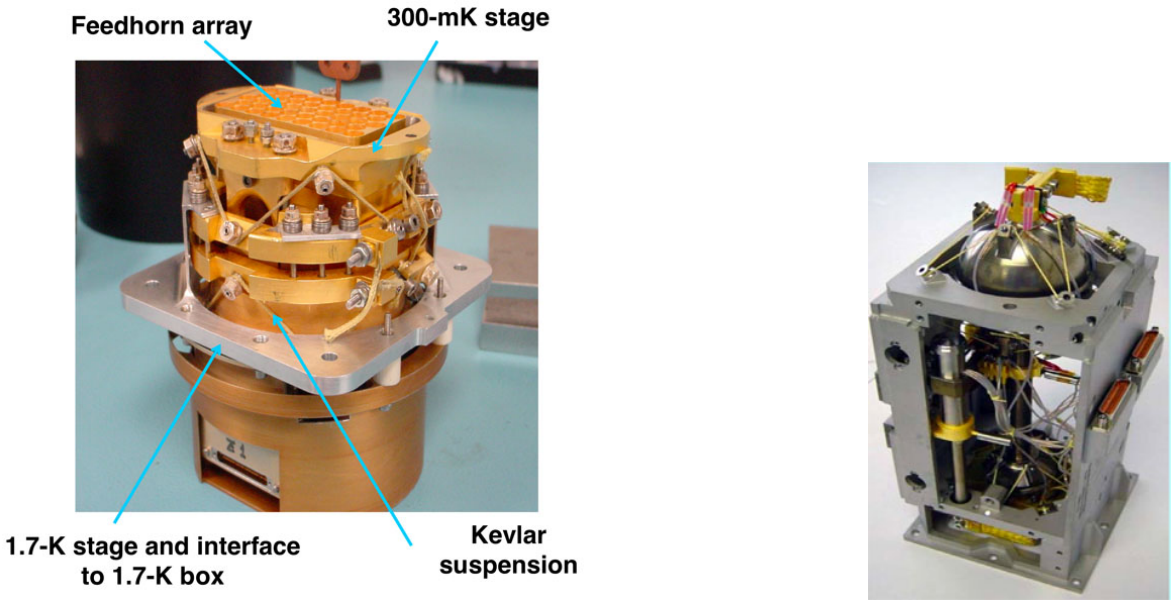

Figure 2.8: Photograph of a SPIRE detector array module (left) and the SPIRE cooler (right).

The operating resistance of the SPIRE bolometers is typically a few MΩ. The outputs are fed to JFETs located as close as possible to the detectors, in order to convert the high-impedance signals to a much lower impedance output capable of being connected to the next stage of amplification by a long cryoharness.

The thermometers are biased by an AC current, at a frequency in the 100-Hz region. This allows the signals to be read out at this frequency, which is higher than the $1/f$ knee frequency of the JFETs, so that the $1/f$ noise performance of the system is limited by the detectors themselves, and corresponds to a knee frequency of around 100 mHz.

The detailed design of the bolometer arrays must be tailored to the background power that they will experience in flight, and to the required speed of response. The individual SPIRE photometer and spectrometer arrays have been optimised accordingly.

The bolometers are coupled to the telescope beam by conical feedhorns located directly in front of the detectors on the ^{3}He stage. Short waveguide sections at the feedhorn exit apertures lead into the detector cavities. The feedhorn entrance aperture diameter is set at $2F\lambda$, where λ is the design wavelength and F is the final optics focal ratio. This provides the maximum aperture efficiency and thus the best possible point source sensitivity (Griffin et al., 2002). In order to achieve the highest packing density possible, the feedhorns are hexagonally close-packed, as shown in the photograph in Figure 2.8 and schematically in Figure 2.4 and Figure 2.6. A centre-centre distance of $2F\lambda$ in the focal plane corresponds to a beam separation on the sky of $2\lambda/D$, where D is the telescope diameter. This is approximately twice the beam FWHM, so that the array does not produce an instantaneously fully sampled image. A suitable scanning or multiple-pointing ("jiggling") scheme is therefore needed to achieve fully sampled maps.

2.4.2 ^{3}He cooler and thermal strap system

The same ^{3}He cooler design (Duband et al., 1998), shown in Figure **??**, is used for both SPIRE and PACS instruments. This type of refrigerator consists of a sorption pump and an evaporator and uses porous material which absorbs or releases gas depending on its temperature. The refrigerator contains 6 litres of liquid ^{3}He. At the beginning of the cold phase, all of this is contained in liquid form in the evaporator. The pump is cooled to $\sim$ 2 K, and cryo-pumps the ^{3}He gas, lowering its vapour pressure and so reducing the liquid temperature. The slow evaporation of the ^{3}He provides a very stable thermal environment at 300 mK for around 48 hours under constant heat load in normal observing and operational circumstances.

Once most of the helium is evaporated and contained in the pump then the refrigerator must be recycled. This is carried out by heating of the sorption pump to ~ 40 K in order to expel the absorbed gas. The gas re-condenses as liquid at $\sim$ 2 K in the evaporator. Once all of the ^{3}He has been recondensed, the pump is cooled down again and starts to cryo-pump the liquid, bringing the temperature down to 0.3 K once again. This recycling takes about 2.5 hours and is usually performed during the daily telecommunications period (DTCP). Gas gap heat switches control the cooler and there are no moving parts. The confinement of the ^{3}He in the evaporator at zero-g is achieved by a porous material that holds the liquid by capillary attraction. A Kevlar wire suspension supports the cooler during launch whilst minimising the parasitic heat load. Copper straps connect the cooler 0.3 K stage to the five detector arrays, and are held rigidly at various points by Kevlar support modules. The supports at the entries to the spectrometer and photometer 1.7 K boxes are also designed to be light-tight.

2.4.3 Warm electronics

There are three SPIRE warm electronics units. The Detector Control Unit (DCU) provides the bias and signal conditioning for the arrays and cold electronics, and demodulates and digitises the detector signals. The FPU Control Unit (FCU) controls the ^{3}He cooler, the Beam Steering Mechanism and the FTS scan mirror, and also reads out all the FPU thermometers. The Digital Processing Unit (DPU) runs the on-board software interfaces with the spacecraft for commanding and telemetry. The 130 kbs available data rate allows all photometer or spectrometer detectors to be sampled and the data transmitted to the ground with no on-board processing.

Chapter 3

SPIRE observing modes and performance

3.1 Introduction

Any observation with SPIRE (or any of the *Herschel* instruments) was performed following an Astronomical Observation Request (AOR) made by the observer. The AOR is constructed by the observer by filling in an Astronomical Observation Template (AOT) in the *Herschel* Observation Planning Tool, HSpot. Each template contains options to be selected and parameters to be filled in, such as target name and coordinates, observing mode etc. How to do this is explained in details in the HSpot user's manual, while in the relevant sections in this chapter we explain the AOT user inputs.

Once the astronomer has made the selections and filled in the parameters on the template, the template becomes a request for a particular observation, i.e. an AOR. If the observation request is accepted via the normal *proposal* $\Rightarrow$ *evaluation* $\Rightarrow$ *time allocation* process then the AOR content is subsequently translated into instrument and telescope/spacecraft commands, which are up-linked to the observatory for the observation to be executed.

There are three Astronomical Observation Templates available for SPIRE: one for doing photometry just using the SPIRE Photometer, one to do photometry in parallel with PACS and one using the Spectrometer to do imaging spectroscopy at different spatial and spectral resolutions.

Building Blocks: Observations are made up of logical operations, such as configuring the instrument, initialisation and science data taking operations. These logical operations are referred to as building blocks. The latter operations are usually repeated several times in order to achieve a particular signal-to-noise ratio (SNR) and/or to map a given sky area. Pipeline data reduction modules work on building blocks (see Chapter 8).

Configuring and initialising the instrument: It is important to note that the configuration of the instrument, i.e. the bolometer parameters, such as setting the bias, the science data and housekeeping data rates etc., are only set once at the beginning of the *Herschel* operational day when the particular instrument is in use. There are however detector settings that are set up at the beginning of each observation, like the bolometer A/C offsets. It is not possible to change the settings dynamically throughout an observation and this may have implications for observations of very bright sources with strong surface brightness gradients, mainly signal clipping or signal saturation.

PCAL: During SPIRE observations, the photometer calibration source, PCAL, is operated at intervals to track any responsivity drifts. Originally it was planned to use PCAL every 45 minutes, but in-flight conditions have shown excellent stability and following performance verification phase a new scheme has been adopted where PCAL is only used once at the end of an observation. This adds approximately 20 seconds to each photometer observation. For the spectrometer this can take a few seconds longer as the SMEC must be reset to its home position.

3.2 SPIRE Photometer AOT

This SPIRE observing template uses the SPIRE photometer (Section 2.2) to make simultaneous photometric observations in the three photometer bands (250, 350 and 500 μm). It can be used with three different observing modes:

- Large areas maps: This mode is for covering large areas of sky or extended sources larger than 5 arcmin diameter. The map is made by scanning the telescope.
- Small area maps: This is for sources or areas with diameters smaller than 5 arcmin. The map is made by two short cross-scans with the telescope.
- Point source photometry: This mode is for photometric observations of isolated point sources. It uses chopping, jiggling and nodding, observing the source at all times.
  This mode was never used for science observations.

3.2.1 Large Map

Description

The build up of a map is achieved by scanning the telescope at a given scan speed (*Nominal* at $30''$/s or *Fast* at $60''$/s) along lines. This is shown in Figure 3.1.

As the SPIRE arrays are not fully filled, the telescope scans are carried out at an angle of ± 42.4 deg with respect to the Z-axis of the arrays and the scan lines are separated by $348''$ to provide overlap and good coverage for fully sampled maps in the three bands. This is shown schematically in Figure 3.1. One scan line corresponds to one building block.

Cross-linked scanning (or cross scanning) is achieved by scanning at $+42.4$ deg (Scan A angle) and then at -42.4 deg (Scan B angle), see Figure 3.3. The cross-scan at Scan A and B is the default Large Map scan angle option in HSpot. This ensures improved coverage of the mapped region. Although the $1/f$ knee for SPIRE is below 0.1 Hz (Griffin et al., 2010), the cross-scanning also helps to reduce the effect of the $1/f$ noise when making maps with maximum likelihood map makers like MADMAP (Cantalupo et al., 2010). Note that the $1/f$ noise will be less significant at the faster scan speed.

Real coverage maps for the cross scanning and single direction scanning for the different SPIRE bands can be found in Section 3.2.1.

When $1/f$ noise is not a concern, the observer can choose either one of the two possible scan angles, A or B. The two are equivalent in terms of observation time estimation, overheads, sensitivities, but one may be favourable, especially when the orientation of the arrays of the sky does not vary much (due to either being near the ecliptic plane or to having a constrained observation, see below).

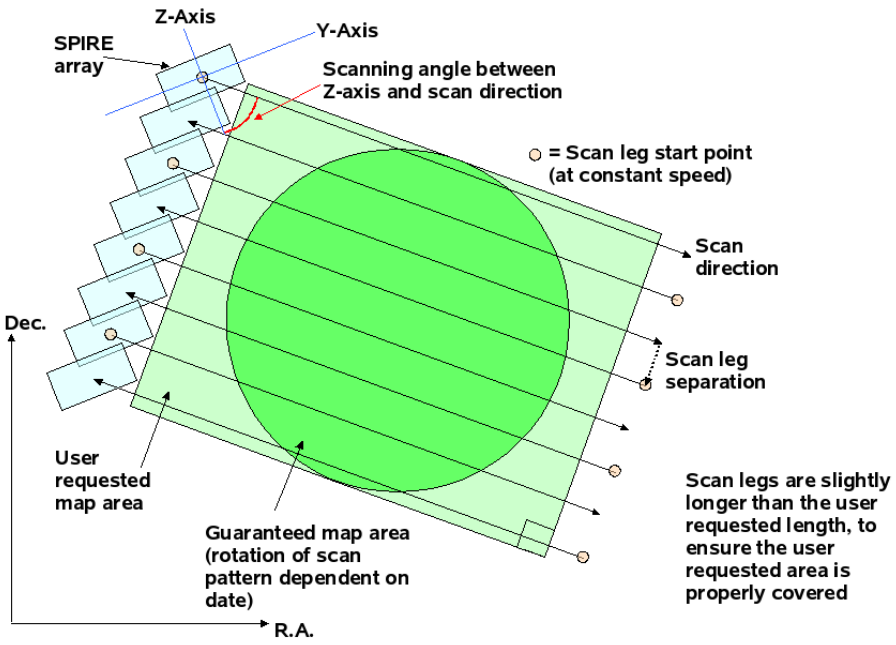

Figure 3.1: Large Map build up with telescope scanning, showing the scan angle, the scan legs and the guaranteed map area.

To build up integration time, the map is repeated an appropriate number of times. For a single scan angle, the area is covered only once. For cross-linked scanning, one repetition covers the area twice, once in each direction. Hence cross-linked scanning takes about twice as long and gives better sensitivity and more homogeneous coverage (see Figure 3.6).

Cross-linked scanning is limited to an area of just under 4 degrees square, whereas single direction scans can be up to nearly 20 degrees in the scan direction and just under 4 degrees in the other direction. Hence, with a single scan direction, it is possible to make very long rectangular maps. Note that cross-scan observations for highly rectangular areas are less efficient, as many shorter scans are needed in one of the directions.

The dimensions of the area to be covered are used to automatically set the length and the number of the scan legs. The scan length is set such that the area requested has good coverage throughout the map and that the whole array passes over all of the requested area with the correct speed. The number of scan legs is calculated to ensure that the total area requested by the user is observed without edge effects (a slightly larger area will be covered due to the discrete nature of the scans). Hence the actual area observed will always be bigger than what was requested.

The area is by default centred on the target coordinates; however this can be modified using map centre offsets (given in array coordinates). This can be useful when one wants to do dithering or to observe the core of an object plus part of its surroundings, but does not mind in which direction from the core the surrounding area is observed.

The scans are carried out at a specific angle to the arrays, and the orientation of the arrays on the sky changes as *Herschel* moves in its orbit. The actual coverage of the map will rotate about the

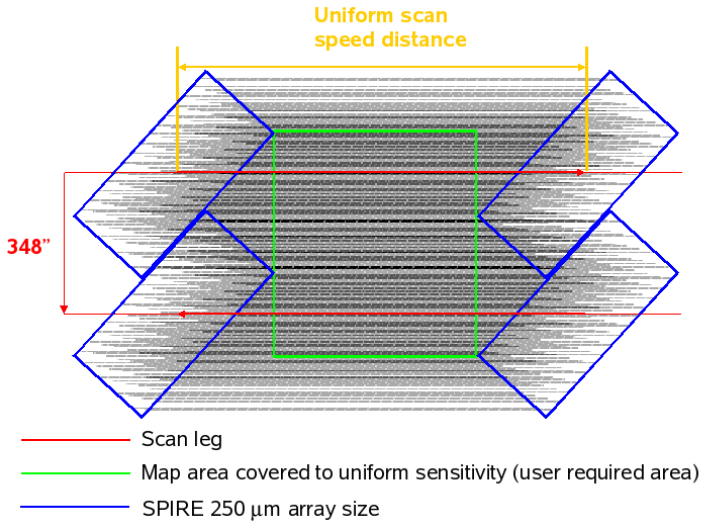

Figure 3.2: Large Map coverage showing the scan direction with respect to the SPIRE arrays, the scan leg separation step and the uniform sensitivity coverage region. The darker the shading the deeper the coverage.

target coordinates depending on the exact epoch at which the data are taken (except for sources near the ecliptic plane where the orientation of the array on the sky is fixed: see the *Herschel* Observers' Manual). This is shown in Figure 3.1.

To guarantee that the piece of sky you want to observe is included in the map, you can oversize the area to ensure that the area of interest is included no matter what the date of observation. This works well for square-like fields, but for highly elongated fields the oversizing factor would be large. To reduce the amount of oversizing needed for the map you can use the Map Orientation "Array with Sky Constraint" setting to enter a pair of angles *A1* and *A2*, which should be given in degrees East of North. The orientation of the map on the sky, with respect to the middle scan leg, will be restricted within the angles given. This reduces the oversizing, but the number of days on which the observation can be scheduled is also reduced.

Note also that, as explained in *Herschel* Observers' Manual, parts of the sky do not change their orientation with respect to the array and therefore it is not possible to set the orientation of the map in certain directions (the ecliptic) as the array has always the same orienatation. The constraints on when the observation can be performed make scheduling and the use of *Herschel* less efficient, hence the observer will be charged 10 minutes observatory overheads (instead of 3 minutes) to compensate (see the *Herschel* Observers' Manual).

Warning: Setting a Map Orientation constraint means that your observation can only be performed during certain periods, and the number of days that your observation can be scheduled will be reduced from the number of days that the target is actually visible, because it is a constraint on the observation, not the target itself. In setting a constraint you will need to check that it is still possible to make your observation.

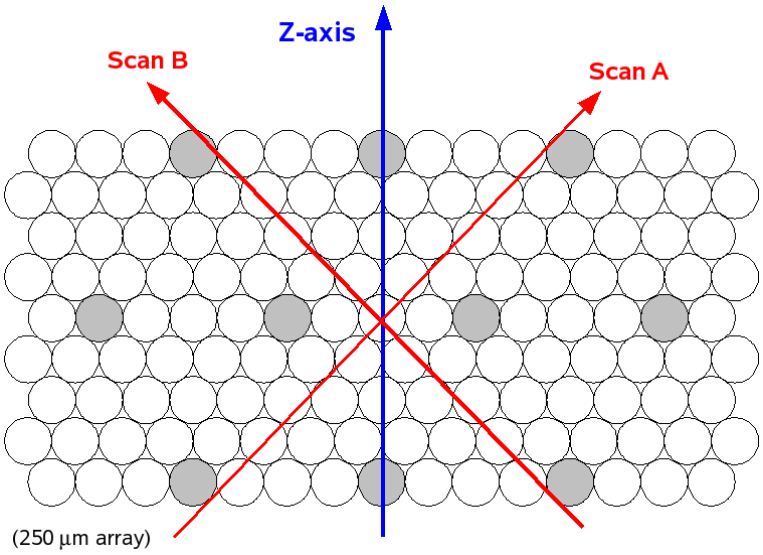

Figure 3.3: Large Map scan angles.

User inputs

The user inputs in HSpot are shown Figure 3.4 and summarised below:

Repetition factor:
The number of times the full map area is repeated to achieve the required sensitivity. For cross-linked maps (Scan Angles A and B), there are two coverages per repetition, one in each direction. For single scan direction observations (Scan Angle A or Scan Angle B), one coverage is performed per repetition.

Length:
This is the scan length of the map (in arcmin). It corresponds to the length in the first scan direction.

Height:
This is the size of the map (in arcmin) in the other dimension.

The maximum allowed Length and Height for cross-linked large maps (Scan Angles A and B) are 226 arcmin for both directions. For scans in either Scan Angle A or Scan Angle B, the maximum Length is 1186 arcmin and the maximum Height is 240 arcmin.

Scan speed:
This can be set as Nominal, $30''$/s (the default value) or Fast, $60''$/s.

Scan direction:
The choices are Scan Angles A and B (the default option, giving a cross-linked map), Scan Angle A, or Scan Angle B.

Map centre offset Y, Z:
This is the offset (in arcmin) of the map centre from the input target coordinates along the Y or Z axes of the arrays. The minimum offset is $\pm 0.1'$ and the maximum allowed is $\pm 300'$.

Figure 3.4: Large Map parameters in HSpot

Map Orientation:
This can be set at either Array or Array with Sky Constraint. The latter option can be entered by selecting a range of map orientation angles for the observation to take place. The orientation angle is measured from the equatorial coordinate system North to the direction of the middle scan leg direction, positive East of North, following the Position Angle convention. The orientation constraint means a scheduling constraint and should therefore be used only if necessary.

Angle from/to:
In the case when Array with Sky Constraint is selected, the pair of angles (in degrees) between which the middle scan leg can lie along.

Source Flux Estimates (optional):
An estimated source flux density (in mJy) and/or an estimated extended source surface brightness (MJy/sr) may be entered for any of the three photometer bands, in which case the expected S/N for that band will be reported back in the Time Estimation. The sensitivity results assume that a point source has zero background and that an extended source is not associated with any point sources. The point source flux density and the extended source surface brightness are treated independently by the sensitivity calculations. If no value is given for a band, the corresponding S/N is not reported back. The time estimation will return the corresponding S/N, as well as the original values entered, if applicable.
Bright Source Setting (optional): this mode has to be selected if the expected flux of the source is above 200 Jy (see Section 3.5.1).

Coverage Maps

Coverage maps for cross-scanning and for single direction scanning for each of the three bands are shown in Figure 3.5. These were taken from standard pipeline processing of real observations with SPIRE. Note that the coverage maps are given as number of bolometer hits per sky pixel. The standard sky pixels for the SPIRE Photometer maps are (6, 10, 14)$''$ (see Section 5.9).

Time estimation and sensitivity

The estimated time to perform a single scan and cross-linked scans for one square degree field ($60' \times 60'$) and one repetitions are given in the HSpot screenshots in Figure 3.6.

The sensitivity estimates are subject to caveats concerning the flux density calibration (see Chapter 5). The reported 1-σ noise level does not include the confusion noise, which ultimately limits the sensitivity (see *Herschel* Confusion Noise Estimator for more details). It is important to keep in mind that the galactic confusion noise can vary considerably over the sky.

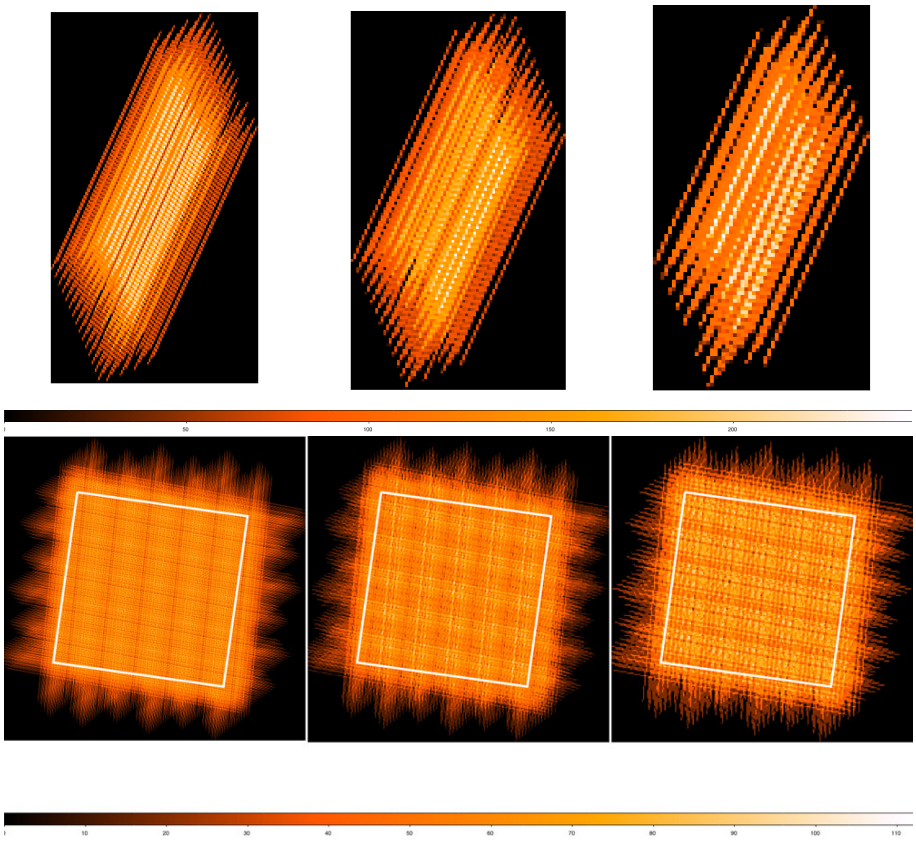

Figure 3.5: Example coverage maps for Large Map mode for the three photometer arrays, PSW (left), PMW (centre) and PLW (right). The top row is for a single scan-A observation. The bottom row is for a cross-linked scan of $30' \times 30'$ field, the white square is the user requested area. The pixel size is (6,10,14)$''$ for (PSW, PMW, PLW) and the colour code represents the number of bolometer hits in each sky pixel.

When to use this mode

Large map mode is used to cover large fields, larger than $5'$ diameter, in the three SPIRE photometer bands. Note that the mode can still be used even for input height and width of $5'$, however the efficiency is low and the map size will be much larger than the requested $5' \times 5'$ field.

The coverage map for a single scan observation is inhomogeneous due to missing or noisy bolometers (see Figure 3.5). Even though the $1/f$ noise is not a big effect even for single scan maps our advice is to use cross-linked maps when a better flux reconstruction is needed (i.e. deep fields, faint targets, etc).

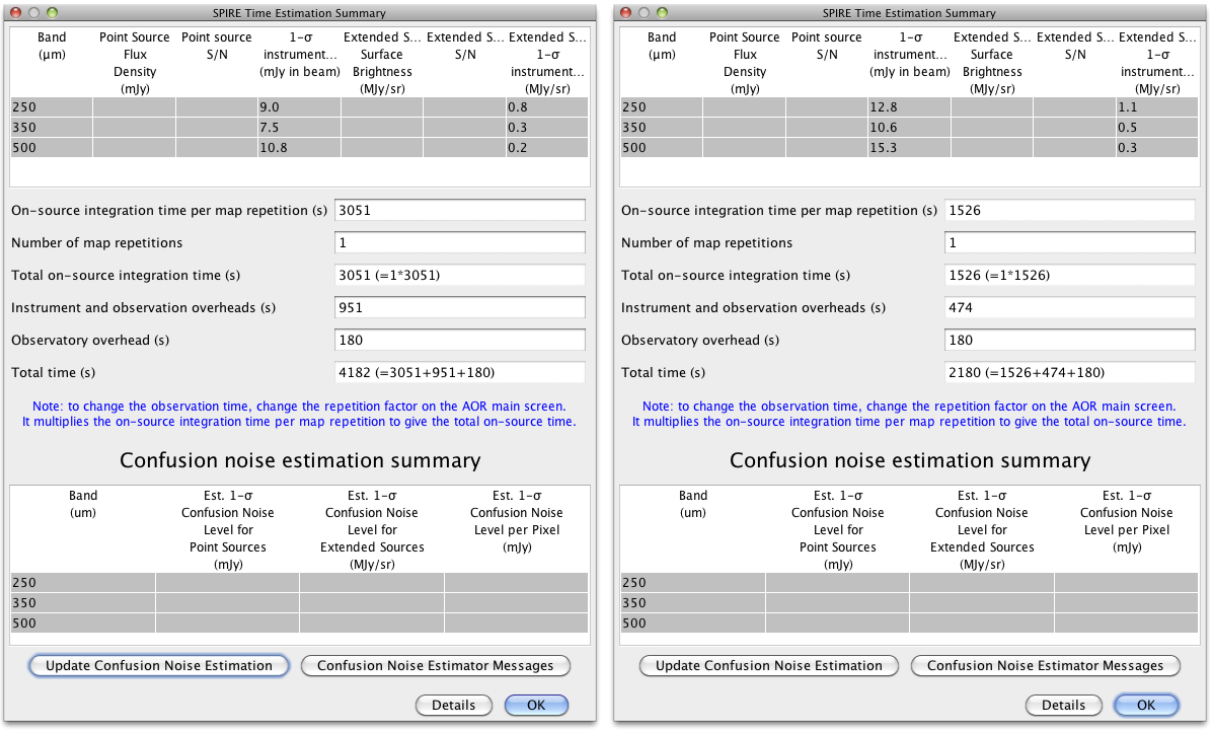

Figure 3.6: Large Map time estimation and sensitivity for a filed of $60' \times 60'$ and one repetition for a cross-linked (scan A and B, left) and single scan direction (right).

3.2.2 Small Map

Description

The SPIRE Small Map mode is designed for observers who want a fully sampled map for a small $< 5'$ dimeter area of sky. The original SPIRE Small Map mode was initially a 64-point Jiggle Map. However, after analysis and investigation this has been replaced by a 1×1 small scan map using nearly orthogonal (at 84.8 deg) scan paths.

The Small Scan Map mode is defined as follows;

- 1x1 nearly orthogonal scan paths.
- Scan Angles are fixed at $\pm$42.4 degrees with respect to the Spacecraft Z-axis.
- Fixed scan path with guaranteed coverage of $5'$ diameter circle.
- Fixed scan speed = $30''$/s.
- Calibration PCAL flash made only at end of Observation.
- Map offsets available.
- Otherwise identical to the SPIRE Large Scan Map mode.

User inputs

The user inputs in HSpot are shown in Figure 3.7, left and described below.

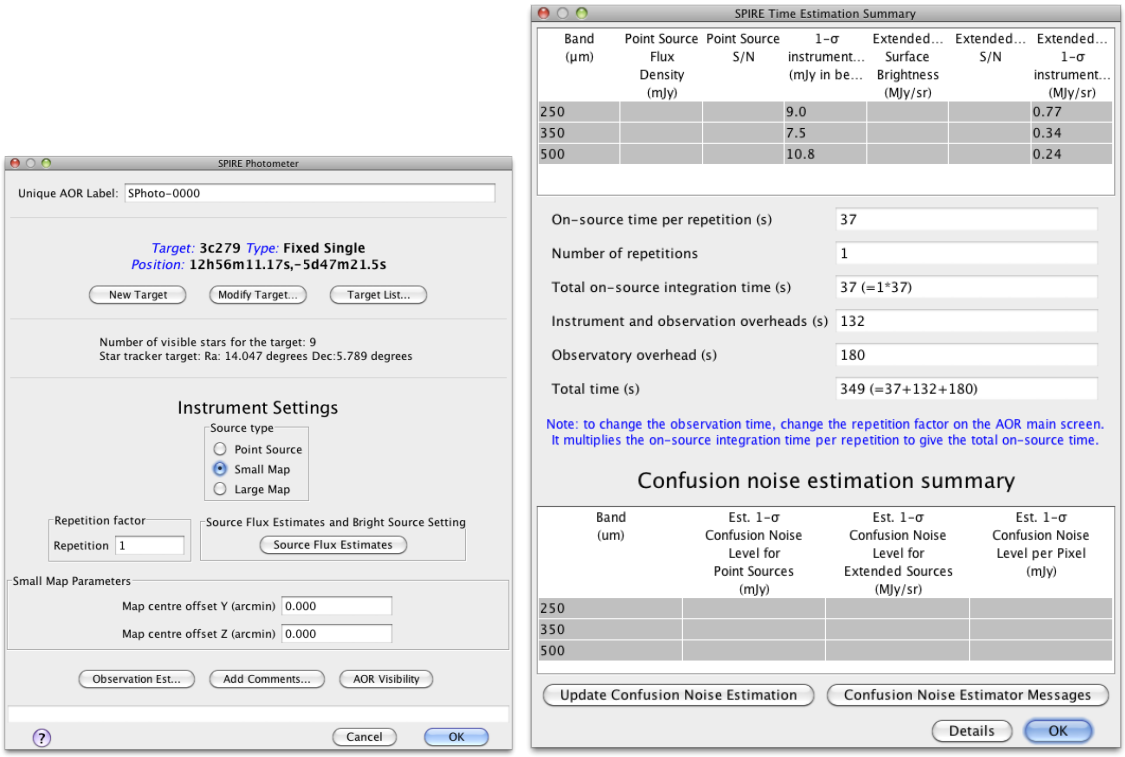

Figure 3.7: User inputs in HSpot for Small Map AOT (left) and Small Map mode time estimation, sensitivity estimate for one repetition of the map.

Repetition factor:
The number of repeats of the 1x1 scan pattern.

Map Centre Offset Y and Z:
This is the offset (in arcmin) of the map centre from the input target coordinates along the Y or Z axis of the arrays. The minimum offset is $\pm 0.1'$ and the maximum allowed is $\pm 300'$.

Source Flux Estimates (optional):
An estimated source flux density (in mJy) may be entered for a band, in which case the expected S/N for that band will be reported back in the Time Estimation. The sensitivity results assume that a point source has zero background. If no value is given for a band, the corresponding S/N is not reported back.

Bright Source Setting (optional):
this mode has to be selected if the expected flux of the source is above 200 Jy (see Section 3.5.1).

Time estimation and sensitivity

The time estimation and sensitivities are shown in Figure 3.7, right. The sensitivity estimates and the caveats are the same as the Large Map mode.

Coverage maps

The coverage maps at 250, 350 and 500 μm from a real observation are shown in Figure 3.8. For a given observation the area covered by both scan legs defines a central square of side $5'$, although the length of the two orthogonal scan paths are somewhat longer than this. In practice, due to the position of the arrays on the sky at the time of a given observation, the *guaranteed* area for scientific use is a circle of diameter $5'$.

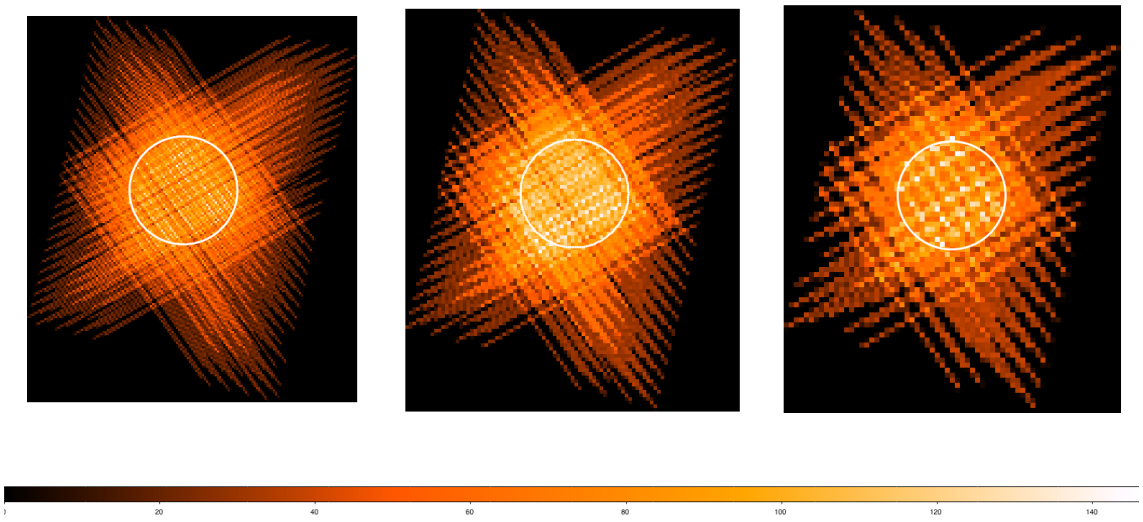

Figure 3.8: Example coverage maps for Small Map mode for the three photometer arrays, PSW (left), PMW (centre) and PLW (right), taken from a real observaiton. The white circle is with $5'$ diameter. The pixel size is $(6,10,14)''$ for (PSW, PMW, PLW) and the colour code represents the number of bolometer hits in each sky pixel.

When to use this mode

This mode has the same sensitivity as the Large Map mode but for small areas it uses less time.

3.2.3 Point Source

Note that this mode was never used for science observations. However, for completeness we provide the details similarly to the previous two photometry modes.

Description

A mini-map is made around the nominal position to make sure that the source signal and position can be estimated. This mini-map is made by moving the BSM around to make the map as shown in Figure 3.9 for one detector. The 7-point map is made by observing the central position and then moving the BSM to observe six symmetrically arranged positions (jiggle), offset from the central position by a

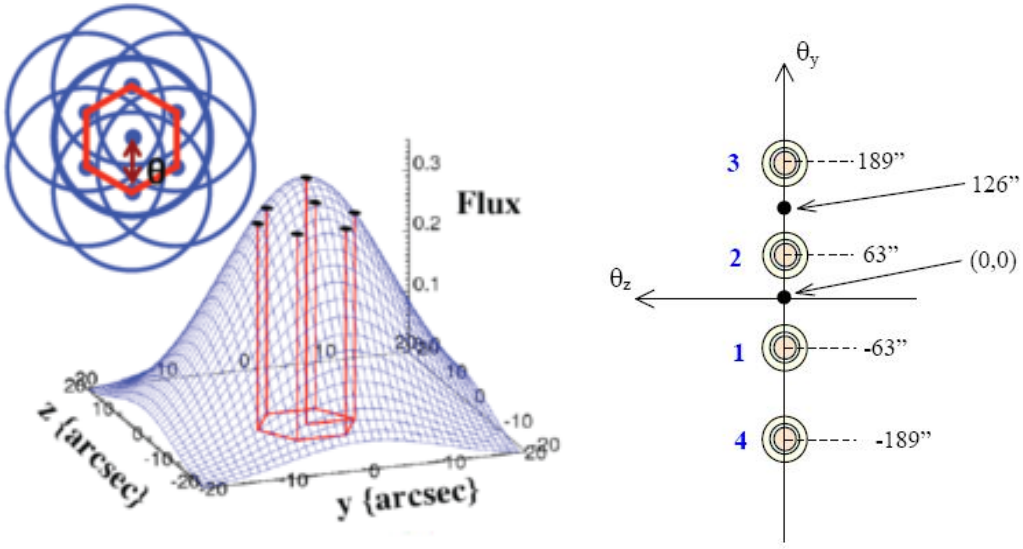

Figure 3.9: Left: the 7-point hexagonal jiggle pattern. Note that the central point is revisited at the end. The seven points are used to fit the 2-D beam as shown in the drawing. Right: the image shows the central co-aligned pixels as they appear on the sky. The circles numbered 1 and 2 show the detectors on which a point source is viewed via the chopping and nodding which is described in detail in the text. The angular positions of detectors are also shown.

fixed angle (nominally $6''$), and then returning to the central point once more (note that the 7 in 7-point refers to the number of different positions). At each of these positions chopping is performed between sets of co-aligned detectors (Figure 3.9, right) to provide spatial modulation and coverage in all three wavelength bands.

The chop direction is fixed along the long axis of the array (Y), and the chop throw is $126''$. The nominal chop frequency is 1 Hz. Sixteen chop cycles are performed at each jiggle position. Nodding, once every 64 seconds, is performed along the Y axis to remove differences in the background seen by the two detectors.

Figure 3.9, right, shows the central row of co-aligned pixels. At the first nod position (nod A at 0,0) the source is repositioned with the BSM on detector 1 and the chopping is performed between 1 and 2. Then the telescope nods at $+126''$ (as shown in the figure), this is nod B, and the target is repositioned with the BSM on detector 2. The chopping is between 2 and 3. Note that in this scheme detector 4 is not used. This is one AB cycle. The standard Point source photometry observation uses ABBA cycle, i.e. we repeat in reverse the same scheme. To acquire further integration time, the ABBA nod pattern is repeated an appropriate number of times: ABBA ABBA etc.

The chop and nod axis is the same and is parallel to the long axis of the array to allow switching between co-aligned pixels. As *Herschel* moves in its orbit, the orientation of the array on the sky changes. To avoid chopping nearby bright sources onto the arrays (see e.g. Figure 3.11), pairs of angles can be defined (up to three pairs are allowed) which will prevent the observation being made when the long axis of the arrays lies between the specified angles. Note that both the specified angle range and its equivalent on the other side of the map ($\pm$ 180 degrees) are avoided.

Setting a chop avoidance criterion means that an observation will not be possible during certain periods, and the number of days on which the observation can be made will be reduced from the number of days that the target is actually visible (visibility in HSpot does not take into account the constraint). In setting a constraint you will therefore need to check that it is still possible to make your observation and that you have not blocked out all dates. Note also that, as explained in the *Herschel* Observers' Manual, parts of the sky near the ecliptic plane do not change their orientation with respect to the array and therefore it is not possible to avoid chopping in certain directions.

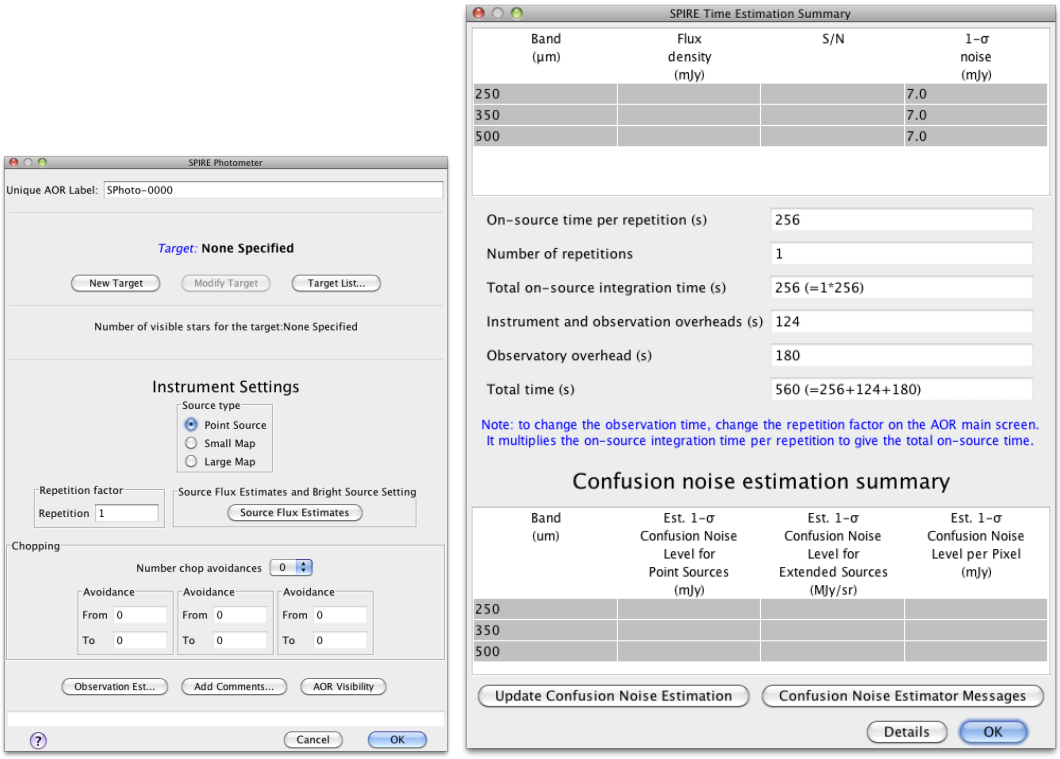

Figure 3.10: HSpot user inputs for Point Source mode (left) and the HSpot time estimation for Point Source mode (right).

A practical tip is to transform the pair of chop avoidance angles (A1, A2) to pairs of position angles of the *Herschel* focal plane. Then, with the help of the HSpot target visibility tool, the days when the focal plane position angle does not fall between the derived angles can be identified. As the chopping is on the Y-axis then the pair of chop avoidance angles (A1,A2) corresponds to two pairs of *Herschel* focal plane position angles (PA1,PA2) = (A1, A2) ± 90 deg, which have to be avoided.

Warning: The constraints on when the observation can be performed make scheduling and the use of *Herschel* less efficient. The observer will be charged extra 10 minutes in overheads (rather than the usual 3) to compensate.

User Inputs

The user input in HSpot are shown in Figure 3.10 and explained below.

Table 3.1: The basic parameters for the Point Source mode.

Parameter	Value
Chop Throw	$126''(\pm\ 63'')$
Chopping frequency	1Hz
Jiggle position separation	$6''$
Nod Throw	$126''(\pm\ 63'')$
Central co-aligned detector	PSW E6, PMW D8, PLW C4
Off-source co-aligned detectors	PSW E2,E10, PMW D5,D11, PLW C2,C6
Number of ABBA repeats	1
Integration time	256 s
Instrument/observing overheads	124 s
Observatory overheads	180 s
Total Observation Time	560 s

Repetition factor:
The number of times the nod cycle ABBA is repeated to achieve the required sensitivity.

Number of chop avoidances:
An integer between 0 and 3.

Chopping Avoidance Angles From/To:
To be used when number of chop avoidances is greater than zero. A From/To pair defines a range of angles to be avoided. Note that also the range $\pm$180 degrees is also avoided. The interval is defined in equatorial coordinates, from the celestial north to the +Y spacecraft axis (long axis of the bolometer), positive East of North, following the Position Angle convention. This effectively defines an avoidance angle for the satellite orientation, and hence it is a scheduling constraint.

Source Flux Estimates (optional):
An estimated source flux density (in mJy) may be entered for a band, in which case the expected S/N for that band will be reported back in the Time Estimation. The sensitivity results assume that a point source has zero background. If no value is given for a band, the corresponding S/N is not reported back.
Bright Source Setting (optional): this mode has to be selected if the expected flux of the source is above 200 Jy (see Section 3.5.1).

When to use this mode

The SPIRE Point Source mode is recommended for bright isolated sources in the range 0.2-4 Jy where the astrometry is accurately known and accurate flux measurement is required. For sources fainter than 200mJy (where the background produces a significant contribution) or at fluxes higher than $\sim$ 4 Jy (where pointing jitter can introduce large errors) the Small Map mode is preferable.

For Point Source mode, the effective sky confusion level is increased due to chopping and nodding (by a factor of approximately 22% for the case of extragalactic confusion noise) and should be added in quadrature to the quoted instrumental noise levels. The result of the measurement is therefore affected by the specific characteristics of the sky background in the vicinity of the source and will depend on the chop/nod position angle in the event of an asymmetric background. Note that although

it is possible to set a chop avoidance angle within HSpot this will constrain the possible dates for the observation

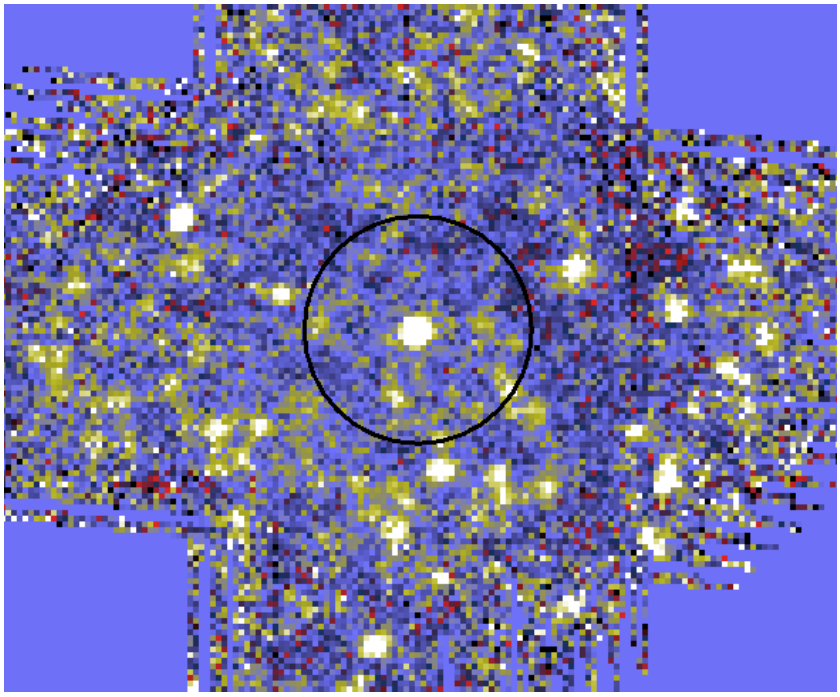

Figure 3.11: Example of possible chop area on a realistic background.

The example in Figure 3.11 shows a scan map observation of a $\sim$ 220 mJy source. The circle drawn around the source corresponds to the chop and/or nod throw used in the Point Source mode. Moving around the circumference of the circle it is found the background can vary between $\pm$30mJy depending on the chop/nod position angle used for the observation. Therefore, due to the problems of confusion noise, and the dependence of the result on the position angle of the observation, the point source AOT is not recommended for sources fainter than $\sim$ 200 mJy, for which a small scan map will produce a better measurement including an accurate characterisation of the background.

For Point Source mode observations of bright sources ($\geq$ 4 Jy) the uncertainties are dominated by pointing jitter and nod-position differences, resulting in a S/N of the order of 100 at most (the uncertainties in the data will also be limited by the accuracy of the flux calibration, which will be at least 5%). Users should be aware of these effects and take them into consideration.

3.3 SPIRE and PACS Parallel Mode

3.3.1 Definition of Parallel Mode

In Parallel Mode, SPIRE and PACS are operating in photometry mode simultaneously, carrying out large-area mapping observations. SPIRE is observing in its three photometric bands (250, 350 and 500 μm), while PACS is taking data in its red band (130-210 μm) and in one of the blue bands (60-85 μm or 85-130 μm).

The SPIRE PACS Parallel Mode is treated as a 4th Herschel instrument, i.e. it has its own Astronomical Observing Template (AOT), its own user interface in HSpot and the two instruments are operated in a way that the spacecraft infrastructure is optimally used. The advantage of Parallel Mode is ensured by the compatibility of the two instruments and their operating modes. In practice, simultaneous observations in five bands are made possible without significant degradation in instrument performance. However, considering the fact that the PACS and SPIRE integration times are identical, the relative instrument sensitivities have to be carefully inspected to judge the real scientific benefit of using Parallel Mode.

In Parallel Mode, the detectors' sampling frequency of the SPIRE instrument is reduced to 10 Hz, in respect to the 18.2 Hz of the SPIRE-only operations. Observations performed during the PV-phase demonstrated that this does not affect the quality of SPIRE data, especially when scanning at $20''$/s (slow mode). However, scanning at $60''$/s (fast mode) has a small impact, mostly on glitch detection, removal and timeline reconstruction, and, as a second order effect, on beam smearing.

The PACS instrument applies an additional data compression with respect to PACS-prime operations, in order to make sure that the data rate in the five bands (3 for SPIRE and 2 for PACS) stays within the allowed limits. In the blue channel, data frames are averaged on-board 8 by 8, but the compression is left unchanged; in the red channel, a 4 by 4 frames averaging is applied. As a consequence, in Parallel Mode the PSF is more elongated in the blue channel than in PACS-prime scan mapping.

Scientific Benefits of Parallel Mode

As there is no evident degradation of SPIRE data between the SPIRE-prime and the Parallel Mode configuration, as long as the on-source integration time is the same, when the program involves large areas (bigger than $30' \times 30'$), and the observer is interested mainly in SPIRE data, it is advantageous to use Parallel Mode in respect to SPIRE-only observation, basically obtaining PACS data for free. In order to get the same on-source integration time as the SPIRE-only observation, the observer might require to repeat the observation multiple times, including cross-scans observations.

Instead, for PACS we do see a degradation of the PSF in respect to PACS-only observations, due to the higher compression factor in Parallel Mode. Hence, if the program mainly relies on PACS-data, it might be better to schedule PACS and SPIRE observations separately.

As a consequence, for programmes involving shallow galactic surveys over large areas of sky, Parallel Mode offers a major efficiency gain and major additional scientific data with respect to two separate PACS and SPIRE coverages. For other mapping programmes like deep galactic surveys or extra-galactic surveys, there may be some advantages with careful design of mosaicking, although not so great.

Shallow galactic surveys

For very large shallow surveys, where the requested coverage is typically in the order of 100 square degrees or more, the observer could save a significant time compared to using the two instruments separately and covering the survey area twice. This is the most likely instance in which Parallel Mode could be beneficial.

Galactic surveys

Deep surveys of nearby molecular clouds mapped with SPIRE will have a benefit using Parallel Mode mode. Instead of doing SPIRE observations only, it is conceivable that PACS is operated in parallel without compromising SPIRE data quality, providing a shallow PACS survey of the complete regions. This would effectively provide additional data for the same observing time. The benefits in terms of mapping efficiency and additional data would not be as great as for a larger shallow survey, but PACS data could be worthwhile nonetheless.

Deep extragalactic surveys

For such a programme the Parallel Mode gain on mapping efficiency is not a great benefit. This is particularly true under the assumption that the survey area of deep extragalactic mapping programmes is considerable smaller than for galactic surveys. Moreover, these observations will cover a range of depths where both PACS and SPIRE sensitivities are demanding. As with the galactic surveys, it is possible that PACS could be operated in parallel to provide additional data but in considerable lower sensitivities.

Additional benefits of Parallel Mode

Operating SPIRE and PACS together increases the load on the helium tank of Herschel by much less than a factor of two, because the total load is largely from the cryostat parasitics. Parallel operations is thus very favourable in terms of science per litre of helium, increasing the overall lifetime of the observatory. Moreover, observations made in Parallel Mode will have more accurate relative PACS/SPIRE astrometry, because the relative angular offsets between the two arrays are fixed and accurately known and the pointing error will be the same for the two instruments throughout the observation. The efficiency of scientific mission planning is also increased because the scheduling of PACS and SPIRE observations of the same sky area can be done within a single block. This reduces the total telescope slew time over the mission lifetime in favour of science time.

3.3.2 SPIRE and PACS Parallel Mode AOT

The Parallel Mode AOT is offered with only one observing mode: scanning. It is the only compatible mode for operating SPIRE and PACS simultaneously: in fact, scan mode is the only option for both SPIRE and PACS to map large areas of the sky, even when they are operated alone.

The scanning strategy has been optimised for both instruments. Scan maps are performed by slewing the spacecraft at a constant speed along parallel lines to cover a large area. The lines follow great circles on the sphere which approximates parallel lines over short distances. When finishing a scan leg, the spacecraft has to perform a turn manoeuvre and continue observing along the next scan leg in the opposite direction: the time required for this turn is about half a minute. Note that scan mapping does not make use of chopping, being the signal modulation provided by the spacecraft motion.

The Parallel Mode AOT does not allow to do cross-scans in a single observation. However, it is normal practice to perform two scan maps of the same area, one with nominal coverage and the other with orthogonal coverage, in order to remove more efficiently the stripping effects due to the 1/f noise

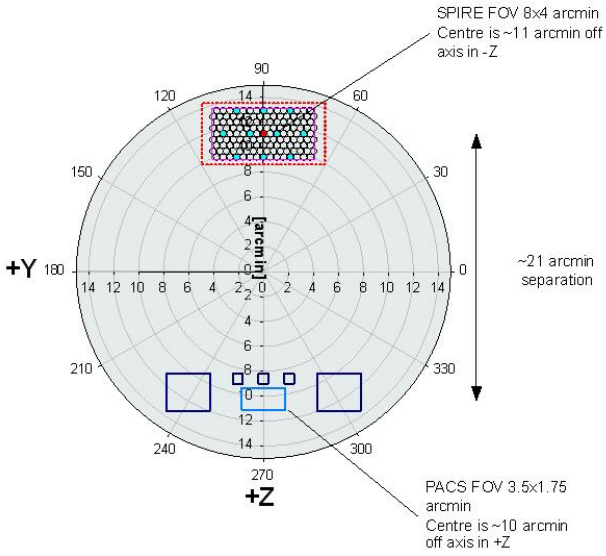

Figure 3.12: PACS and SPIRE footprints overlayed on the Herschel focal plane image. The field-of-views of the two instruments are separated by $21'$ respectively.

and to get better coverage redundancy, especially for SPIRE. For this purpose two AORs are typically concatenated in HSpot to be performed with a different scan direction.

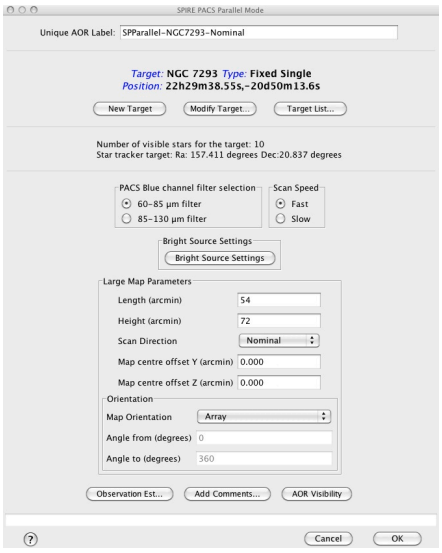

Figure 3.13: HSpot window for setting up the Parallel Mode AOR

As the SPIRE arrays are not fully filled, the telescope scans in Parallel Mode are carried out at $+42.4\,\mathrm{deg}$ ("Nominal" scan direction) or $-42.4\,\mathrm{deg}$ ("Orthogonal" scan direction) with respect to short axis of the arrays (angle from instrument +Z-axis to +Y-axis, see Figure 3.12). In order to provide homogeneous coverage over the mapping area and to optimise PACS performances in the two scan directions, the step size between consecutive lines is $168''$ when scanning in the "Nominal" direction and $155''$ when scanning in the "Orthogonal" one. This small step size for SPIRE (being $348''$ for SPIRE-only large scan maps, see Section 3.2.1) results in a high oversampling factor and a gain in sensitivity, without compromising map uniformity.

Setting up AOT parameters

When selecting "SPIRE PACS Parallel Mode" from the "Observation" menu in HSpot (see Chapter 14 of the HSpot Users' Guide), a window like the one shown in Figure 3.13 appears on the screen. As a first step, the PACS band has to be selected in the blue channel (60-85 μm or 85-130 μm). The other four Parallel Mode bands are fixed.

In the second step, selecting the scan speed the observer could have control over the sensitivity of the measurement.

The depth of observation in Parallel Mode mode can be controlled by three ways: (i) adjust scan speed; (ii) add "Nominal" and "Orthogonal" coverages on the same area of the sky; (iii) repeat AORs. Note that there is no possibility to repeat Parallel Mode maps within one single observation request (AOR) to enhance the survey depth.

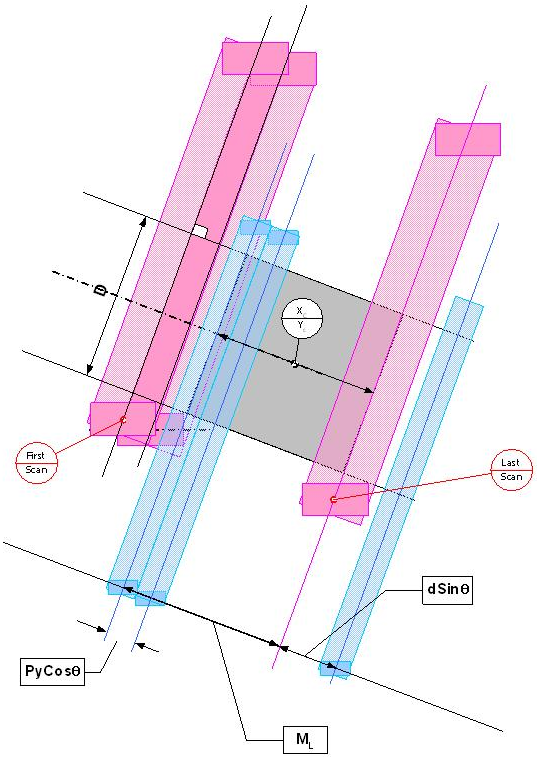

Figure 3.14: Illustration of Parallel Mode scanning scheme. The grey area is the common SPIRE-PACS survey field what the observer specifies in HSpot. The scanning angle with respect the arrays' short axis is $42.4\,\mathrm{deg}$. Red colour represents the SPIRE scanning path, blue colour is used for PACS.

The dimensions of the area to be covered is set by the length and height of the common SPIRE-PACS survey area (see Figure 3.14). The figure illustrates how the common SPIRE-PACS survey area - the grey box - is actually built up. The number of scans required to cover the common area is higher than would be required in a single instrument coverage. The number of extra scans and the required length of the scan legs both depend on the scan angle and the footprints separation. Taking into account the $42.4\,\mathrm{deg}$ scan angle and the fixed $21'$ separation of the SPIRE and PACS focal plane footprints on the sky, the Parallel Mode observations perform five or six extra scans and extend the scan leg length by $22'$ respectively. Hence, the actual area observed with each instrument will be bigger than what was requested.

Note: Using the SPIRE Photometer AOT, the Parallel Mode settings can be reproduced in scan map mode simply enlarging the requested area by $\sim 15'$ in both length and height. This applies to PACS scan map mode too. In this case, however, the observer must set a scan step of $168''$ and $+42.4\,\mathrm{deg}$ orientation angle in "Array" or "Array with sky constraint" reference frame to get the same Parallel

Mode “Nominal” scan direction coverage. The scan step must be set to $155''$ and the orientation angle to $-42.4\,\mathrm{deg}$ to reproduce the Parallel Mode “Orthogonal” scan direction coverage.

The centre of the common survey area is at the coordinates given by the target position, unless an offset along the axes Y or Z of the spacecraft coordinates is given. The map size along a scan leg can be specified by the map “Length” parameter. In perpendicular direction, the common survey size is defined by the ”Height” parameter. In case the scan direction is set to “Orthogonal”, then the observer has to change the “Length” and “Height” parameters and the spacecraft will perform an observation along $-42.4\,\mathrm{deg}$ scan angle over the same survey area specified for the “Nominal” direction. The pairs of nominal and orthogonal AORs can be concatenated in HSpot (see further details in the HSpot Users’ Guide).

An illustration of how a Parallel Mode AOR footprint is visualised in HSpot can be seen in Figure 3.15 and in Figure 3.16. Pink represents the PACS and green the SPIRE footprint: the observer requested common survey area is painted by both instruments. SPIRE and PACS coverage maps as taken from real observations.

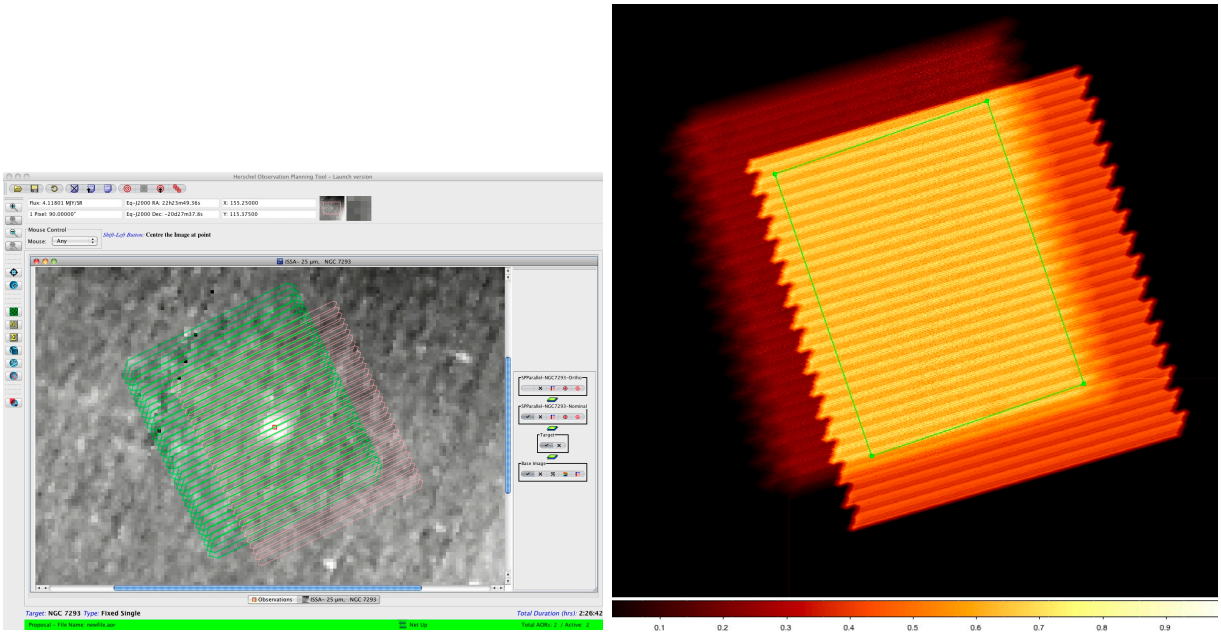

Figure 3.15: Parallel Mode footprint image example as displayed in HSpot (left). NGC 7293 is imaged in “Nominal” scan direction with a coverage area of $54' \times 72'$. A comparison between observer’s requested area and real instrument coverages, normalised to 1, is shown on the right, the green rectangle is the original observer requested area. SPIRE coverage is the darker area on the left.

Three optional parameters are available:

- “Bright Source Setting”: enabling this setting (disabled by default), settings of SPIRE and PACS photometers will be optimised to observe bright sources, without saturating their dynamic range, but at the cost of sensibly increasing the instruments’ noise. Depending on the science case, the observer might want to enable it for one or both instruments. Please refer to the SPIRE Observers’ Manual and the PACS Observers’ Manual for applicable flux thresholds.

- "Map centre offset": by default, the common SPIRE-PACS coverage is centred on the target coordinates. The observer has the option to apply an offset to the centre, given in spacecraft coordinates (Y,Z) in arcminutes.
- "Orientation": as the map is carried with a specific angle of the arrays and because the orientation of the array on the sky changes as Herschel moves in its orbit, then the actual coverage of the map will rotate about the requested centre of the map except for sources close to the ecliptic plane. However, in order to cover specific rectangular (elongated) areas in the sky, a constraint on the orientation of the scan map in the sky can be introduced by selecting a range for the "map position angle", i.e. the angle from the celestial equatorial North to the scan line direction, counted positively East of North. This corresponds to the option "Array with Sky Constraint" in HSpot.

Setting a Map Orientation constraint means that your observation will not be able to be performed during certain periods, hence the number of days that your observation can be made will be reduced from the number of days that the target is actually visible. In setting a constraint, the observer needs to check that it is still possible to fit the observation within a visibility window or if the orientation constraint blocked out all dates. Note also that parts of the sky do not change their orientation with respect to the array and therefore it is not possible to set the orientation of the map in certain directions (close to the ecliptic plane) as the array is orientated in a restricted direction on the sky. Note: Setting constraints on when the observation can be performed make scheduling and the use of Herschel less efficient, hence the observer will be charged extra overheads to compensate.

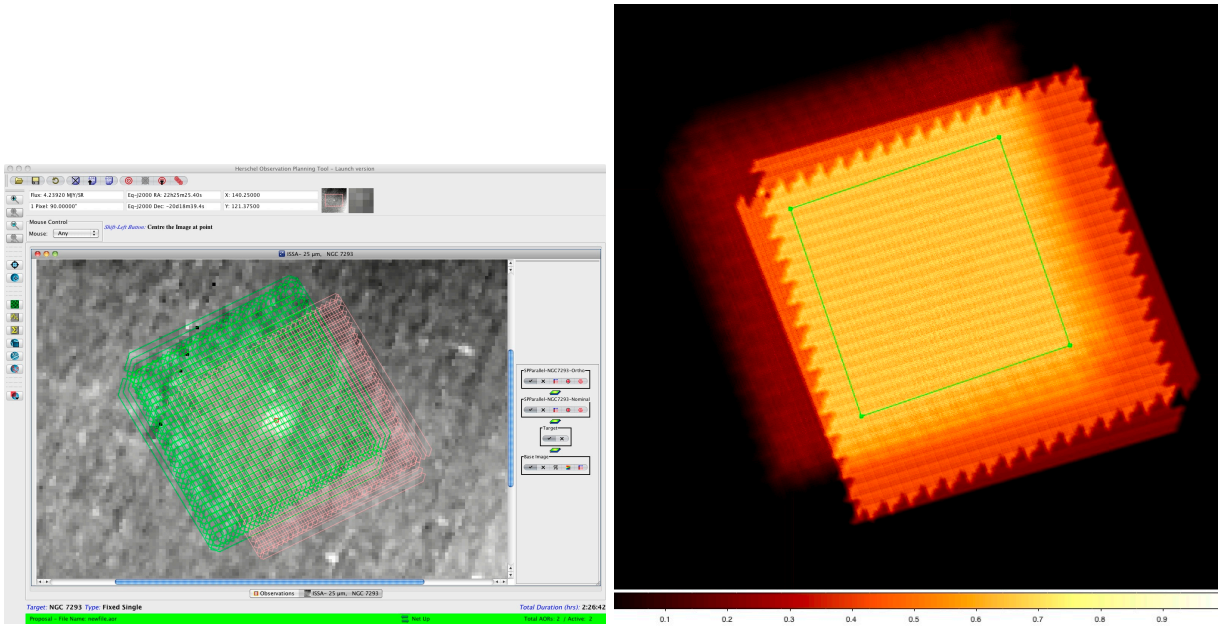

Figure 3.16: Parallel Mode footprint image example as displayed in HSpot (left). NGC 7293 is imaged in "Nominal" plus "Orthogonal" scan directions. However, the "Length" and "Height" parameters are the same in the 2 AORs (instead of being inverted): the result is that the area covered by both instruments, in both directions, is only $54' \times 54'$. The right panel shows the SPIRE (darker area on left) and PACS coverage maps, normalized to 1, as obtained from observation of NGC 7293 in "Nominal" and "Orthogonal" scan directions. The green rectangle is the user requested area.

Parameter name	Comments
Filter	Which of the two filters from the PACS blue channel to use (60-85 μm or 85-130 μm).
Map Orientation	The reference frame for the scan map orientation, either "Array" or "Array with Sky Constraint". This can be entered, by selecting a range of map orientation angles for the observation to take place.
Angle from/to	The constraint on map angle is the angle measured from the equatorial North to the direction of the scan leg calculated East of North and towards the scan direction of the map's first scan leg.
Scan speed	Slew speed of the spacecraft: fast mode ($60''$/s) or slow mode ($20''$/s).
Length	Length of the common survey area parallel the scan direction in arcminutes: the maximum length is $1173'$.
Height	Size of the common survey area in perpendicular direction in arcminutes: the maximum height is $231'$.
Scan Direction	This parameter defines the scan angle along which the spacecraft builds up the scan legs. In "Nominal" direction the scan angle is $42.4\,\mathrm{deg}$ and the scan leg separation is $168''$, in "Orthogonal" direction the angle is set to $-42.4\,\mathrm{deg}$ and the scan leg separation to $155''$.
Map centre offset Y	The offset of the map centre from the input target coordinates along the Y axis of the spacecraft coordinate system, in arcminutes.
Map centre offset Z	The offset of the map centre from the input target coordinates along the Z axis of the spacecraft coordinate system, in arcminutes.

Table 3.2: Observer input parameters for SPIRE PACS Parallel Mode AOT.

3.4 SPIRE Spectrometer AOT

This observing mode is used to make spectroscopic observations with the SPIRE Fourier Transform Spectrometer (Section 2.3). The Spectrometer was used to take spectra with different spectral resolutions:

- High resolution (HR);
- Medium resolution (MR);
- Low resolution (LR);
- High and Low resolutions (H+LR).
- and Calibration resolution (CR), only used for calibration observations.

Spectra can be measured in a single pointing (using a set of detectors to sample the field of view of the instrument) or in larger spectral maps, which are made by moving the telescope in a raster. For either of these, it is possible to choose sparse, intermediate, or full Nyquist spatial sampling. In summary, to define an observation, one needs to select a spectral resolution (high, medium, low, high and low), an image sampling (sparse, intermediate, full) and a pointing mode (single or raster). These options are described in more detail in the next sections.

The HSpot input parameters for all[1] SPIRE Spectrometer observing modes are shown in Figure 3.17. In the following sections we describe each one of the options.

3.4.1 Spectral Resolution

The Spectrometer Mirror Mechanism (SMEC) is scanned continuously at constant speed over different distances to give different spectral resolutions (see Section 2.3). For every repetition, two scans of the SMEC are done: one in the forward direction and one in the backward direction, making one scan pair, as shown in Figure 3.18. Two scan pairs are deemed essential for redundancy in the data. The desired integration time is set by increasing the number of scan pairs performed (corresponding to the number of repetitions entered in HSpot).

The summary of the OPD ranges and the corresponding spectral resolutions are shown in Table 3.3.

Low Resolution (LR):

Usage and Description: To make continuum measurements at the resolution of Δf= 24.98 GHz ($\lambda/\Delta\lambda = 48$ at $\lambda = 250\mu$m). The SMEC is scanned symmetrically about ZPD over a short distance. It takes 6.4 seconds to perform one scan in one direction at low resolution. This mode is intended to survey sources without spectral lines or very faint sources where only an SED is required.

Medium Resolution (MR):

Usage and Description: The medium resolution of Δf= 7.2 GHz ($\lambda/\Delta\lambda = 160$ at $\lambda = 250$ μm) was never used for science observations.

[1] CR mode was only available in the expert HSpot.

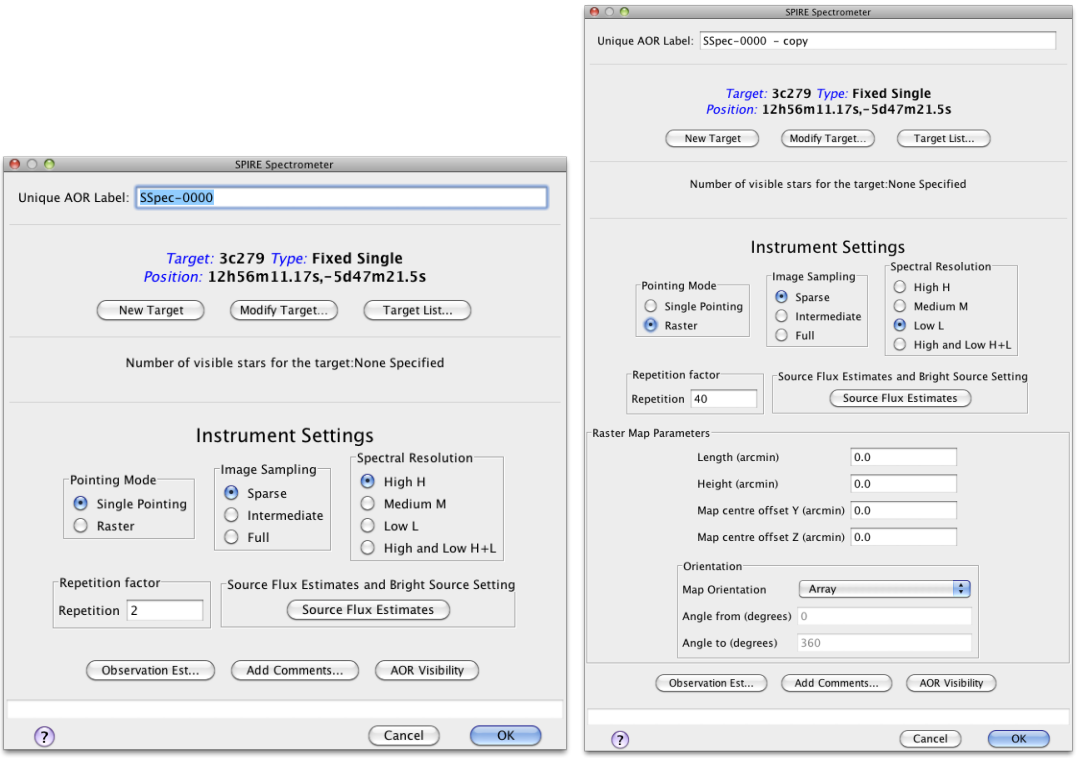

Figure 3.17: The HSpot initial screen for the SPIRE Spectrometer AOTs, point source mode (left) and raster (right)

High Resolution (HR):

Usage and Description: The high resolution mode gives spectra at the highest resolution available with the SPIRE spectrometer, Δf= 1.2 GHz, this corresponds to $\lambda/\Delta\lambda = 1000$ at $\lambda = 250$ μm. High resolution scans are made by scanning the SMEC to the maximum possible OPD of 12.65 cm from ZPD. It takes 66.6 s to perform one scan in one direction at high resolution. This mode is best for discovery spectral surveys where the whole range from 194 to 671 μm can be surveyed for new lines. It is also useful for simultaneously observing sequences of spectral lines across the band (e.g. the CO rotational ladder). In this way, a relatively wide spectral range can be covered in a short amount of time compared to using HIFI (although with much lower spectral resolution than achieved by HIFI, see the HIFI Handbook).

Calibration resolution (CR) mode was used for calibration observations up to *Herschel* Operational Day 1054 (02 Apr 2012). In this mode the SMEC was scanned from the max OPD (+12.645 cm) to the min OPD available (-2.4 cm), see Table 3.3. The spectral resolution is the same as for the HR-mode, because the maximum OPD dictates the resolution and this is the same for both modes. The benefit of CR-mode is that there is a larger symmetric region around the ZPD, which helps the phase correction pipeline module (see Fulton 2012 for details). The different standing-wave (fringe) patterns in HR-mode and CR-mode, however, lead to different noise properties. Hence all CR-mode observations, including calibration observations, were processed as HR-mode by limiting the min OPD to the HR limit.

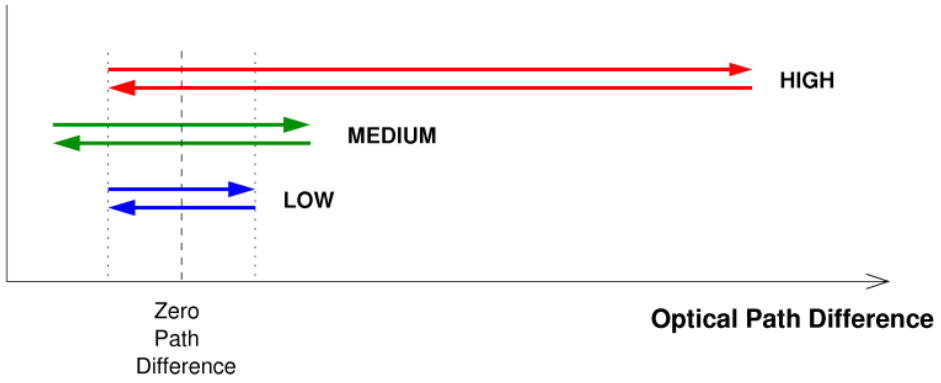

Figure 3.18: Diagram to show how the SMEC moves (in terms of optical path difference) during one repetition for High, Medium and Low spectral resolution. The low resolution SMEC scan range is always covered during High or Medium resolution observations.

Similarly, LR spectra can be extracted by the pipeline from HR or CR observations, using data only within the LR-mode OPD limits. Consequently, the equivalent LR continuum *rms* noise (for the number of scan repetitions chosen) can also be recovered from a HR observation, i.e. improving the sensitivity on the continuum.

For cases where the signal-to-noise ratio (SNR) for this extracted low resolution spectrum is not sufficient for the scientific case, the following "High and Low" resolution mode is available:

High and Low Resolution:

Usage and Description: This mode allows observations of a high resolution spectrum as well as using additional integration time to increase the SNR of the low resolution continuum. This mode saves overhead time over doing two separate observations.

The number of high resolution and low resolution scans can differ, and will depend on the required S/N for each resolution. If the number of repetitions for the high and low resolution parts are nH and nL respectively, then the achieved low resolution continuum sensitivity will correspond to nH+nL

Table 3.3: Optical path difference (OPD) range and spectral resolution for the FTS resolution modes. For an unresolved $sinc$ line (see Section 3.5.3 and Figure 3.25), the spectral resolution is the distance from the peak to the $sinc$-function first zero crossing. Note that in the current pipeline, CR is processed as HR and MR is processed as LR.

Mode	OPD range [cm]	Resolution [GHz]
LR	-0.555 – +0.560	24.98
MR	-2.395 – +2.400	7.200
HR	-0.555 – +12.645	1.184
CR	-2.395 – +12.645	1.184

repetitions, because low resolution data can also be extracted from every high resolution scan.

3.4.2 Pointing Modes

A pointing mode and an image sampling are combined to produce the required sky coverage. Here the pointing modes are described.

Single Pointing Mode:

Usage and Description: This is used to take spectra of a region covered by the full instrument field of view of 2.6′ diameter. Only the field of view of the arrays on the sky is observed with one pointing of the telescope.

Raster Pointing Mode:

Usage and Description: This mode is used to take spectra of a region larger than the 2.6′diameter field of view of the instrument. The telescope is pointed to various positions making a hexagonally packed map (see example in Figure 3.19). At each position, spectra are taken at one or more BSM positions depending on the image sampling chosen (see Section 3.4.3). The HSpot input parameters are shown in the right side of Figure 3.17.

Details: The area to be covered determines the number of pointings in the map. The distances between individual pointings are 116″ along the rows and 110″ between the rows, as shown in Figure 3.19. The number of pointings needed to cover the map is rounded up to ensure that the whole of the requested area is mapped. By default, the area is centred on the target coordinates, however this can be modified using map centre offsets (given in array coordinates).

Note that for raster maps the target centre does not necessarily correspond to the centre of the detector array (see Figure 3.19), as the map is not circular and because the orientation of the array on the sky changes as *Herschel* moves in its orbit. The actual coverage of the map will rotate about the requested centre of the map (usually the target coordinates unless an offset is used) except for sources near the ecliptic (see the *Herschel* Observers' Manual). To force the actual area to be observed to be fixed or to vary less, the Map Orientation settings of "Array with Sky Constraint" can be used to enter a pair of angles (which should be given in degrees East of North) to restrict the orientation of the rows of the map to be within the angles given.

Setting a Map Orientation constraint means that it will not be possible to perform the observation during certain time periods. Fewer days will be available to make such a constrained observation. In setting a constraint the observer will need to check that not all observing dates have been blocked and that it is still possible to schedule the observation. Note also that, as explained earlier, parts of the sky do not change their orientation with respect to the array and therefore it is not possible to set the orientation of the map in certain directions (the ecliptic) as the array is only orientated in one way on the sky. These constraints on when the observation can be performed make scheduling and the use of *Herschel* less efficient, hence the observer will be charged extra overheads to compensate.

Alternatively, raster observations can be split into several concatenated AORs to allow some tailoring of the coverage to match the source shape (but note that every concatenated AOR will be charged the 180 second slew tax).

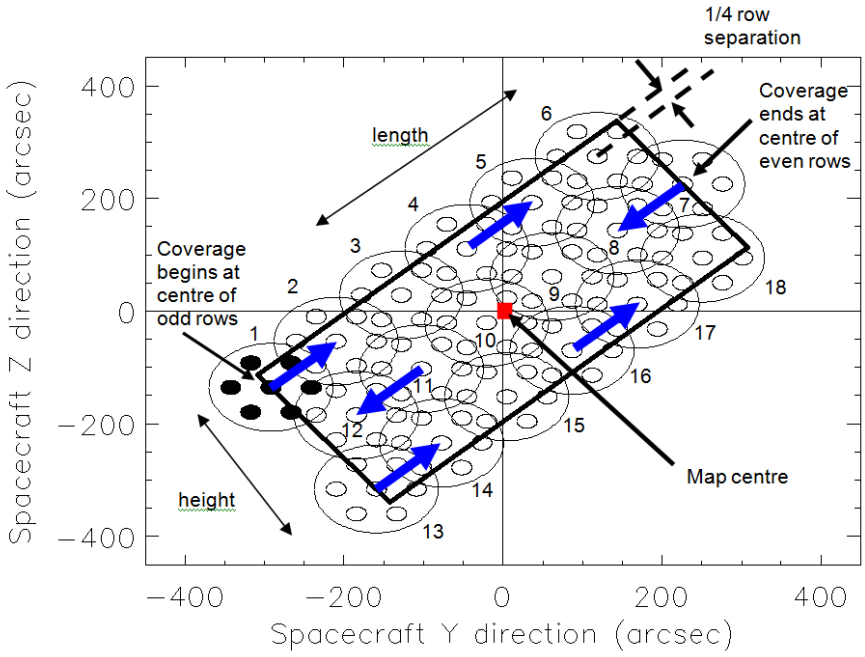

Figure 3.19: Ratser map with the SPIRE FTS.

User Input: The map parameters are similar to those for the Photometer Large Map. The Spectrometer parameters are listed in Section 3.4.4.

3.4.3 Image Sampling

The pointing and an image sampling mode are combined to produce the required sky coverage. Here the image sampling options are described and figures are given to show the sampling. Note that the figures show only the unvignetted detectors.

Sparse Image Sampling:

Usage and Description: In single pointing or raster, the BSM is not moved during the observation, producing a single array footprint on the sky. The result is an observation of the selected source position plus a hexagonal-pattern sparse map of the surrounding region with beam centre spacing of (32.5, 50.5)″ in the (SSW, SLW) bands as shown in Figure 3.21. Sparse sampling is used to measure the spectrum of a point or compact source well centred on the central detectors of the Spectrometer. For a point source this requires accurate pointing and reliable knowledge of the source position to be sure to have the source well centred in the (central) detector beam.

Intermediate Image Sampling:

Usage and Description: In single pointing or raster, the BSM is moved on a 4-point jiggle pattern to produce a spectral map with intermediate spatial sampling: 1 beam spacing or (16.3, 25.3)″ for SSW and SLW respectively, as shown in Figure 3.21 and Figure 3.22. The input number of repetitions is

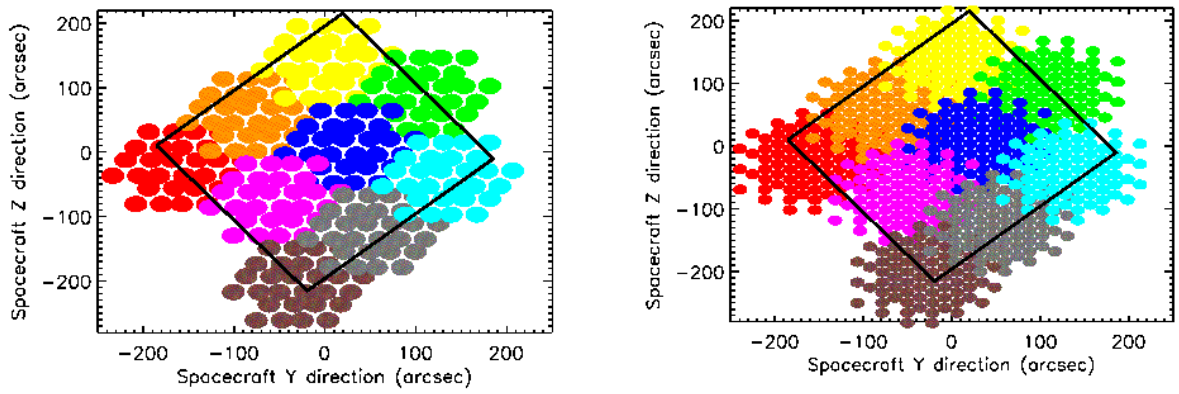

Figure 3.20: Spectrometer raster example to show spacing of the individual pointings for the long wavelength array (SLW, left) and the short wavelength array (SSW, right) for intermediate image sampling.

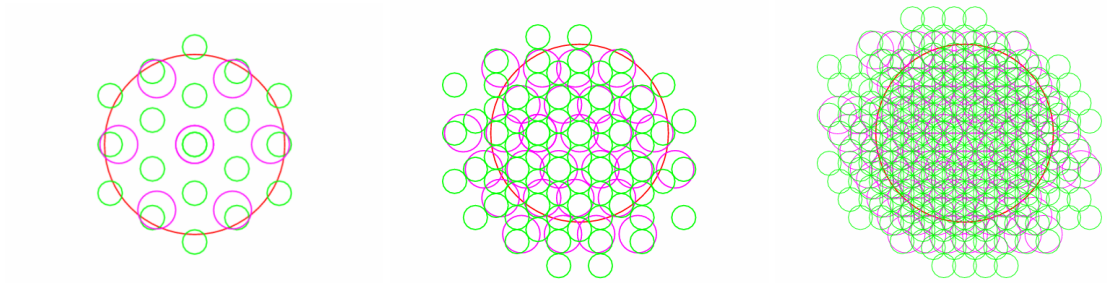

Figure 3.21: SPIRE Spectrometer spatial sampling: sparse (left), intermediate (centre) and full (right). The small green and magenta circles indicate the regions where spectra will be observed for different spatial samplings. The green circles show SSW and the magenta show SLW, the large red circle of 2′ diameter is to guide the eye for the unvignetted field of view.

performed at each of the 4 positions to produce the spectra. The coverage maps for the SSW and SLW in this mode are shown in Figure 3.23, left column.

Full Image Sampling:

Usage and Description: In single pointing or raster, the BSM is moved in a 16-point jiggle to provide complete Nyquist sampling (1/2 beam spacing) of the required area. The beam spacing in the final map is (8.1, 12.7)″ as shown in Figure 3.21 and in Figure 3.22. The input number of repetitions is performed at each one of the 16 positions to produce the spectra. The coverage maps for the SSW and SLW in this mode are shown in Figure 3.23, right column.

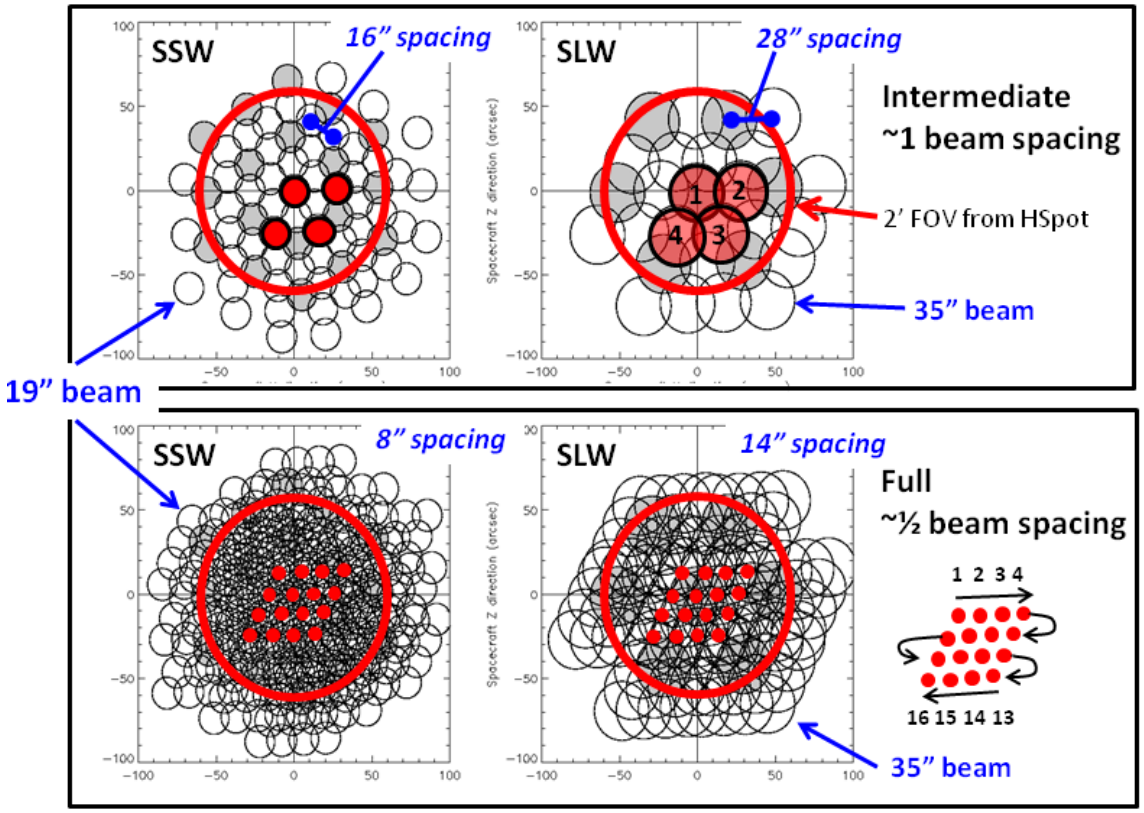

Figure 3.22: The FTS mapping pattern with intermediate image sampling for SSW and SLW (4-point jiggle, top) and full sampling (16 point jiggle, bottom). The red circle shows the 2′ diameter unvignetted field of view of the FTS. The spacing of the beams is indicated for each of the detector arrays and the two image sampling modes. The red dots show the central detector of each array at the 4 jiggle positions (top) and the 16 jiggle positions (bottom).

3.4.4 User input parameters for all Spectrometer AOTs.

The user inputs shown in Figure 3.17 are given below:

Pointing Mode:
Single Pointing or Raster selection. See Section 3.4.2 for details. Note that if Raster is selected then size of the map (Length and Height) must be given.

Image Sampling:
Sparse, Intermediate or Full. See Section 3.4.3 for details.

Spectral Resolution:
High, Medium, Low or High and Low. See Section 3.4.1 for details.

Repetition factor:
The number of spectral scan pairs to be made at each position. Note that if High and Low resolution is selected you can independently control the number of pairs for each resolution.

Length:
In arcmin. The length of the raster map along the rows.

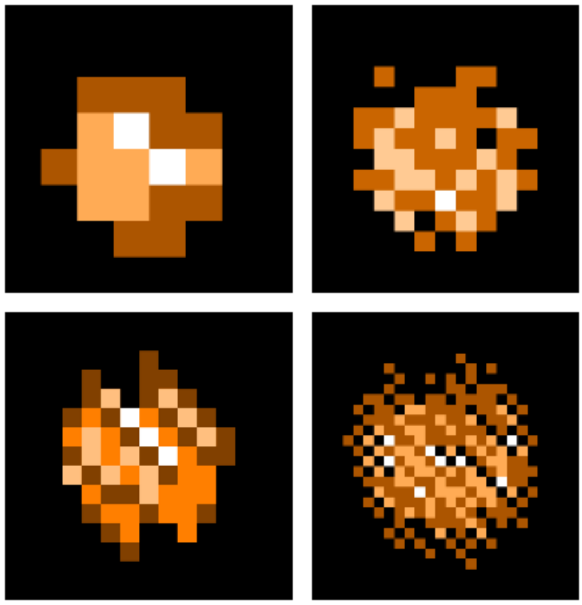

Figure 3.23: Intermediate (top) and Full (bottom) spatial sampling coverage maps for SLW (left) and SSW (right) from a real SPIRE FTS mapping observation using the naive projection method to build up the spectral cube. The sky spectral pixel (spaxel) sizes are the default 35″ (top left), 17.5″ (bottom left), 19″ (top right), 9.5″ (bottom right). The number of bolometer hits in each sky pixel are encoded with colour. The coverage maps depend on the observational day, and hence the holes in the maps (black pixels), due to dead bolometers, change from observation to observation. More homogeneous coverage without holes in the centre can be achieved using the convolution projection method, the default SPIRE spectral cubes making method from HIPE v14 (see the SPIRE Data Reduction Guide for details).

Height:
In arcmin. The height of the raster map.

Map centre offset Y, Z:
In arcmin. The offset of the raster map centre from the input target coordinates along the Y or Z axes of the arrays. Minimum is $\pm 0.1'$, maximum $\pm 300'$.

Map Orientation:
Either Array or Array with Sky Constraint. If Array with Sky Constraint is selected then range of the map orientation is constrained. This is a scheduling constraint and should therefore only be used if necessary.

Angle from/to:
In degrees East of North. In the case that Array with Sky Constraint is selected, the angles between which the raster rows can be constrained to are entered here.

Source Flux Estimates:
Optional: if the estimated line flux in $10^{-17}\,\mathrm{W\,m^{-2}}$, and/or the estimated continuum (selectable units either Jy or $10^{-17}\,\mathrm{W\,m^{-2}\,\mu m^{-1}}$) is entered along with a wavelength then the expected SNR for that line or continuum will be reported back in the Time Estimation as well as the original values entered. The time estimator always returns 1-σ flux sensitivity, 1-σ continuum sensitivity and unapodised

resolving power for 8 standard wavelengths. Note, when Low resolution is selected only continuum information can be entered and returned (plus the unapodised resolving power). When High and Low resolution is selected data are returned for the two different resolutions, the low resolution sensitivity does not take into account the possibility to get the low resolution part from the high resolution spectrum.

Bright source mode:
Optional: when the source is expected to be very bright (see Section 6.7 for more details) then this option provides a way to switch the detectors to bright mode settings, thus avoiding signal clipping. Using this mode leads to 25 s increase in the overhead time, because the detector A/C offsets are set at the start of the observation at each jiggle position.

3.5 SPIRE Performance and sensitivity

3.5.1 Photometer

The photometer sensitivity in scan map mode has been estimated from repeated scan maps of dark regions of extragalactic sky. A single map repeat is constituted by two nearly orthogonal scans as implemented in the SPIRE-only Large Map AOT. Multiple repeats produce a map dominated by the fixed-pattern sky confusion noise, with the instrument noise having integrated down to a negligible value. This sky map can then be subtracted from individual repeats to estimate the instrument noise.

The extragalactic confusion noise levels for SPIRE, defined as the standard deviation of the flux density in the map in the limit of zero instrument noise, are provided in detail in Nguyen et al. (2010). The measured extragalactic confusion and instrument noise levels are given in Table 3.4 for the nominal scan speed (30″/s). Instrument noise integrates down in proportion to the square root of the number of repetitions, and for the fast scan speed (60″/s) the instrument noise is $\sqrt{2}$ higher as expected from the factor of 2 reduction in integration time per repeat. The achieved instrument noise levels are comparable to the pre-launch estimates which were (9.6, 13.2, 11.2) mJy in beam at (250, 350, 500) μm – very similar for the 250 and 500 μm bands and somewhat better for the 350μm band.

Figure 3.24 shows the manner in which the overall noise integrates down as a function of repeats for cross-linked maps with the nominal 30″/s scan rate. The overall noise is within a factor of $\sqrt{2}$ of the (250, 350, 500) μm confusion levels for (3, 2, 2) repeats.

Table 3.4: Estimated SPIRE Photometer sensitivities.

Band	**250**	**350**	**500**
1 σ extragalactic confusion noise (mJy in beam)	5.8	6.3	6.8
SPIRE-only scan map; 30″/s scan rate			
1 σ instrument noise for one repeat: i.e., two cross-linked scans, A+B (mJy in beam)	9.0	7.5	10.8
1 σ instrument noise for one repeat: i.e., one scan A or B (mJy/beam)	12.8	10.6	15.3

Notes:

1. All sensitivity values correspond to nominal source strength settings. For bright source settings, recommended for sources brighter than 200 Jy in any band, the achieved sensitivities are de-

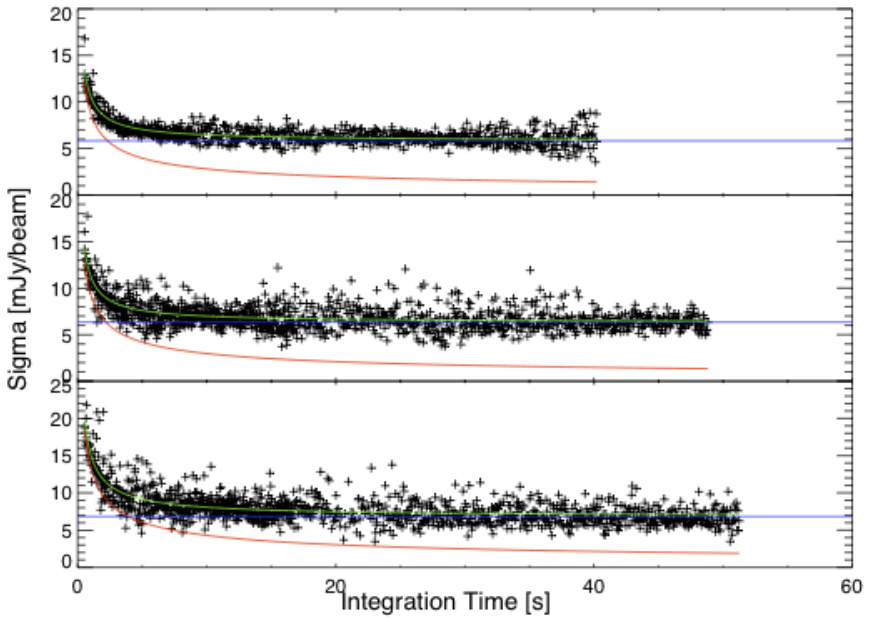

Figure 3.24: Pixel noise vs. integration time for all pixels in deep SPIRE photometer fields. The derived instrument noise is shown in red, the confusion floor is show in blue and the total noise is in green. Taken from Nguyen et al. (2010).

graded (with respect to nominal setting) by factors of (3.8, 3.2, 2.6) for (250, 350, 500) μm. It should be noted however, that in practice S/N values > 200 should not be regarded as reliable in any case.

2. All scan map sensitivity values are for nominal scan speed of 30″/s. Figures for 60″/s scale as $\sqrt{2}$.

An important aspect of the photometer noise performance is the knee frequency that characterises the $1/f$ noise of the detector channels. Pre-launch, a requirement of 100 mHz with a goal of 30 mHz had been specified. In flight, the major contributor to low frequency noise is temperature drift of the ^{3}He cooler. Active control of this temperature, available via a heater-thermometer PID control system, has not been implemented in standard AOT operation as trials have shown that a better solution, in terms of overall noise performance, is to apply a temperature drift correction in the data processing. The scan-map pipeline includes a temperature drift correction using thermometers, located on each of the arrays, which are not sensitive to the sky signal but track the thermal drifts. This correction works well and has been further improved with the recent update of the flux calibration parameters. Detector timelines to de-correlate thermal drifts over a complete observation can produce a $1/f$ knee of as low as a 1-3 mHz. This corresponds to a spatial scale of several degrees at the nominal scan speed.

As with most observing systems, high SNR predictions should not be taken as quantitatively correct. This is because small errors such as pointing jitter, other minor fluctuations in the system, or relative calibration errors, will then become significant. That is why a SNR of 200 is taken as the maximum achievable for any observation, and HSpot will never return a value of SNR greater than 200.

Table 3.5: The SPIRE PACS Parallel Mode 1-σ instrument noise for one repetitions and assuming a point source, calculated for the two scan speeds. Units for SPIRE are mJy in beam, for PACS are in mJy.

Scan Direction	Nominal		Orthogonal	
Scan Speed	60″/s	20″	60″	20″
SPIRE 500 μm	15.0	8.7	14.4	8.3
SPIRE 350 μm	10.5	6.0	10.0	5.8
SPIRE 250 μm	12.6	7.3	12.1	7.0
PACS 130-210 μm	47.0	27.3	45.2	26.3
PACS 85-130 μm	24.7	14.3	23.8	13.8
PACS 60-85 μm	21.0	12.2	20.2	11.7

3.5.2 Photometer in Parallel Mode

In this section, sensitivity numbers are given specific for the Parallel Mode (Table 3.5). The Parallel Mode AOT the observer to choose the scan speed: 60″/s (fast mode) or 20″/s (slow mode). In Table 3.5, the second column summarises sensitivities for the fast mode and the third column reports sensitivities for the deeper slow mode. To a first order, the sensitivity in scan mode scales with the inverse of the square root of the on-source observation time (the source crossing time), therefore the gain in depth if changing from fast to slow mode is about a factor of 1.7.

Table 3.5 reports 1-σ instrument noise for one repeat for a point source: values are applicable to all Parallel Mode observations irrespective of the map size. Note the difference between "Nominal" and "Orthogonal" scan directions, due to the different scan leg separation.

3.5.3 Spectrometer

Spectral range, line shape and spectral resolution

The FTS spectral range given in Table 3.6 represents the region over which the FTS sensitivity estimates and calibration are reliable.

Table 3.6: Spectral range over which FTS data is currently be calibrated. Note that the final spectra are provided in the local standard of rest (LSR) reference frame.

Band	**Spectral Range**
SSW	944 GHz (318 μm) to 1568 GHz (191 μm)
SLW	447 GHz (671 μm) to 1018 GHz (294 μm)

The instrumental line shape of a perfect FTS instrument is a $sinc = \sin(x)/x$ function, due to the truncation of the interferogram by the limited travel of the moving mirror (the SMEC). The observed line shapes for the two central detectors, derived from observations of isolated and unresolved lines, are shown in Figure 3.25. The actual line shape deviates slightly from an ideal $sinc$ function with

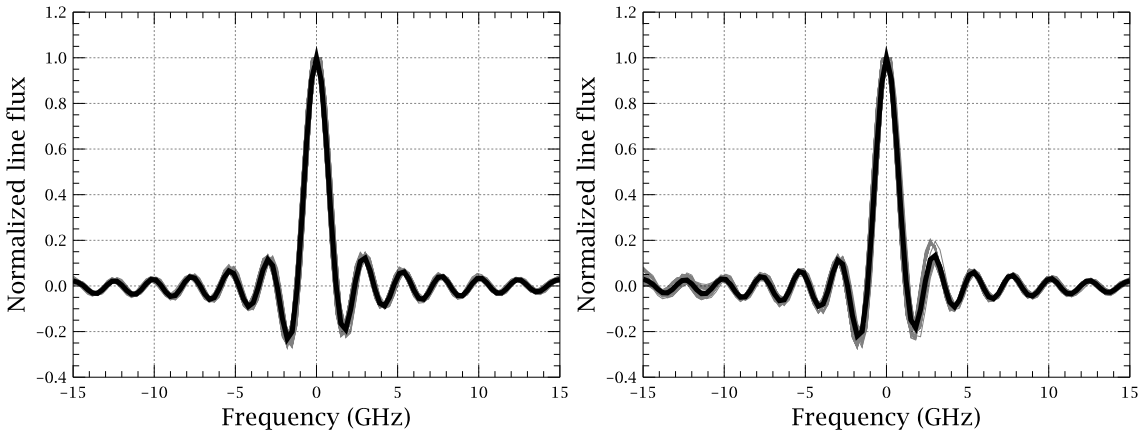

Figure 3.25: The FTS instrumental line shape, the *sinc* function. The average line shape (in black) for the two central detectors from unresolved CO lines in the HR spectrum of NGC 7027, SSWD4 (left) and SLWC3 (right). The grey curves show the line shapes for all 30 observations of NGC 7027.

a noticeable asymmetry in the first *sinc* minimum towards higher frequencies (i.e. at positive frequencies in Fig. 3.25), this effect is more pronounced for the SSWD4 detector. The reason for this asymmetry is a small residual phase shift in the interferograms (see Hopwood et al. 2015 for details). As a consequence, the integrated line flux derived from a canonical *sinc* function is systematically underestimated by 2.6%.

For the *sinc* function, the spectral resolution (in the natural units of wavenumbers) $\Delta\sigma$ is the distance from the peak to the first zero crossing, i.e. $\Delta\sigma = 1/(2L_{\rm max})$, where $L_{\rm max}$ is the maximum optical path difference created by the scan mirror travel. The wavenumbers are converted to frequencies using Δf (GHz) = $10^{-7}\, c\, \Delta\sigma$ (cm^{-1}), where c is the speed of light. There were three observing modes with three different $L_{\rm max}$, although only two were used for science observations: HR with $\Delta f = 1.2$ GHz and LR with $\Delta f = 25$ GHz. The FWHM in km s^{-1} of an unresolved line for the HR mode is:

$$\mathrm{FWHM(km\,s^{-1})} = 1.20671\, \Delta f\, \lambda = 1.4472 \left(\frac{\lambda}{\mu\mathrm{m}}\right). \tag{3.1}$$

Hence the line FWHM for the SSW is between 280–450 km s^{-1} and between 440–970 km s^{-1} for the SLW. The resolving power $\lambda/\Delta\lambda = f/\Delta f$ ranges from 370 to 1288 at the two extremes of the FTS bands.

The spectral range and spectral resolution for the central detectors (SSWD4 and SLWC3, see Figure 2.6) also applies to the other detectors across the spectrometer arrays used for spectral mapping.

Wavelength scale accuracy

The FTS wavelength scale accuracy has been verified using line fits to the ^{12}CO lines in five Galactic sources with the theoretical instrumental line shape (*sinc* profile). The line centroid can be determined to within a small fraction of the spectral resolution element, $\sim 1/20^{th}$, if the signal-to-noise is high. There is a very good agreement between the different sources and across both FTS bands (see Swinyard et al. 2014 for more details).

Sensitivity

The current FTS sensitivity estimates[2] are given in greater detail in Hopwood et al. (2015). Figure 3.26 shows the current sensitivity estimates and compare them with the initial and revised HSpot values.

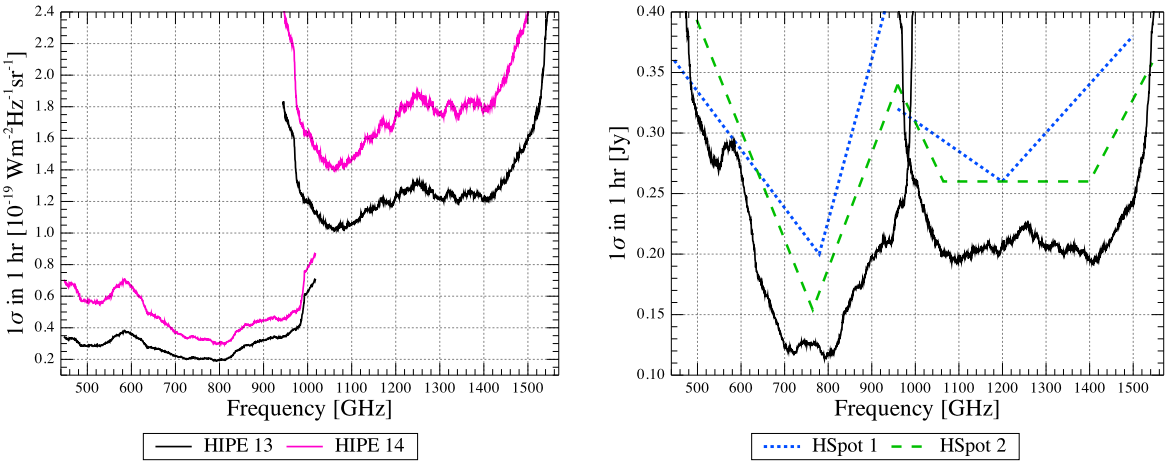

Figure 3.26: FTS sensitivity for extended-calibrated data (left) and point-source-calibrated data (right). The extended source calibration sensitivity is significantly underestimated for HIPE versions before v14 as the far-field feedhorn efficiency $\eta_{\rm ff}$ was not taken into account (see Section 6.1 for more details). The point-source-calibrated sensitivity is compared to the initial and revised HSpot values, which give the predicted sensitivity.

From Figure 3.26, and assuming an unresolved line[3], we can derive the integrated "1σ in 1 hour" line flux sensitivity of 2.4×10^{-18} W m^{-2} in [1100,1450] GHz (SSW) and between $(1.2 - 3.0) \times 10^{-18}$ W m^{-2} in [600,900] GHz (SLW).

A number of important points concerning the FTS sensitivity should be noted.

1. When using smoothed FTS spectra via apodization (the recommended apodized function is the extended Norton-Beer function 1.5; Naylor & Tahic 2007), the amplitude of the secondary maxima and minima of the *sinc* function can be reduced at the expense of broadening of the line, by a factor of 1.5, and consequently lowering the peak as the flux is conserved. Apodization is not recommended for spectra with many lines or lines with very low signal-to-noise.

2. The integrated line flux sensitivity for an unresolved line is in principle independent of the resolution for an FTS.

3. For point source observations, a sparse map covering the full FTS field of view is also generated. The full field of view is 2.6′ diameter, but the outer ring of detectors is partially vignetted. The unvignetted field of view is specified as 2′ diameter. Data from the full field of view are available.

[2]The sensitivity estimates are applicable for HIPE v13 and SPIRE calibration tree SPIRE_CAL_13_1.
[3]The unresolved line flux $F_{\rm line}({\rm W\,m^{-2}}) = 1.2 \times 10^{-17} \times p_0$, where p_0 is the line peak in Jy.

4. For very bright sources, a bright-source mode is available (Lu et al., 2014). The sensitivity for this mode is reduced, compared to the nominal mode, by a factors of approximately 2 for the SLW array and 4 for the SSW array. Guidance on the use of the bright source mode is provided in Section 6.7.

5. As for the photometer, the maximum achievable SNR should be taken as 200.

6. For spectral mapping:

   (a) Integrated line flux sensitivity is essentially the same as for point source for a given map point (in terms of W m^{-2} in beam).

   (b) For a fully sampled map, spatial pixels in the spectral cube can be co-added/resized to enhance sensitivity (as in the photometer), but it is best to assume no enhancement in sensitivity as calibration errors or other imperfections may counteract the gain that is available in principle.

Chapter 4

Calibration sources and models

SPIRE flux calibration is based on Neptune for the photometer and on *Herschel* telescope and Uranus for the spectrometer. The SPIRE calibration programme also includes observations of Mars, Saturn asteroids, and stars to enable a consistent and reliable flux calibration and cross-calibration with PACS and HIFI, and with other facilities. The currently assumed planet, asteroid and stellar models are briefly described below for information.

More detailed analysis of the SPIRE calibration targets are presented in Lim et al. (2016, in preparation) for the Photometer and in Hopwood et al. (2015) for the Spectrometer.

4.1 Neptune and Uranus models

Models of Uranus and Neptune have been agreed by the *Herschel* Calibration Steering Group (HCalSG) as the current standards for *Herschel*, and are available on the HSC calibration ftp site[1]. The models currently used for SPIRE are the "ESA-4" tabulations for both Uranus (based on Orton et al. 1986, 2014) and for Neptune (based on the updated model of Moreno 1998, 2010). The absolute systematic flux uncertainty for Neptune is estimated to 4% (R. Moreno, private communication), while comparing Uranus and Neptune, the absolute uncertainties are of the order of 3% (Swinyard et al., 2014). The consistency of the models within the SPIRE ranges were further confirmed in Hopwood et al. (2015).

The Uranus and Neptune disk-averaged brightness temperature spectra are plotted in Figure 4.1. In the *Herschel* range, the disk averaged brightness temperatures increase with wavelength as deeper layers in the atmosphere are probed. The planets have similar temperatures, despite Neptune's greater distance from the Sun, because Neptune has an internal heat source. This also leads to a more dynamic Neptunian atmosphere resulting in some prominent spectral features whereas the Uranian spectrum is largely featureless (see e.g. Teanby & Irwin 2013).

Typical photometer (250, 350, 500) μm calibration flux densities (see Chapter 5 for precise definition) are (160, 100, 60) Jy for Neptune and (370, 250, 150) Jy for Uranus.

Neptune and Uranus angular sizes are important parameters in the flux calibration scheme. The adopted equatorial radii (1-bar level, r_{eq}) and eccentricities (e) for Uranus and Neptune are summarised in Table 4.1 and are based on the analysis of Voyager data by Lindal et al. (1987) and Lindal

[1] ftp://ftp.sciops.esa.int/pub/hsc-calibration/PlanetaryModels/

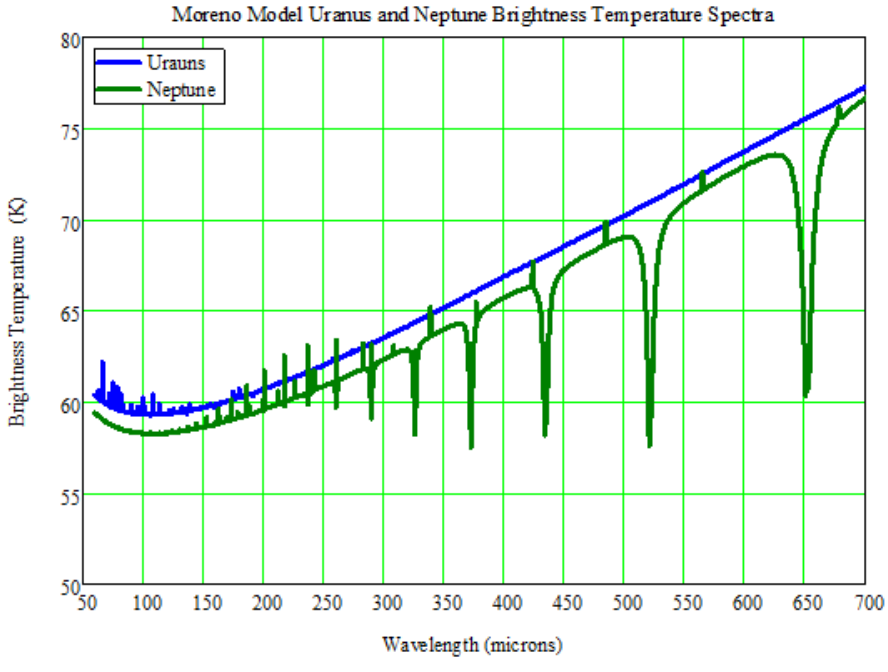

Figure 4.1: Currently adopted models (Moreno, 2010; Orton et al., 2014) of the brightness temperature spectra of Uranus and Neptune.

(1992). These are similar to the values used in the ground-based observations by Griffin & Orton (1993), Hildebrand et al. (1985) and Orton et al. (1986).

In calculating the planetary angular sizes and solid angles, a correction is applied for the inclination of the planet's axis at the time of observation, and the apparent polar radius is given by (Marth, 1897):

$$r_{p-a} = r_{eq}\left[1 - e^2\cos^2(\phi)\right]^{1/2}, \tag{4.1}$$

where ϕ is the latitude of the sub-*Herschel* point, and e is the planet's eccentricity:

$$e = \left[\frac{r_{eq}^2 - r_p^2}{r_{eq}^2}\right]^{1/2}. \tag{4.2}$$

The observed planetary disc is taken to have a geometric mean radius, r_{gm}, given by

$$r_{gm} = \left(r_{eq}.r_{p-a}\right)^{1/2}. \tag{4.3}$$

For a Herschel-planet distance of D_H, the observed angular radius, θ_p, and planet solid angle, Ω_p, are thus

$$\theta_p = \frac{r_{gm}}{D_H} \text{ and } \Omega_p = \pi\theta_p^2. \tag{4.4}$$

Typical angular radii for Uranus and Neptune are $1.7''$ and $1.1''$ respectively.

Table 4.1: Adopted planetary radii and eccentricity values.

Planet	Equatorial radius r_{eq} (km)	Polar radius r_p (km)	Eccentricity Eq. (4.2)	Reference
Uranus	$25,559 \pm 4$	$24,973 \pm 20$	0.2129	Lindal et al. (1987)
Neptune	$24,766 \pm 15$	$24,342 \pm 30$	0.1842	Lindal (1992)
Uranus	25,563	24,949	0.024	Griffin & Orton (1993)
Neptune	24,760	24,240	0.021	Hildebrand et al. (1985) Orton et al. (1986)

4.2 Mars models

Web-based models of the martian continuum by Emmanuel Lellouch, H. Amri and Bryan Butler are available at http://www.lesia.obspm.fr/perso/emmanuel-lellouch/mars/ and http://www.aoc.nrao.edu/~bbutler/work/mars/model/.

Mars is a very bright source for SPIRE. For example, at the time of its observation by SPIRE on 29 Oct 2009 (*Herschel* operational day 168 or OD 168) it had flux densities of (9300, 5000, 2500) Jy at (250, 350, 500) μm. The nominal *Herschel* telescope background is equivalent to approximately (230, 250, 270) Jy, so that Mars is equivalent to (40, 20, 10) time the nominal telescope brightness.

The Mars model was used to validate the Spectrometer bright source mode, see Lu et al. (2014) for details.

4.3 Asteroid models

The larger asteroids can also be used as FIR/submillimetre calibration sources, and were particularly important in the early part of the mission when Uranus and Neptune were not visible. The use of asteroids in the calibration of the three *Herschel* instruments is presented in detail in Müller et al. (2014). The most accurate asteroid models are the thermophysical models of Müller & Lagerros (2002); Müller et al. (2014), which have been tabulated by Müller (2009) and must be computed in detail for a given observation date and time (there can be significant variations in brightness associated with the asteroid rotation period). For planning and estimation purposes, the asteroid Standard Thermal Model (STM, Lebofsky et al. 1986) can be used to estimate the expected flux densities.

As an illustration, STM spectra for 9 Dec 2009 are shown in Figure 4.2 for the four largest asteroids, 1-Ceres, 2-Pallas, 3-Juno, and 4-Vesta. Note that STM asteroid spectra are all of approximately the same shape, close to that of a Rayleigh-Jeans black-body: the monochromatic flux density ratios are typically 1.98 for S_{350}/S_{500} and 3.7–3.8 for S_{250}/S_{500}, where S_{250}, S_{350} and S_{500} are the flux densities in the three SPIRE Photometer bands.

The initial SPIRE photometer flux calibration was based on observations of 1-Ceres on OD 50 (02 July 2009), for which Ceres thermal spectrum was derived using the STM. This initial calibration has now been superseded by the Neptune-based calibration.

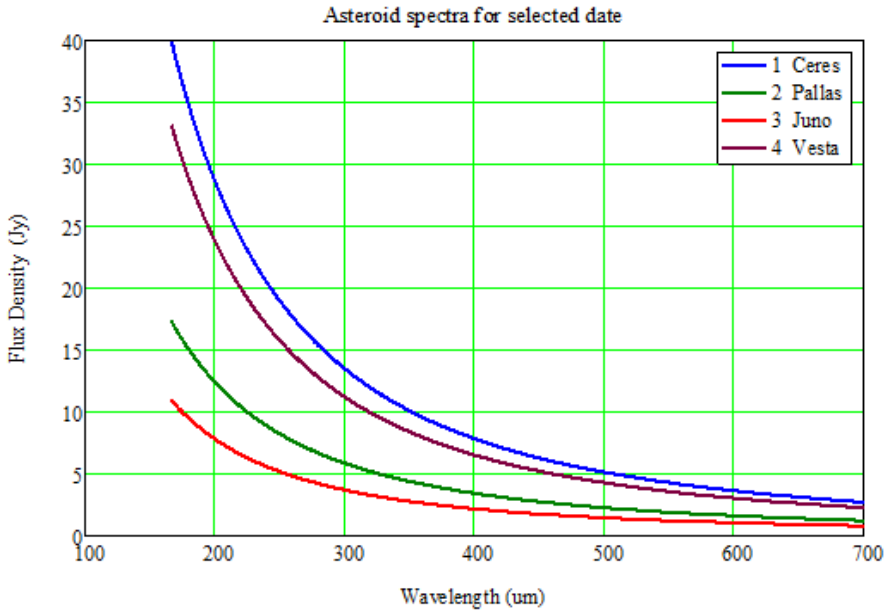

Figure 4.2: Standard Thermal Model spectra of 1-Ceres, 2-Pallas, 3-Juno, and 4-Vesta for Dec. 9 2009.

4.4 Stellar calibrators

At present, the PACS photometer calibration is based on a set of standard stars identified by the *Herschel* Calibration Steering group (HCalSG). These stars are also being observed by SPIRE as part of the SPIRE-PACS cross-calibration programme, which will include detailed comparison of the stellar-based and Neptune-based calibrations. The eight stars are: α Boo, α Tau, γ And, β Peg, γ Dra, Sirius, and α Cet.

Model spectra for these stars have been generated by Leen Decin based on the MARCS stellar atmosphere code of Decin & Eriksson (2007), covering 2-200 μm. The quoted estimated uncertainty is 1% for that wavelength range. Figure 4.3 shows the model FIR SEDs for the eight stellar calibrators with extrapolations to the SPIRE photometer bands based on the spectral index, α, in the 150-200 μm range. The latter is fairly uniform, varying between -1.99 and -2.034 for the eight sources. Computations covering wavelengths up to 700 μm are awaited. In the meantime, the available SEDs can be extrapolated with reasonable accuracy to SPIRE wavelengths, assuming no excess emission due to a chromospheric component or to a cold dust component around the star. The presence of any such excess would lead to a higher flux density, so the extrapolated figures can be taken as lower limits.

4.5 Dark sky

The location of the dark sky field was carefully chosen to be always visible to *Herschel*, in a region with no bright sources and with very low galactic foreground emission. The actual position of the dark sky is RA = 265.05 deg, Dec = 65.0 deg (J2000.0), close to the North Ecliptic Pole. A snapshot of the FTS footprint on the photometer map of the dark sky region is shown in Figure 4.4.

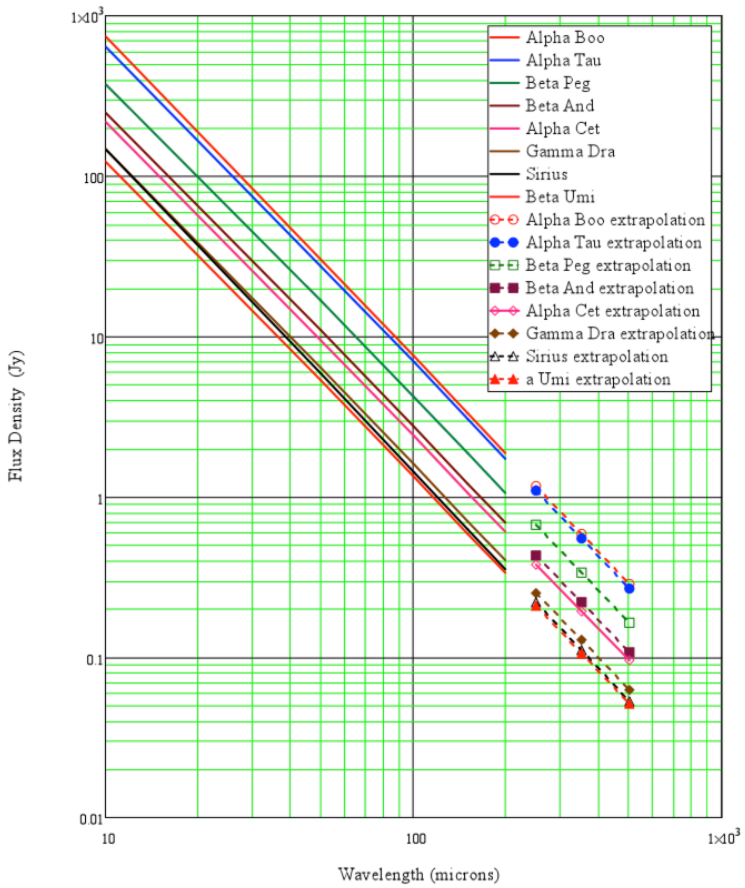

Figure 4.3: FIR SEDs model for the eight stellar calibrators with extrapolations to the SPIRE photometer bands using Decin & Eriksson (2007).

A spectrometer dark sky observation was performed during each *Herschel* operational day when the instrument was in use. A photometer map of the dark sky region was also obtained periodically during Photometer days. The dark sky observations are used in the Photometer flux calibration scheme (see Section 5.3) and to improve FTS calibration as it represents the telescope and instrument response to a "zero level" signal (see Chapter 6 for more details).

All dark sky and calibration observations performed with standard observing modes (see Chapter 3) are publicly available from the *Herschel* Science Archive (HSA).

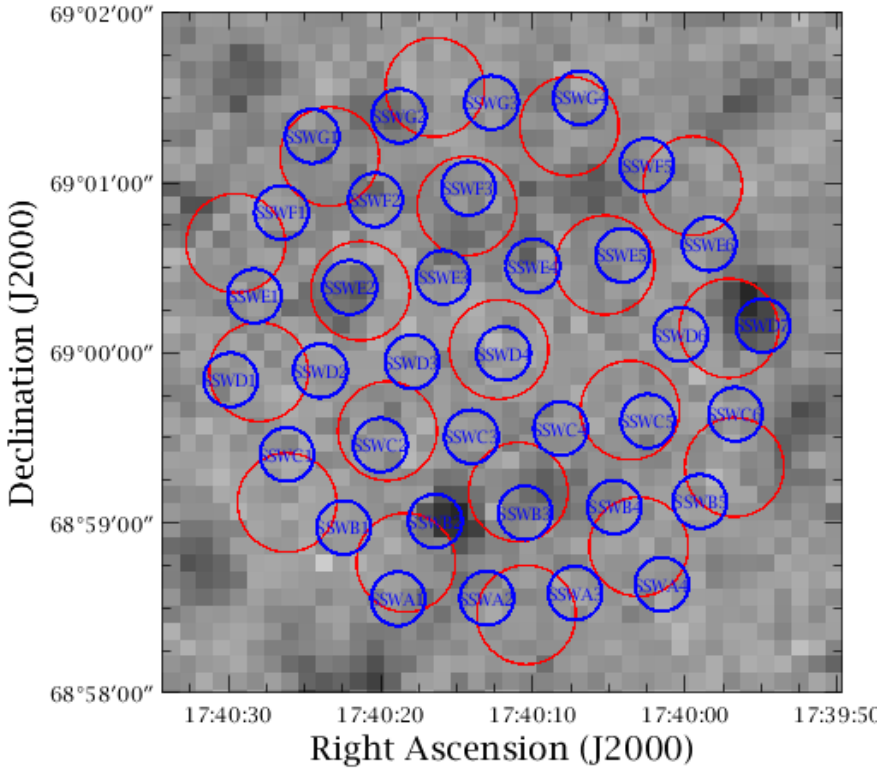

Figure 4.4: SPIRE FTS footprint at the location of the standard dark sky centre: RA=265.05 deg, Dec=+69 deg (J2000.0). The background image is the SPIRE photometer map at 250 μm, using negative colour table, i.e. the higher the flux the darker the pixel. The brightest source visible in this snapshot, WISE J174015.22+685901.4, near detector SSWB2, has flux densities of $\sim$ (50, 30, 20) mJy at (250, 350, 500) μm. Note that the FTS footprint will rotate around the central detector SSWD4 depending on the observing date.

Chapter 5

SPIRE Photometer flux calibration

The information in this chapter is based on Griffin et al. (2013) and Bendo et al. (2013).

The photometer pipeline produces monochromatic in-beam flux densities (Jy/beam) at standard frequencies corresponding to 250, 350 and 500 μm, and calculated under the assumptions of (i) a point source observation and (ii) a flat νS_ν spectrum, i.e. $\nu S_\nu = \mathrm{const}$. The calibration is carried out at the level of the detector timelines (Level-1 data products). The SPIRE Level-2 photometer products (maps) are also calibrated in terms of in-beam flux density (Jy/beam), though starting with HIPE v10 additional surface brightness products are available. These are calibrated in units of MJy/sr assuming an infinitely extended source with $\nu S_\nu = \mathrm{const}$, and the zero level is offset to match the absolute level from Planck maps.

5.1 Photometer Relative Spectral Response Function

In a SPIRE photometer observation, the property of the source that is directly proportional to source power absorbed by the bolometer is the integral over the passband of the flux density weighted by the instrument Relative Spectral Response Function (RSRF) and aperture efficiency:

$$\bar{S}_S = \frac{\int\limits_{Passband} S_S(\nu) R(\nu) \eta(\nu)\, \mathrm{d}\nu}{\int\limits_{Passband} R(\nu)\eta(\nu)\, \mathrm{d}\nu}, \tag{5.1}$$

where $S_S(\nu)$ represents the in-beam source flux density at the telescope aperture, $R(\nu)$ is the RSRF and $\eta(\nu)$ is the aperture efficiency[1]. The passband used in the integration is the same for all three bands, from 300 to 1800 GHz, interpolating $R(\nu)$ and $\eta(\nu)$ on the same frequency grid with 0.1 GHz step.

The three photometer RSRFs and aperture efficiencies are shown in Figure 5.1. The solid lines correspond to the overall filter transmission functions, and give the RSRFs, $R(\nu)$, for the case of a point source. The dashed lines give the aperture efficiency, $\eta(\nu)$, again for a point source. Note that the absolute vertical scale in Figure 5.1 is irrelevant to the computations here as all relevant parameters involve ratios of RSRF integrals. The RSRF curves and aperture efficiencies can be accessed in the SPIRE Calibration Tree in the *Herschel* Interactive Processing Environment (HIPE).

[1]The aperture efficiency is the frequency dependent on-axis response of the coupling of the telescope optics, including the feedhorn, to the sky.

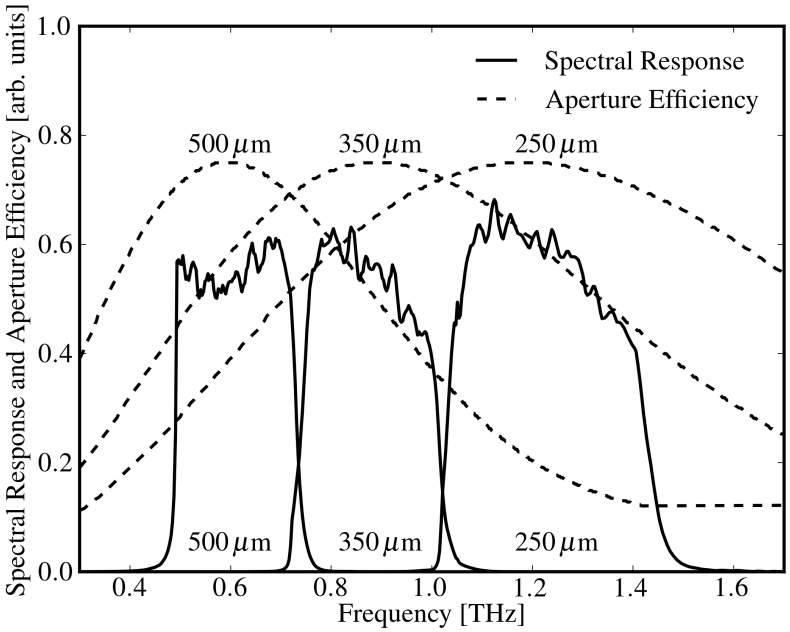

Figure 5.1: Photometer RSRFs and aperture efficiencies: $R(\nu)$ (solid lines), $\eta(\nu)$ (dashed lines).

5.2 Calibration flux densities

When observing a calibration source, the property that is directly proportional to the in-band power is

$$\bar{S}_{\rm Calib} = K_{\rm Beam} \frac{\int\limits_{Passband} S_C(\nu) R(\nu)\, \eta(\nu)\, {\rm d}\nu}{\int\limits_{Passband} R(\nu)\, \eta(\nu)\, {\rm d}\nu}, \tag{5.2}$$

where S_C is the calibrator flux density at the telescope aperture. The slightly extended appearance of the prime calibrator Neptune at SPIRE wavelengths is accounted for with the beam correction factor $K_{\rm Beam}$. For a Gaussian beam profile coupled to a uniformly bright disk (planet or asteroid), the beam correction factor is given by (e.g. Ulich & Haas 1976):

$$K_{\rm Beam}(\theta_p, \theta_{\rm Beam}) = \frac{1-\exp(-x^2)}{x^2};\; x = \sqrt{4\ln(2)} \left(\frac{\theta_p}{\theta_{\rm Beam}} \right), \tag{5.3}$$

where θ_p is the angular radius of the disk, and $\theta_{\rm Beam}$ is the beam FWHM. This derivation assumes the source is perfectly centred in the beam. The corresponding (250, 350, 500) μm beam correction factors are small: 0.995, 0.997, 0.999 for Neptune.

$\bar{S}_{\rm Calib}$ for Neptune, derived using the "ESA-4 model" $S_C(\nu)$ of Moreno (2010), has been used in the derivation of the flux density conversion parameters that are applied in the pipeline, and which are in turn used to derive the RSRF-weighted source flux density $\bar{S}_S$.

5.3 Response of a SPIRE bolometer to incident power

The output signal voltage of a SPIRE bolometer depends on the absorbed signal power, which is in turn a function of the source power collected by the telescope. For NTD bolometers with a given applied bias voltage, the small-signal responsivity varies with the voltage across the bolometer with an approximately linear relationship over a wide range of background loading and bath temperature conditions (Griffin, 2007). This translates to a corresponding relationship for the differential sensitivity of the system to the RSRF-weighted flux density, $\bar{S}$:

$$\frac{\mathrm{d}V}{\mathrm{d}Q} \propto V \;\Rightarrow \frac{\mathrm{d}V}{\mathrm{d}\bar{S}} \propto V. \tag{5.4}$$

To allow for the fact that the responsivity-operating point voltage relationship will not be exactly linear, we let

$$\frac{\mathrm{d}\bar{S}}{\mathrm{d}V} = f(V). \tag{5.5}$$

Note that:

1. $f(V)$ is specific to a particular bolometer and bias setting;
2. $f(V)$ is negative (since absorbed power causes a decrease in bolometer voltage); however, in the rest of this document we take it to be positive for convenience, assuming that a correction factor of -1 is applied.

In order to obtain $\bar{S}$ we need to integrate $f(V)$. Various fitting functions for $f(V)$ have been investigated and it is found that the most suitable function is of the form:

$$f(V) = K_1 + \frac{K_2}{V - K_3}, \tag{5.6}$$

where K_1, K_2 and K_3 are constants. K_1 has units of Jy V^{-1}, K_2 has units of Jy, and K_3 has units of V.

An example plot of $f(V)$ vs. V is shown Figure 5.2, and corresponds to a typical SPIRE 350 μm bolometer. The nominal operating point (blank sky) in this case would be close to 3 mV, and the range covers a sky brightness range up to more than 10 times the telescope brightness. The blue points are derived from a bolometer model, and the red line corresponds to the best fit K-parameters using Eq. (5.6).

A flux density corresponding to a measured RMS bolometer voltage, V_m, can be derived by integrating the above expression between some fixed bolometer voltage, V_0, and V_m:

$$\bar{S} = \int_{V_0}^{V_m} f(V)\mathrm{d}V = \int_{V_0}^{V_m} \left(K_1 + \frac{K_2}{V - K_3}\right) \mathrm{d}V, \tag{5.7}$$

so

$$\bar{S} = K_1(V_m - V_0) + K_2 \ln\left(\frac{V_m - K_3}{V_0 - K_3}\right). \tag{5.8}$$

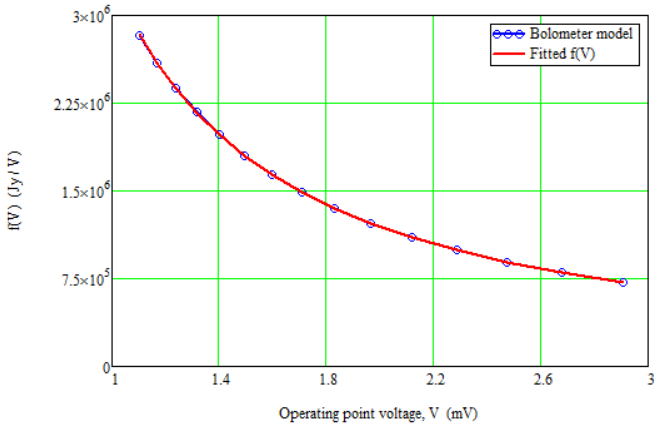

Figure 5.2: Typical plot of $f(V)$ vs. V (for a nominal 350 μm bolometer). The blue points correspond to the bolometer model and the red line is the fitted function using Eq. (5.6).

Ideally, V_0 would be the bolometer voltage in the absence of any astronomical signal (i.e., what would be measured when observing blank sky in otherwise identical conditions). The resulting flux density would correspond to that from the sky calibrated with respect to the blank sky level. V_0 is therefore derived from standard calibration observations of a fiducial "dark" area of sky (see Section 4.5) in scan-map mode under the nominal conditions: bias voltage and frequency, bolometer and instrument FPU (Level-1) temperature, and telescope temperature.

While bias voltage and Lock-In frequency are extremely stable, the temperatures of the bolometers and instrument FPU are floating, resulting in large thermally-induced bolometer voltage excursions. Thus in science measurements V_0 differs from the dark reference value by an additive amount that is typically larger than most astronomical signals. This means that the raw flux density values produced by the pipeline have additive offsets (different for each bolometer) that must be removed before map-making to derive the flux density from the sky. The removal of these offsets is known as "baseline removal" or "destriping" in the SPIRE pipeline jargon.

Values of K_1, K_2 and K_3 have been derived from calibration observations (Bendo et al., 2013), and are used in the pipeline flux conversion module together with the standard colour correction parameter $K_{\rm MonP}$ (see the next subsection) to produce the SPIRE monochromatic flux density timelines.

5.4 Conversion of RSRF-weighted flux density to monochromatic flux density for point sources

The definition of a monochromatic flux density requires the adoption of a standard reference frequency/wavelength for the band and some assumption about the shape of the source spectrum. For SPIRE (and PACS) we assume that the spectrum is a power law across the band defined by the flux density at a reference frequency ν_0, and a spectral index $\alpha_S = -1$ (corresponding to $\nu S_S(\nu)$ = const. across the band):

$$S_S(\nu) = S_S(\nu_0) \left(\frac{\nu}{\nu_0} \right)^{\alpha_S} . \tag{5.9}$$

For the standard SPIRE pipeline, we choose values of ν_0 to correspond to wavelengths of 250, 350 and 500 μm for the three bands. Therefore the pipeline generates monochromatic flux densities for the bolometer timelines at those frequencies.

Under these assumptions, the measured RSRF-weighted flux density (the in-band power, weighted by the source spectrum and the RSRF, to which the bolometer output voltage due to the source is proportional in the linear regime) is thus

$$\bar{S}_S = \frac{\int\limits_{Passband} S_S(\nu) R(\nu) \eta(\nu) \mathrm{d}\nu}{\int\limits_{Passband} R(\nu) \eta(\nu) \mathrm{d}\nu} = \frac{S_S(\nu_0)}{\nu_0^{\alpha_S}} \left[\frac{\int\limits_{Passband} \nu^{\alpha_S} R(\nu) \eta(\nu) \mathrm{d}\nu}{\int\limits_{Passband} R(\nu) \eta(\nu) \mathrm{d}\nu} \right], \tag{5.10}$$

where $R_\eta(\nu) = R(\nu)\,\eta(\nu)$, $R(\nu)$ is the RSRF and $\eta(\nu)$ is the aperture efficiency.

The monochromatic source flux density at frequency ν_0, which is produced by the pipeline, is therefore given by:

$$S_S(\nu_0) = \bar{S}_S \left[\frac{\nu_0^{\alpha_S} \int\limits_{Passband} R(\nu) \eta(\nu) \mathrm{d}\nu}{\int\limits_{Passband} \nu^{\alpha_S} R(\nu) \eta(\nu) \mathrm{d}\nu} \right] = K_{\mathrm{MonP}}(\alpha_S, \nu_0)\, \bar{S}_S. \tag{5.11}$$

The measured RSRF-weighted flux density is thus multiplied by $K_{\mathrm{MonP}}(\alpha_S, \nu_0)$ to derive the monochromatic flux density at the reference wavelength to be quoted to the user.

The standard SPIRE pipeline assumes $\alpha_S = -1$ and we can introduce the conversion parameter $K_{4\mathrm{P}}(\nu_0)$ as:

$$K_{4\mathrm{P}}(\nu_0) = K_{\mathrm{MonP}}(\alpha_S = -1, \nu_0) = \frac{1}{\nu_0} \frac{\int\limits_{Passband} R(\nu) \eta(\nu) \mathrm{d}\nu}{\int\limits_{Passband} \nu^{-1} R(\nu) \eta(\nu)\, \mathrm{d}\nu}. \tag{5.12}$$

Therefore all pipeline timelines are converted to monochromatic flux densities using

$$S_{\mathrm{pip}}(\nu_0) = K_{4\mathrm{P}}(\nu_0)\, \bar{S}_S, \tag{5.13}$$

where $\bar{S}_S$ is the in-band RSRF weighted flux density in Jy/beam, derived using the K-parameters (see Eq. 5.8).

Following this convention, the peak value of a calibrated SPIRE Level-1 timeline reflects the flux density of a point source with a flat SED (i.e. $\nu S_S(\nu) = \mathrm{const}$), at the reference wavelength of the passband, when the associated bolometer is moved centrally across that source.

The conversion from the pipeline output $S_{\mathrm{pip}}(\nu_0)$ to $S_S(\nu_0)$ for a source with a particular spectral shape is achieved through applying a colour correction; this is discussed in Sections 5.6 and 5.7.

5.5 Conversion of RSRF-weighted flux density to monochromatic surface brightness for fully extended sources

Previous versions of this document (up to and including v2.4) advised a different method of extended source calibration than recommended here. They advised using a conversion parameter with λ^2-weighted RSRF to approximate the beam variation across the band, giving the in-beam flux density. The conversion to surface brightness was then achieved by dividing by the beam area.

The method was not completely accurate for two reasons, as shown in greater detail in Griffin et al. (2013). Firstly, the beam solid angle does not scale with λ^2 but as $\lambda^{1.7}$ due to the finite size of the *Herschel* optics. Secondly, because sources with different spatial and spectral variations illuminate the aperture in a different way, and the collecting aperture varies across the filter passband, there is not a single value for the beam area that is appropriate for all source types. See Section 5.12.1 for an indication of the effect of these changes.

In the following we will concentrate on the extreme case of an infinitely extended source. Such sources are characterised by their surface brightness, $I_S(\nu)$, usually measured in MJy/sr. Following the same convention as for point sources, we assume a source with a power-law spectrum of index α_S in-band, i.e $I_S(\nu) = I_S(\nu_0)\,(\nu/\nu_0)^{\alpha_S}$. It is also assumed that the source uniformly fills the entire beam, and that the beam has a frequency-dependent solid angle, $\Omega_\nu(\nu)$ This variation is discussed in Section 5.9. Under these assumptions the measured RSRF-weighted flux density is thus

$$\bar{S}_S = \frac{\int_{Passband} I_S(\nu)\, R(\nu)\, \eta(\nu)\, \Omega_\nu(\nu)\, \mathrm{d}\nu}{\int_{Passband} R(\nu)\, \eta(\nu)\, \mathrm{d}\nu} = \frac{I_S(\nu_0)}{\nu_0^{\alpha_S}} \left[\frac{\int_{Passband} \nu^{\alpha_S} R(\nu)\eta(\nu)\Omega_\nu(\nu)\mathrm{d}\nu}{\int_{Passband} R(\nu)\eta(\nu)\mathrm{d}\nu}\right]. \quad (5.14)$$

The monochromatic source surface brightness at frequency ν_0 is therefore given by

$$I_S(\nu_0) = \bar{S}_S \left[\frac{\nu_0^{\alpha_S} \int_{Passband} R(\nu)\eta(\nu)\mathrm{d}\nu}{\int_{Passband} \nu^{\alpha_S} R(\nu)\eta(\nu)\Omega_\nu(\nu)\mathrm{d}\nu}\right] = K_{\mathrm{MonE}}(\alpha_S, \nu_0)\, \bar{S}_S. \quad (5.15)$$

and so the conversion parameter $K_{\mathrm{MonE}}(\alpha_S, \nu_0)$ is given by

$$K_{\mathrm{MonE}}(\alpha_S, \nu_0) = \frac{\nu_0^{\alpha_S} \int_{Passband} R(\nu)\eta(\nu)\mathrm{d}\nu}{\int_{Passband} \nu^{\alpha_S} R(\nu)\eta(\nu)\Omega_\nu(\nu)\mathrm{d}\nu}. \quad (5.16)$$

From HIPE v10 and above an additional set of SPIRE maps are provided in units of MJy/sr. As with the point source pipeline, the pipeline in-band RSRF-weighted flux density timelines $\bar{S}_S$ are converted to monochromatic surface brightness using $K_{\mathrm{MonE}}(\nu_0)$, assuming a source with $\alpha_S = -1$:

$$I_{\mathrm{pip}}(\nu_0) = K_{\mathrm{MonE}}(\alpha_S = -1, \nu_0)\, \bar{S}_S, \quad (5.17)$$

where, as before, the in-band flux density $\bar{S}_S$ in Jy/beam is derived using the K-parameters (Eq. 5.8).

The processing for extended source calibrated maps, however, involves some additional steps:

1. Relative gain factors are applied to the signal of each bolometer ($\bar{S}_S$), taking into account small differences in the ratio between peak and integral between individual bolometers. Correcting in this way for the sensitivities of the individual bolometers to an extended source improves the consistency of photometric gains of bolometers, reducing residual striping in maps with predominantly extended sources.

2. The maps are zero-point corrected based on the *Planck*-HFI maps (see Section 5.10). This is a constant offset applied to the entire map.

There are some cases in which users may wish to convert SPIRE point-source calibrated maps to extended-source calibrated maps. Because the first step above, namely applying the relative gains factors, cannot be replicated by a simple multiplicative factor, the user needs to apply those to all individual bolometer timelines, prior to the map making step. In cases where the point-source calibrated maps already include the relative gains then the conversion can be achieved by multiplying the point-source calibrated map by $K_{\rm PtoE}(\nu_0)$:

$$K_{\rm PtoE}(\nu_0) = \frac{K_{\rm MonE}(\alpha_S = -1, \nu_0)}{K_{\rm 4P}(\nu_0)} = \Omega_{\rm eff}(\alpha_S = -1). \tag{5.18}$$

where the value of $\Omega_{\rm eff}(\alpha_S = -1)$ is that used for the pipeline and the value of this parameter is given in Table 5.1. Note that multiplying the map by this parameter changes the units from flux density (Jy/beam) to surface brightness (MJy/sr).

The conversion from extended source calibrated pipeline output $I_{\rm pip}(\nu_0)$ to source surface brightness $I_S(\nu_0)$ of a source with a particular spectral shape is achieved through applying the colour correction, as discussed in Sections 5.6 and 5.7. It is important to note that since the extended-source calibrated maps are in units of surface brightness, they depend on the effective beam solid angle. The colour correction for such a map must therefore take into account the variation in the beam solid angle, and so is different from that for a point source (see Section 5.6).

The conversion from surface brightness (MJy/sr) to flux density (Jy/beam in general, or Jy for a true point-like source) is achieved by multiplying by the effective beam solid angle for the source in question (see Section 5.9.2, and (5.35)). For an extended source with the spectrum assumed in the pipeline ($\alpha_S = -1$), we can define a conversion parameter, $K_{\rm 4E}$, as is done with point sources in (5.12)–(5.13). Using (5.18) and (5.35), this can be written as

$$K_{\rm 4E} = K_{\rm MonE}(-1, \nu_0)\Omega_{\rm eff}(-1) = \frac{\nu_0^{-1} \int\limits_{Passband} R(\nu)\eta(\nu)\mathrm{d}\nu}{\int\limits_{Passband} \nu^{-1} R(\nu)\eta(\nu)\mathrm{d}\nu} = K_{\rm 4P}. \tag{5.19}$$

Note that the equality $K_{\rm 4E} = K_{\rm 4P}$ was not true in previous versions of this manual, accompanying HIPE v13 and previous, because the aperture efficiency, $\eta(\nu)$, was not included in the calculation of the beam solid angle.

5.6 Colour correction for power-law spectra

The assumption that the source has a spectrum with $\nu\, S_S(\nu)$ flat across the band will not be the case for most observations. For instance, at SPIRE wavelengths, planets and other solar system objects will typically have a spectral index of 2 (corresponding to black-body emission in the Rayleigh-Jeans region). Dust sources will typically have a steeper spectrum, with $\alpha_S \approx$ 3-4. Only for very cold dust or strongly redshifted sources will a power-law begin to fail being a good approximation. For the highest calibration accuracy a colour correction can be applied by the astronomer based on other information (for instance, measurements in other SPIRE or PACS bands and/or data from other telescopes). Depending on the nature and temperature of the source, the true spectral index could be different for the three SPIRE bands, as illustrated in Figure 5.3, which could apply in the case of a cold dust source.

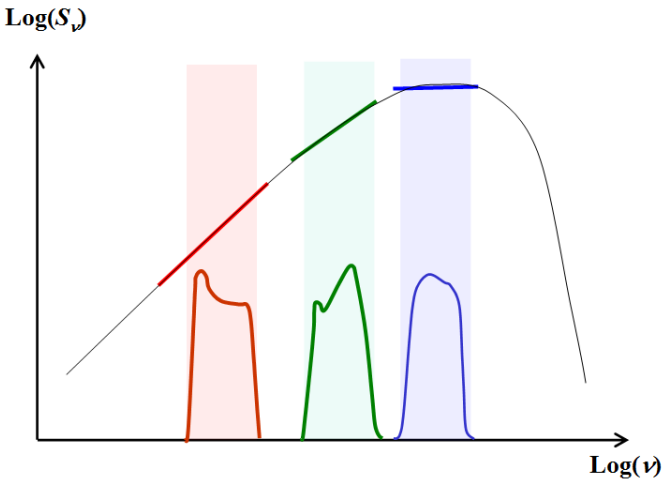

Figure 5.3: Illustration of the possibility of different source spectral indices for the three SPIRE bands.

Given the width of the SPIRE bands and the nature of the observed source SEDs, in many cases it will be appropriate to assume that the source spectrum follows a power law across the band, but with a different spectral index, α_N. Let $S'_S(\nu_0)$ be the point source flux density at ν_0 for that spectral shape. We then have from Eq. (5.11)

$$S'_S(\nu_0) = \nu_0^{(\alpha_N - \alpha_{\rm pip})} \left[\frac{\int_{Passband} R(\nu)\eta(\nu)\nu^{\alpha_{\rm pip}}\,{\rm d}\nu}{\int_{Passband} R(\nu)\eta(\nu)\nu^{\alpha_N}\,{\rm d}\nu} \right] S_{\rm pip}(\nu_0) = K_{\rm ColP}(\alpha_N)\, S_{\rm pip}(\nu_0). \quad (5.20)$$

Putting $\alpha_{\rm pip} = -1$ gives

$$K_{\rm ColP}(\alpha_N, \nu_0) = \nu_0^{(\alpha_N+1)} \left[\frac{\int_{Passband} R(\nu)\eta(\nu)\nu^{-1}\,{\rm d}\nu}{\int_{Passband} R(\nu)\eta(\nu)\nu^{\alpha_N}\,{\rm d}\nu} \right]. \quad (5.21)$$

The colour-correction $K_{\rm ColP}$ for sources of different power-law indices is tabulated in Table 5.6 and shown in Figure 5.4, left panel.

Similarly, for a fully extended source, the monochromatic source surface brightness at ν_0 can be derived from the extended pipeline output, which is provided in units of MJy/sr, as follows

$$I'_S(\nu_0) = K_{\rm ColE}(\alpha_N, \nu_0) I_{\rm pip}(\nu_0). \quad (5.22)$$

Putting $\alpha_{\rm pip} = -1$ into 5.19 and 5.17 gives

$$K_{\rm ColE}(\alpha_N, \nu_0) = \nu_0^{(\alpha_N+1)} \left[\frac{\int_{Passband} R(\nu)\eta(\nu)\Omega_\nu(\nu)\nu^{-1}\,{\rm d}\nu}{\int_{Passband} \nu^{\alpha_N} R(\nu)\eta(\nu)\Omega_\nu(\nu){\rm d}\nu} \right]. \quad (5.23)$$

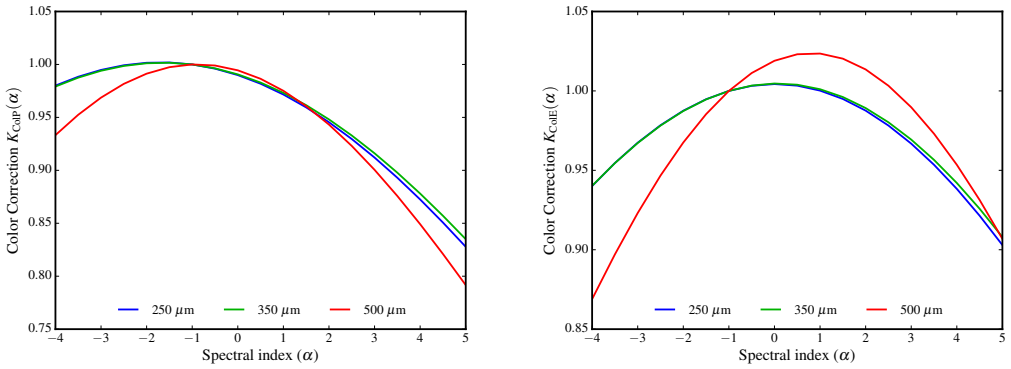

Figure 5.4: Colour correction parameters for point sources ($K_{\rm ColP}$, left) and extended sources ($K_{\rm ColE}$, right), vs. assumed source spectral index.

The colour-correction $K_{\rm ColE}$ for sources of different power-law indices is tabulated in Table 5.6 and shown in Figure 5.4, right panel. Note that in the calculation of $K_{\rm MonE}(\nu_0)$ and $K_{\rm ColE}(\nu_0)$ the monochromatic beam solid angle, $\Omega_\nu(\nu)$ is required, which is well described by a power frequency law with index -1.7 (see Section 5.9, Eq. 5.37).

It is important to note that these extended source colour corrections should only be applied to a map which is in surface brightness units, and which assumes $\alpha_S = -1$. If the map in question is in flux density units, i.e. Jy/beam, and the relative gains are already applied, then it should be converted to surface brightness first using the conversion $K_{\rm PtoE}$ in Eq. (5.18). Also note that this conversion parameter applies only to maps with the standard colour of $\alpha_S = -1$, and so any colour correction that has been applied should be reversed beforehand.

Table 5.1: Values of $K_{\rm 4P}$, $K_{\rm MonE}(\alpha = -1)$, $K_{\rm PtoE}$ and $\Omega_{\rm pip}$ for the three SPIRE bands. $K_{\rm 4P}$ is the pipeline point source flux conversion parameter; $K_{\rm MonE}(\alpha = -1)$ is the conversion to monochromatic surface brightness for an extended source with $\alpha = -1$; $K_{\rm PtoE}$ is the conversion from point source flux density to extended source surface brightness for a source spectrum $\alpha = -1$; $\Omega_{\rm pip}$ is the beam solid angle for a source with $\alpha_S = -1$, i.e. $\Omega_{\rm eff}(-1)$.

Band	PSW	PMW	PLW
Reference wavelength, λ_0 (μm)	250.0	350.0	500.0
Reference frequency, ν_0 (GHz)	1199.17	856.55	599.58
$K_{\rm 4P}$ & $K_{\rm 4E}$	1.0102	1.0095	1.0056
$K_{\rm MonE}$ (MJy/sr per Jy/beam)	91.567	51.665	23.711
$K_{\rm PtoE}$ (MJy/sr per Jy/beam)	90.646	51.181	23.580
$\Omega_{\rm pip}$ (arcsec^2)	469.35	831.27	1804.31

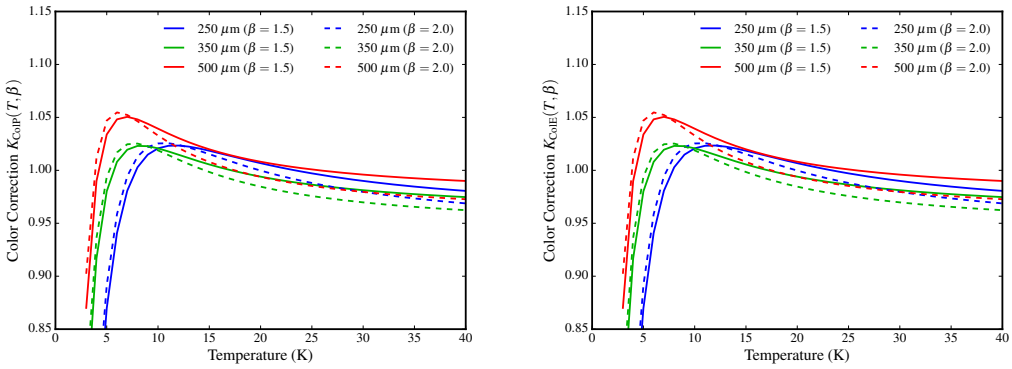

Figure 5.5: Colour correction parameters for point sources ($K_{\rm ColP}$, left) and extended sources ($K_{\rm ColE}$, right), vs. assumed modified blackbody source temperature. The colour correction factors are plotted for two values of emissivity index, $\beta = 1.5$ and $\beta = 2$.

5.7 Colour correction for modified black-body spectra

For some sources, the approximation to a power-law spectrum is not accurate. This is particularly true of sources with low blackbody temperatures. Assuming a modified blackbody (also known as a "greybody") with a spectrum $I_S = \nu^\beta \mathcal{B}(T,\nu)$, where β is the dust emissivity index and $\mathcal{B}(T,\nu)$ is the Planck blackbody function:

$$\mathcal{B}(T,\nu) = \frac{2h\nu^3}{c^2} \cdot \frac{1}{e^{h\nu/kT} - 1}, \tag{5.24}$$

we can follow the same procedure as for a power-law spectrum and derive the colour correction parameters:

$$K_{\rm ColP}(T,\beta,\nu_0) = \nu_0^{\beta-\alpha_{\rm pip}} \mathcal{B}(T,\nu_0) \times \left[\frac{\int_{Passband} \nu^{\alpha_{\rm pip}}\, R(\nu)\, \eta(\nu)\, {\rm d}\nu}{\int_{Passband} \nu^{\beta}\, \mathcal{B}(T,\nu)\, R(\nu)\, \eta(\nu)\, {\rm d}\nu} \right], \tag{5.25}$$

for a point source, and

$$K_{\rm ColE}(T,\beta,\nu_0) = \nu_0^{\beta-\alpha_{\rm pip}} \mathcal{B}(T,\nu_0) \times \left[\frac{\int_{Passband} \nu^{\alpha_{\rm pip}}\, R(\nu)\, \eta(\nu)\, \Omega_{\rm eff}(\nu)\, {\rm d}\nu}{\int_{Passband} \nu^{\beta}\, \mathcal{B}(T,\nu)\, R(\nu)\, \eta(\nu)\, \Omega_{\rm eff}(\nu)\, {\rm d}\nu} \right], \tag{5.26}$$

for an extended source. Note that $\alpha_{\rm pip} = -1$ by convention.

The colour-correction parameters $K_{\rm ColP}$ and $K_{\rm ColE}$ for modified blackbodies with $\beta = 1.5$ and 2 and temperatures from 3 to 40 K, are tabulated in Table 5.7 and shown graphically in Figure 5.5.

5.8 Colour correction for more general source properties

The colour corrections and beam areas given in the earlier sections assume the following source properties:

- A power-law or modified blackbody spectral energy distribution (SED).
- Either a point-like or completely uniform infinitely extended source.

A more general colour correction procedure is more appropriate when either one or both of these assumptions are not applicable. We can define the in-beam astronomical flux density at a given frequency ν as:

$$S(\nu) = \oint_{4\pi} B(\theta, \phi, \nu)\, I_\nu(\theta, \phi)\, \mathrm{d}\Omega, \tag{5.27}$$

where $\theta \in [0, \pi]$ is a radial angular offset from the beam centre, $\phi \in [0, 2\pi]$ is an azimuthal angular offset, $B(\theta, \phi, \nu)$ is the normalised frequency-dependent beam distribution, $I_\nu(\theta, \phi)$ is the sky intensity (surface brightness) distribution, and $\mathrm{d}\Omega$ is a solid angle element in the direction defined by (θ, ϕ).

If we assume that the spectral and spatial variations are independent, and we restrict ourselves to circularly symmetric source and beam distributions, then we can define the source radial profile, relative to a scale width θ_0, as $g(\theta, \theta_0)$ and define the source SED as $f(\nu, \nu_0)$, usually normalised at a fiducial frequency ν_0. Consequently, the in-band total power is

$$\bar{S}_S = I_{S_p}(\nu_0) \frac{\int_{Passband} f(\nu, \nu_0)\, y(\nu, \theta_0)\, R(\nu)\, \eta(\nu)\, \mathrm{d}\nu}{\int_{Passband} R(\nu)\, \eta(\nu)\, \mathrm{d}\nu}, \tag{5.28}$$

where $I_{S_p}(\nu_0)$ is the monochromatic peak surface brightness of the source and the parameter $y(\nu, \theta_0)$, which is the beam coupling with the source distribution, is given by

$$y(\nu, \theta_0) = \int_0^{\theta_{\mathrm{max}}} B(\theta, \nu)\, g(\theta, \theta_0)\, 2\pi\, \theta\, \mathrm{d}\theta, \tag{5.29}$$

where $B(\theta, \nu)$ is the monochromatic beam radial profile at frequency ν and θ_{max} is the maximum size of the beam maps (see Section 5.9).

The conversion from the in-band power to the monochromatic peak surface brightness is therefore given by a general form of K_{MonE} given by

$$K_{\mathrm{MonE}}(f, g, \nu_0) = \frac{\int_{Passband} R(\nu)\, \eta(\nu)\, \mathrm{d}\nu}{\int_{Passband} f(\nu, \nu_0)\, y(\nu, \theta_0)\, R(\nu)\, \eta(\nu)\, \mathrm{d}\nu}. \tag{5.30}$$

Note that for an infinitely extended source, where $g(\theta, \theta_0) \equiv 1$, the $y(\nu, \theta_0)$ parameter in Eq. (5.29) is simply the integral over the beam profile, and so is given by the monochromatic beam area $\Omega_\nu(\nu_0)$.

Combining Eqs. (5.30) and (5.16), we see that for a general source, characterised by spectral variation $f(\nu, \nu_0)$ and spatial variation $g(\theta, \theta_0)$, the colour correction required to convert from the extended

pipeline maps to the true peak surface brightness is

$$K_{\rm ColE}(f,g,\nu_0) = \frac{\int\limits_{Passband} (\nu/\nu_0)^{-1}\,\Omega_\nu(\nu)\,R(\nu)\,\eta(\nu)\,{\rm d}\nu}{\int\limits_{Passband} f(\nu,\nu_0)\,y(\nu,\theta_0)\,R(\nu)\,\eta(\nu)\,{\rm d}\nu}, \tag{5.31}$$

where $y(\nu,\theta_0)$ is as given in Eq. (5.29).

A straightforward application of this procedure for a Gaussian source distribution $g(\theta,\theta_0)$, where θ_0 is simply the characteristic scale, i.e. the FWHM of the Gaussian shape, is given in Griffin et al. (2013). As of HIPE v13, we provide a useful script[2], which can be used to calculate the colour-corrections for sources of different shapes $g(\theta,\theta_0)$: Gaussian, power law, tophat, exponential, linear, constant, linear with limits, as well as sources with different SEDs, i.e. $f(\nu,\nu_0)$: power-law or modified black-bodies.

Additionally, as of HIPE v13, we also provide a task `spireSynthPhotometry()` that calculates the synthetic photometry $S_{\rm pip}(\nu_0)$ (or $I_{\rm pip}(\nu_0)$ for a fully extended source) for an arbitrary input source spectrum $S_S(\nu)$ (or $I_S(\nu)$). The spectrum, for example, can be taken from observations with the SPIRE Spectrometer. This way the Photometer pipeline photometry can be properly compared with the observations of the Spectrometer.

5.9 Photometer beam maps and areas

Updated analysis of the SPIRE photometer beam data and resulting beam parameters are available on the SPIRE Public wiki[3] and comprise the following:

- new empirical beam maps based on fine-scan-map measurements of Neptune;
- the raw data used for the above;
- an updated analysis taking into account the diffuse and point-source backgrounds behind Neptune, i.e. the so called "shadow map" – the same background sky region when the planet moved away from it.
- a theoretical model including coverage of the sidelobes and low-level structure due to the secondary mirror supports;

5.9.1 Empirical beam maps

The empirical beam products consist of two sets of three beam maps, one for each photometer band. The product was derived from scan-map data of Neptune, performed using a custom "fine-scan" observing mode with the nominal source brightness setting, where the detector array and its surroundings were scanned at a distance of only 2-3″ between scan legs. In these fine-scan observations, each bolometer was scanned over Neptune in four different directions. The data were reduced using the

[2] The script is available in HIPE, under
`Scripts => SPIRE Useful Scripts => Photometer Calibration Bundle semi-ext`

[3] http://herschel.esac.esa.int/twiki/bin/view/Public/SpirePhotometerBeamProfile2

standard HIPE scan-map pipeline, the median baseline subtractor with a circular exclusion zone of $8'$ diameter, and the naïve map-maker. Each map constitutes an averaging in the map over all of the individual bolometers crossing the source, and represents the realistic point source response function of the system, including all scanning artefacts. It is worth noting that in a normal SPIRE scan-map, any individual source in the map will be covered by only a subset of bolometers, leading to low-level beam profile variations, from position to position in the map, about the average profile presented here. These beam products also represent the measurement of a source with a particular spectral shape, $\sim \nu^{1.29}, \nu^{1.42}, \nu^{1.47}$ for 250, 350, 500 μm respectively, i.e. different from the standard ν^{-1} reference spectrum assumed by the pipeline products. A source with a different spectral shape will produce slightly different beam parameters.

The beam maps for all three bands are displayed in log scaling in Figure 5.6. Four individual maps, one from each of the four observations from which the final beam products are derived, are also available should the user want to investigate the beam stability. The beam product maps are $\sim 10' \times 30'$ in scale and include the same extensions and header information as the nominal maps output from HIPE. There are two versions of each map, one high resolution with a $1''$ pixel scale, and another with the nominal SPIRE output map pixel scale of (6, 10, 14)$''$ per pixel for (250, 350, 500) μm. The data have also been normalised to give a peak flux of unity in all three bands.

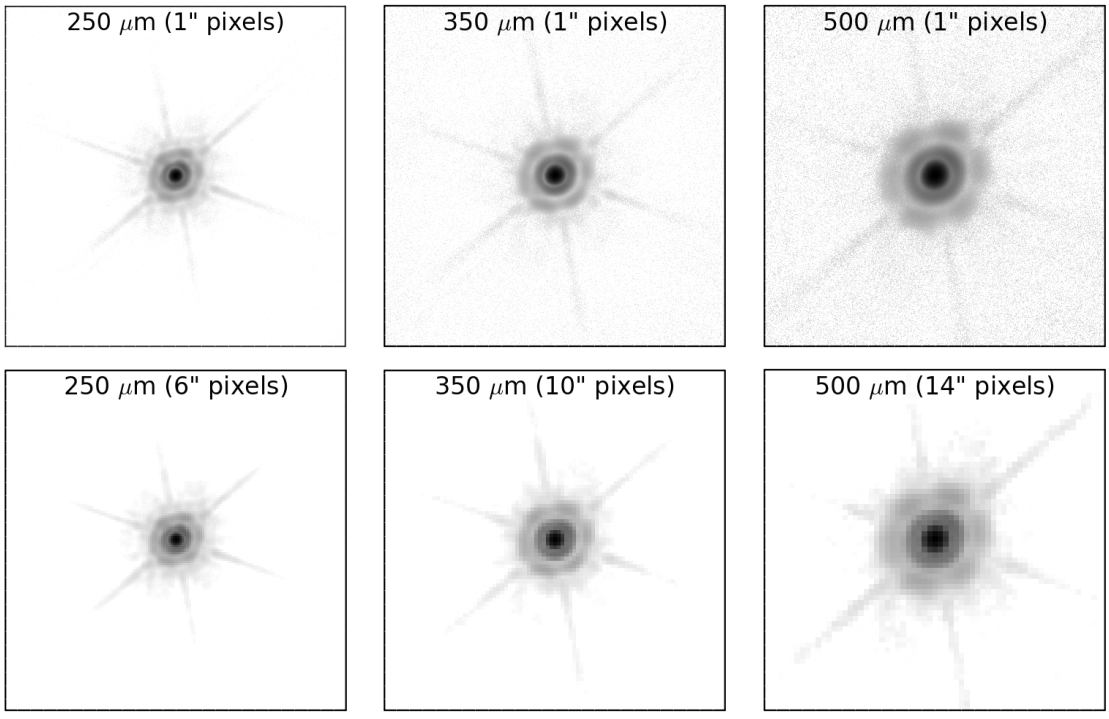

Figure 5.6: Log scale images for the empirical SPIRE beam model at 250, 350, and 500 μm from left to right respectively. The top row uses a $1''$ pixel scale for all maps, and the bottom row uses the nominal SPIRE map pixel scales of 6, 10, and $14''$ from left to right respectively.

Note that the ellipticity seen in the maps is not a function of scanning direction, but is constant with position angle. When using these beam models it is advised that the user rotates the beam map so that it matches the position angle of the user's data. The position angle of HIPE maps can be found in the primary FITS header and is specified by the POSANGLE keyword.

Table 5.2 summarises the basic beam parameters for data binned into $1''$ map pixels. The FWHM values are determined by fitting an asymmetric 2-D Gaussian to the beam maps, and the beam areas are computed by integrating explicitly under the measured beam profiles. It is recommended to use the as-measured beam area in $1''$ maps in the flux-density to surface brightness conversion.

The main beams are approximated by Gaussian profiles with the nominal FWHM values of (18.1, 24.9, 36.4)$''$, measured on maps with (6, 10, 14)$''$ pixels. The explicit integration under the measured beams in standard maps produces beam areas of (533, 936, 1808) arcsec^2, which are larger, by factors of approximately (1.18, 1.17, 1.08) at (250, 350, 500) μm, than those derived from higher resolution beam scans (maps with $1''$/pixel). These are derived by rebinning the updated (background-removed) beam maps to the standard SPIRE maps pixel sizes.

The basic beam parameters vary as a function of pixel scale, with the FWHM values and beam areas increasing with pixel size. This is expected since the fidelity of the surface brightness reconstruction becomes less reliable at low resolution, particularly with respect to the Airy ring pattern at higher radii from the source peak.

The values of the beam FWHM and solid angle given in Table 5.2 are correct for a source with the same spectral index as Neptune. See Table 5.4 for the effective beam area at a range of source spectral indices. With the diffuse and point source backgrounds removed from the beam maps, the uncertainty on the measured and effective beam solid angles is of the order of 1%.

Table 5.2: Basic 2-D Gaussian parameters for beams based on shadow measurements of Neptune. Uncertainties in the beam FWHM values and areas are estimated at $< 1\%$, and uncertainties in the beam solid angles at 1 %.

Band	PSW	PMW	PLW
$\alpha_{\rm Nep}$	1.29	1.42	1.47
Position angle (deg)	37.98	51.17	28.44
Pixel size (arcsec)	1	1	1
Major×Minor FWHM (arcsec)	18.4×17.4	24.9×23.6	37.0×33.8
Geometric mean FWHM ($\theta_{\rm Nep}$, arcsec)	17.9	24.2	35.4
Flattening (%)	5.1	5.4	8.7
Measured beam solid angle ($\Omega_{\rm Nep}$, arcsec^2)	454	803	1700
Isophotal frequency[a] ($\nu_{\rm eff}$, GHz)	1222.14	871.18	612.35
Pixel size (arcsec)	6	10	14
Major×Minor FWHM (arcsec)	18.9×18.0	25.8×24.6	38.3×35.2
Geometric mean FWHM ($\theta_{\rm Nep}$, arcsec)	18.4	25.2	36.7
Flattening (%)	4.8	5.0	8.1

([a]) The isophotal frequency is the frequency at which the solid angle of the monochromatic beam, weighted by the filter transmission and aperture efficiency, and integrated over all frequencies and sky area, is equal to the solid angle of the beam as measured on Neptune, using the model discussed in the text.

5.9.2 Frequency-dependent beam profiles and beam areas

The beam areas given in Table 5.2 are correct when observing a source with the same spectral index as Neptune. For all other sources the beam profile and area must be colour-corrected. This requires having a frquency-dependent model of the beam.

The beam maps in Figure 5.6 were used to produce azimuthally averaged radial beam profiles, as plotted in Figure 5.7. The radius of this beam profile scales inversely with frequency[4].

The RSRF-weighted beam profile measured on Neptune is assumed to be equal to the monochromatic beam profile at some effective isophotal frequency $\nu_{\rm eff}$ in the model. The radius of this function is then scaled with frequency as a power law with an index $\gamma = -0.85$[5]. The negative index results from the fact that with increasing frequency the beam profile effectively contracts in radial direction.

The monochromatic radial beam profile at a given frequency ν and radial distance θ is then given by

$$B_\nu(\theta, \nu) = B_{\rm Nep}(\theta \cdot (\nu/\nu_{\rm eff})^{-\gamma}), \tag{5.32}$$

where $B_{\rm Nep}$ is the beam profile as measured on Neptune.

The monochromatic beam area at a given frequency is simply the integral of the beam profile

$$\Omega_\nu(\nu) = \int_0^{\theta_{\rm max}} B_\nu(\theta, \nu) 2\pi\theta {\rm d}\theta. \tag{5.33}$$

where $\theta_{\rm max}$ is limited by the size of the beam map.

The modelled RSRF-weighted "effective" beam profile when observing a source with spectral index α_S is thus

$$B_{\rm eff}(\theta, \alpha_S) = \frac{\int\limits_{Passband} R(\nu)\eta(\nu)\nu^{\alpha_S} B(\theta, \nu){\rm d}\nu}{\int\limits_{Passband} R(\nu)\eta(\nu)\nu^{\alpha_S}{\rm d}\nu}, \tag{5.34}$$

and we can define the effective beam area for a given source spectrum, $\Omega_{\rm eff}$, by

$$\Omega_{\rm eff}(\alpha_S) = \frac{\int\limits_{Passband} R(\nu)\eta(\nu)\nu^{\alpha_S}\Omega_\nu(\nu){\rm d}\nu}{\int\limits_{Passband} R(\nu)\eta(\nu)\nu^{\alpha_S}{\rm d}\nu} \approxeq \int_0^{\theta_{\rm max}} B_{\rm eff}(\theta, \alpha_S)\, 2\pi\, \theta\, {\rm d}\theta, \tag{5.35}$$

where $\theta_{\rm max}$ is limited by the size of the beam map. Note that $\Omega_{\rm eff}(\alpha_S = -1) \equiv \Omega_{\rm pip}$, as given in Table 5.1.

The frequency dependence of the beam FWHM θ_ν and solid angle Ω_ν, as measured at a specific frequency, can then be approximated by power laws:

$$\theta_\nu(\nu) = \theta_{\rm Nep}\left(\frac{\nu}{\nu_{\rm eff}}\right)^{\gamma}, \text{ and} \tag{5.36}$$

$$\Omega_\nu(\nu) = \Omega_{\rm Nep}\left(\frac{\nu}{\nu_{\rm eff}}\right)^{2\gamma}, \tag{5.37}$$

[4] A prior version of the model described in Griffin et al. 2013, used an additional "constant" radial beam profile that did not change with frequency. The increased data accuracy achieved with the "shadow" observations showed that this part was due to residual background galaxies and thus removed.

[5] The value of γ is calculated from simulations of the SPIRE optics, and takes into account the change in diffraction from the focal plane array and the edge-taper at the edge of the primary mirror.

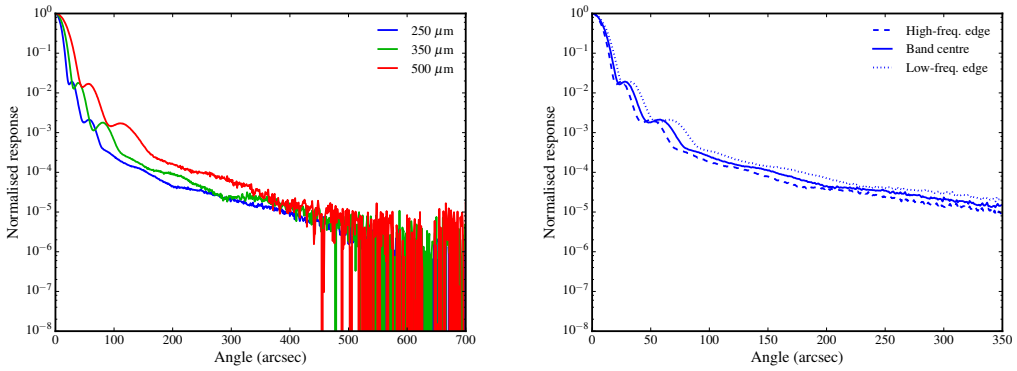

Figure 5.7: Left: Normalised radial beam profiles of the three SPIRE bands as measured on Neptune. Right: The PSW beam profile at the band centre (solid line) and the high-frequency (dashed line) and low-frequency (dotted line) band limits.

where $\nu_{\rm eff}$ is the isophotal frequency. The value of $\nu_{\rm eff}$ is fitted for each band such that the modelled beam solid angle for a source with Neptune's spectral index, $\alpha_{\rm Nep}$, is equal to the measured solid angle, $\Omega_{\rm Nep}$. The values for all these parameters in the three SPIRE bands are given in Table 5.2.

It is these values of **monochromatic** beam solid angle (Eq. 5.37) that are required when calculating the values of $K_{\rm MonE}$ and $K_{\rm ColE}$ (see Eqs. 5.16, 5.23 and 5.26). Note that the monochromatic beam FWHM and solid angle are defined as a power law relative to the isophotal frequency $\nu_{\rm eff}$, and use the fact that $B_\nu(\theta, \nu_{\rm eff}) \equiv B_{\rm Nep}(\theta)$. If they are scaled with (ν/ν_0) then the nomalisation factors must also be changed to $\theta_\nu(\nu_0)$ and $\Omega_\nu(\nu_0)$, such that

$$\theta_\nu(\nu) = \theta_\nu(\nu_0)\left(\frac{\nu}{\nu_0}\right)^\gamma, \text{ and} \tag{5.38}$$

$$\Omega_\nu(\nu) = \Omega_\nu(\nu_0)\left(\frac{\nu}{\nu_0}\right)^{2\gamma}, \tag{5.39}$$

where the values of $\Omega_\nu(\nu_0) = \Omega_{\rm eff}(\alpha_S = -1) \equiv \Omega_{\rm pip}(\nu_0)$, as given in Table 5.1.

The **effective** beam solid angles for sources with a range of spectral or grey body indices, using Eq. (5.32)–(5.35), are given in Table 5.4 and 5.5 respectively, and plotted in Figure 5.8. Since much of the pipeline analysis is performed assuming a source with $\alpha_S = -1$, a beam correction parameter, $K_{\rm Beam}(\alpha_S)$ is also provided, such that:

$$\Omega_{\rm eff}(\alpha_S) = \frac{\Omega_{\rm eff}(-1)}{K_{\rm Beam}(\alpha_S)}. \tag{5.40}$$

If used in conjunction with colour correction, the same spectral index for both the colour correction and the beam solid angle must be used.

5.9.3 Optical model of photometer beams

The theoretical model of the beams is based on an optical model of the telescope and the instrument, which has been shown by analysis of in-flight data to provide a highly representative characterisation

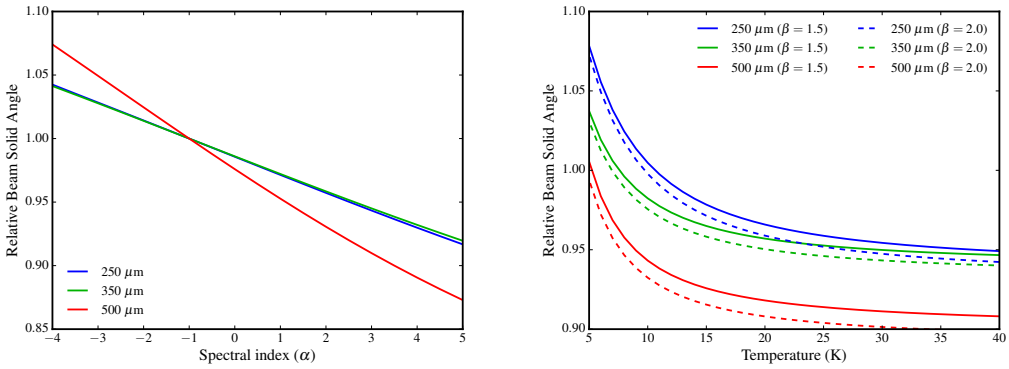

Figure 5.8: The variation of effective beam area relative to the beam area used in the pipeline ($\alpha_{\rm pip} = -1$). The areas are plotted against source spectral index (left) and against grey body temperature for two values of the grey body index β (right). See Table 5.4 and 5.5.

of the low-level structure in the beams. The model is based on computations of the response function of the end-to-end optical train of the *Herschel* observatory and SPIRE photometer at individual in-band wavelengths, then summing the monochromatic response with specific weights. The model contains the reconstructed wave-front error distribution of the telescope taken from ground measurements, taking into account the dominant impact of the flight environmental conditions (gravity release, cryo-vacuum operation), as well as the detailed pupil obscuration from the full observatory geometry. The full SPIRE instrument optical model including the entire photometer train up to focal plane is also implemented (see Figure 5.9). The simulated source is a coherent point source with continuum Rayleigh-Jeans (RJ) spectrum, representative of most bright point sources with brightness temperature. The effect of the detector feedhorn is taken into account by including further pupil apodisation with a spectrally-varying edge taper (and associated spectral shift of the diffraction focus) within each band, which has been characterised during SPIRE ground calibration.

The full band response is obtained by spectral weighting of the set of individual responses. The weights are obtained by product of the Rayleigh-Jeans source spectrum with the instrument RSRF in each band, the spectral in-band throughput $A\Omega$ and finally the spectral in-band coupling, all derived from flight model instrument level ground calibration.

The derived beam models can be considered as "static" noise-free point source reference maps, complementary to the empirical maps which, being flight measured and pipeline generated, include the additional effects among others of electronics detection, scanning, processing and map reconstruction and general additional background noise from sky and observatory.

Figure 5.10 shows the theoretical beam models, all given at a $0.6''$ sampling over a $6' \times 6'$ angular extent and in the spacecraft coordinate system (Y/Z; rotation via the user's defined position angle will transfer into the relevant sky coordinate systems).

The model beam product provides significantly higher detail at greater radius but presently is released only at $6' \times 6'$ scale. Larger scale beam models (e.g., up to 1 deg scale) at lower sampling (e.g. standard 6, 10, $14''$) have been generated in order to provide better estimates on integrated beam extent/effective surface area and may be released later.

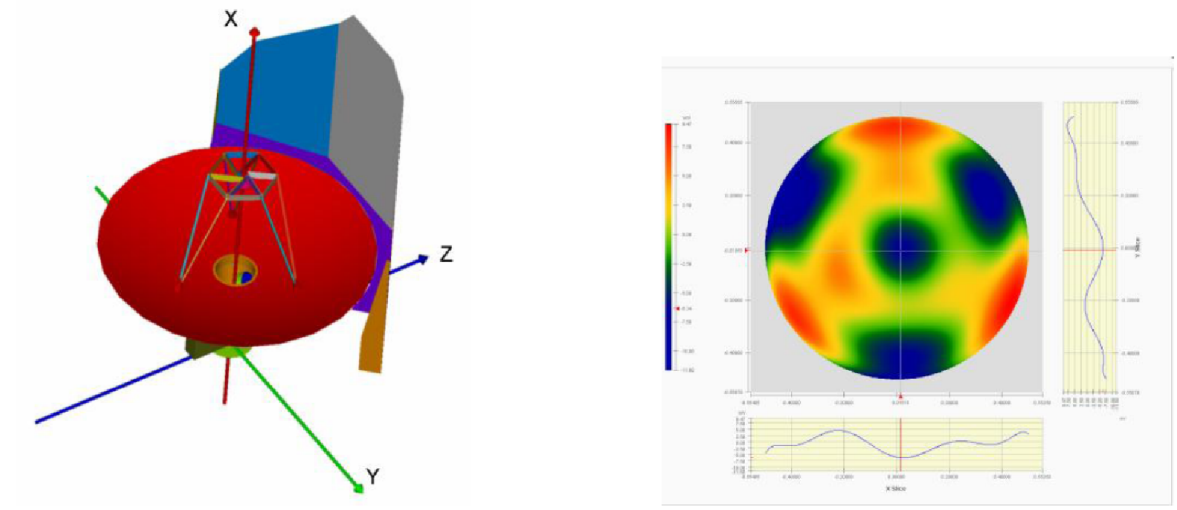

Figure 5.9: View of the model geometry (left) and reconstructed telescope pupil optical path difference map from environmental ground measurements by *Herschel* Observatory industrial contractors (right).

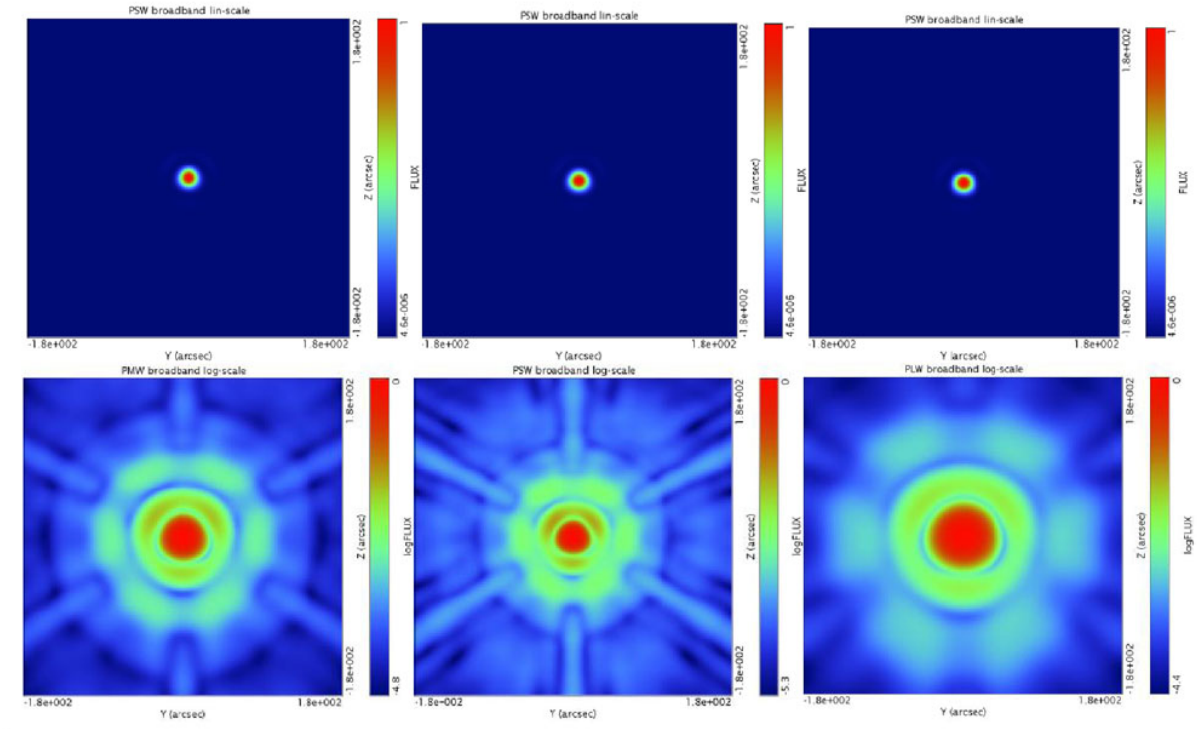

Figure 5.10: Theoretical photometer beams for 250, 350, and 500 μm (left, centre, and right, respectively), with linear scaling (top row) and logarithmic scaling (bottom row).

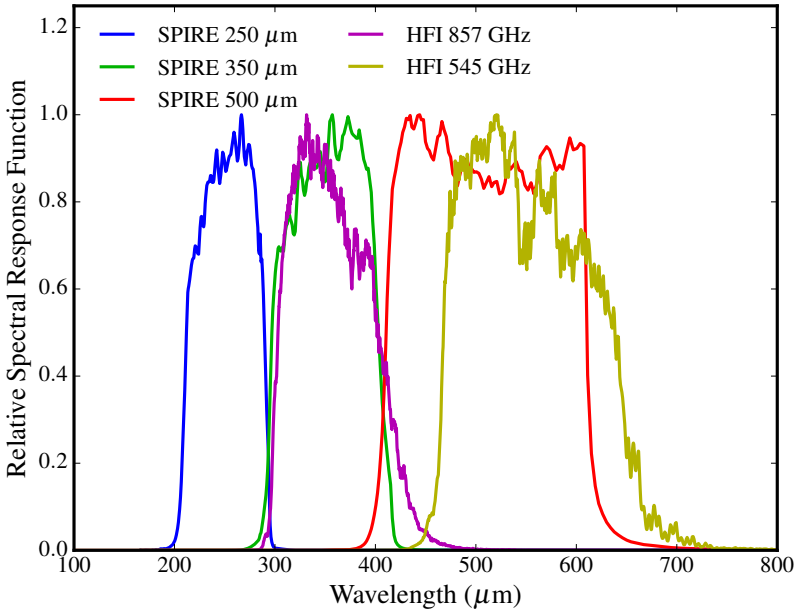

Figure 5.11: Relative Spectral Response Functions, $R(\nu)$, for the five wavebands: *Planck*HFI 545 GHz & 857 GHz, and *Herschel*SPIRE 250 μm, 350 μm & 500 μm bands.

5.10 Absolute flux offset estimation of SPIRE maps via cross-calibration with *Planck*-HFI

The power incident on the SPIRE bolometers is dominated by thermal emission from the telescope, and therefore the recorded signal levels do provide a measure of the absolute sky brightness.

The *Planck*-HFI detectors are similar to the SPIRE ones. However, its observing strategy allows it to (almost) observe a great circle on the sky every minute (having a 1 rpm spinning rate). By comparing the sky brightness as measured by COBE-FIRAS at the galactic poles (where the dust emission is lower), HFI is capable of defining an absolute brightness level for its maps (Planck Collaboration VIII, 2014).

Planck maps are in units of MJy/sr and in order to recalibrate the SPIRE maps to the absolute calibration coming from *Planck*, the first step needed is to take the extended source calibrated maps from SPIRE. These are available as Level-2 products ("extdPxW" maps) and are produced as explained in detail in Section 5.5, in particular, taking into account the frequency dependence of the beam solid angle $\Omega_\nu(\nu)$.

SPIRE and HFI share two channels with overlapping passbands as shown in Figure 5.11. SPIRE-PMW and HFI-857 have a similar filter profile, while SPIRE-PLW and HFI-545 are visibly offset. The filter profiles are not identical, so a colour-correction from HFI to SPIRE passband is needed. In addition, both SPIRE and the HFI maps assume a fully extended source with intensity $I_S(\nu) \sim \nu^{-1}$, but the actual spectrum of the sky is closer to that of a modified blackbody with a particular dust emissivity index β, i.e. $I_S(\nu) \sim \nu^\beta \mathcal{B}(T,\nu)$, with the Planck blackbody function $\mathcal{B}(T,\nu)$ given in Eq. (5.24). Hence, the proper colour correction calculation should incorporate the more realistic

source spectrum as well as the differences in the RSRFs.

The SPIRE colour correction $K_{\rm ColE}$ in the case of a modified blackbody with different values of T and β is explained in Section 5.7 and tabulated in Table 5.7. For the HFI, we can follow Eq. (5.26) and derive the factor K_i to convert from the HFI pipeline spectrum to a greybody, taking $\alpha_{\rm pip} = -1$:

$$K_i = \nu_0^{\beta+1} \mathcal{B}(T,\nu_0) \times \left[\frac{\int_{Passband} \nu^{-1}\, R(\nu)\, {\rm d}\nu}{\int_{Passband} \nu^{\beta} \mathcal{B}(T,\nu)\, R(\nu)\, {\rm d}\nu} \right], \tag{5.41}$$

where the index i is for the particular *Planck*-HFI band with ν_0 = 545 GHz or ν_0 = 857 GHz and $R(\nu)$ is the corresponding HFI filter RSRF.

Having K_i for HFI and $K_{\rm ColE}$ for SPIRE, we can then derive the overall conversion factors from HFI to SPIRE, assuming a modified blackbody source spectrum $I_S \sim \nu^{\beta}\, \mathcal{B}(T,\nu)$:

$$\begin{aligned}
K_{857\rightarrow {\rm PMW}}(T,\beta) &= \frac{K_{857}\, I_S(\nu_{857})}{K^{\rm PMW}_{\rm ColE}\, I_S(\nu_{\rm PMW})} = \frac{K_{857}\, \nu_{857}^{\beta}\, \mathcal{B}(T,\nu_{857})}{K^{\rm PMW}_{\rm ColE}\, \nu_{\rm PMW}^{\beta}\, \mathcal{B}(T,\nu_{\rm PMW})}, \\
K_{545\rightarrow {\rm PLW}}(T,\beta) &= \frac{K_{545}\, I_S(\nu_{545})}{K^{\rm PLW}_{\rm ColE}\, I_S(\nu_{\rm PLW})} = \frac{K_{545}\, \nu_{545}^{\beta}\, \mathcal{B}(T,\nu_{545})}{K^{\rm PLW}_{\rm ColE}\, \nu_{\rm PLW}^{\beta}\, \mathcal{B}(T,\nu_{\rm PLW})}, \\
K_{857\rightarrow {\rm PSW}}(T,\beta) &= \frac{K_{857}\, I_S(\nu_{857})}{K^{\rm PSW}_{\rm ColE}\, I_S(\nu_{\rm PSW})} = \frac{K_{857}\, \nu_{857}^{\beta}\, \mathcal{B}(T,\nu_{857})}{K^{\rm PSW}_{\rm ColE}\, \nu_{\rm PSW}^{\beta}\, \mathcal{B}(T,\nu_{\rm PSW})},
\end{aligned} \tag{5.42}$$

with $\nu_{545} = 545$ GHz and $\nu_{857} = 857$ GHz for the HFI and $\nu_{\rm PMW} = 865.55$ GHz, $\nu_{\rm PLW} = 599.58$ GHz and $\nu_{\rm PSW} = 1199.17$ GHz for the three SPIRE bands. Note that the conversion $K_{857\rightarrow {\rm PSW}}$ is only given for completeness as the PSW band only marginally overlaps with the HFI 857 GHz band.

It is evident that the colour correction, and consequently the cross-calibration, depends on the assumed greybody spectrum. The colour correction factors computed with a fixed $\beta = 1.8$ and different temperatures are shown in the upper panel of Figure 5.12.

Using the two *Planck*-HFI maps at 545 and 857 GHz we can derive the ratio $R_{\rm HFI}(T,\beta)$ of the HFI intensities for a range of temperatures to eliminate this dependence from the colour correction factors:

$$R_{\rm HFI}(T) = \left(\frac{\nu_{545}}{\nu_{857}}\right)^{1.8} \times \frac{\mathcal{B}(\nu_{545},T,\beta=1.8)}{\mathcal{B}(\nu_{857},T,\beta=1.8)}. \tag{5.43}$$

Figure 5.12, bottom panel, shows the same colour correction factors as functions of the ratio $R_{\rm HFI}$. From the ratio of the two HFI maps, converted using Eq. (5.41), we can obtain the average $R_{\rm HFI}$ and then the $K_{\rm HFI\rightarrow SPIRE}$ factors.

The SPIRE calibration context, SPIRE_CAL_12 or above, contains the precomputed $R_{\rm HFI}$ and $K_{\rm HFI\rightarrow SPIRE}$ for a range of temperatures T from 5 K to 300 K and $\beta = 1.8$. These are available in a table called Phot/ColorCorrHfi. The method for calibration SPIRE maps in practice, so that they have the absolute offset from *Planck*, is explained in detail in the SPIRE Data Reduction Guide, section 4.1. The final Level-2 SPIRE maps "extdPxW" (in units of MJy/sr) in the *Herschel* Science Archive are already recalibrated to the *Planck* absolute offset, following the assumptions described in this section.

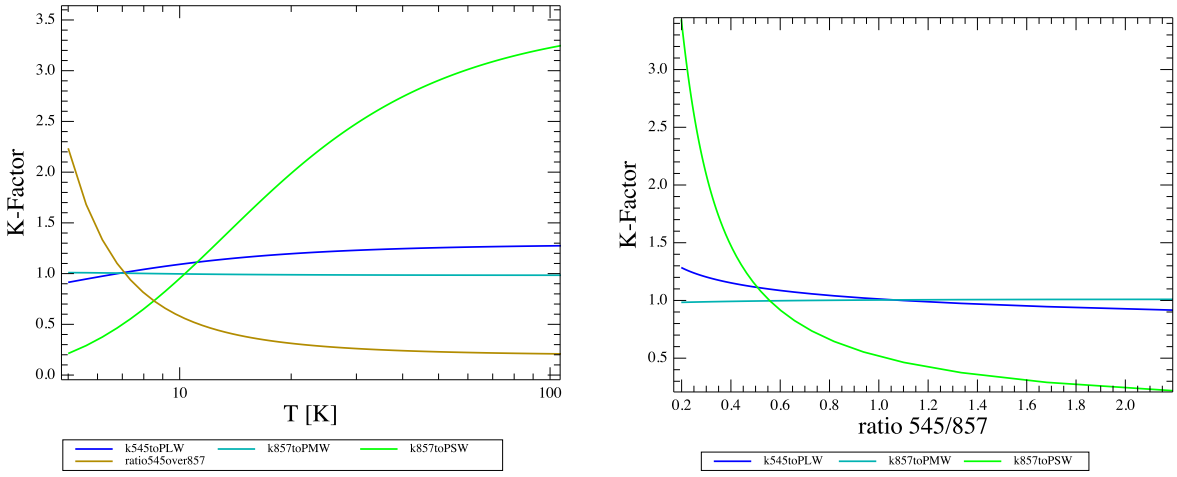

Figure 5.12: Left: the three colour correction factors $K_{\mathrm{HFI}\rightarrow\mathrm{SPIRE}}$ and the ratio R_{HFI} as a function of dust temperature, assuming a fixed dust emissivity index $\beta = 1.8$. Right: the three colour correction factor $K_{\mathrm{HFI}\rightarrow\mathrm{SPIRE}}$ as a function of the ratio R_{HFI}, for $\beta = 1.8$.

5.11 *HiRes* SPIRE maps

With good knowledge of the *Herschel*-SPIRE beam profile, it is possible to deconvolve the data in cases of high signal-to-noise data. There are several techniques available, with *HiRes* being included as a built-in task in HIPE (from v12 onwards). The procedure is based on the Richardson-Lucy deconvolution algorithm (Richardson, 1972; Lucy, 1974), and has been successfully applied to IRAS (Aumann et al., 1990) and WISE (Jarrett et al., 2012) data. The source code is available on GitHub[6], and information is available on the NHSC public wiki[7].

For SPIRE observations, *HiRes* typically increases the resolution of the image by a factor of 2, as described in Xu et al. (2014). It is only beneficial when there is structure in the map on spatial scales smaller than the beam, and for which the signal-to-noise is sufficiently high. The selection criteria for observations to which *HiRes* has been applied are discussed in Section 5.11.2.

5.11.1 *HiRes* Procedure

The *HiRes* processing applied to SPIRE maps uses the following parameters and assumptions.

- **Detector relative gains**: *HiRes* is best suited to compact or partially-extended emission, and therefore the detector relative gains are applied to the dectector timelines before destriping
- **SPIRE beam**: The *HiRes* images in the archive use the SPIRE beam as measured on Neptune (see Section 5.9) with 1 arcsecond resolution. The same beam is assumed for all detectors and all observations, regardless of orientation. While the SPIRE beam is not completely azimuthally-symmetric, the variations caused by a beam rotation, are very small. Previous implementations have used different beam profiles for each detector, but the variation across the

[6] github.com/stargaser/hires
[7] nhscsci.ipac.caltech.edu/sc/index.php/Spire/HiRes

Table 5.3: Criteria used for selecting SPIRE observations for *HiRes* processing

	PSW	PMW	PLW
Criterion 1			
Surface brightness threshold (MJy/sr)	100	30	20
Number of pixels above threshold	544	196	100
Equivalent sky area (sq. arcmin)	5.44	5.44	5.44
Criterion 2			
99th percentile threshold (MJy/sr)	30	15	10

detector arrays is very minor. In addition, the knowledge of the beam profile for individual detectors is much poorer than for the entire array.

- **Output WCS**: Since *HiRes* roughly doubles the image resolution, the resulting FITS files have identical World Coordinate System (WCS) to the nominal FITS files, but with half the pixel size (i.e. 3, 5, 7 arcsec at 250, 350, 500 μm).

- **Flux offset**: For the deconvolution to work well, the data should include as few negative values as possible. The timeline data therefore has the absolute offsets described in Section 5.10 applied, converted from surface brightness (MJy/sr) to flux density (Jy/beam) by dividing by the beam solid angle. Once *HiRes* has been run, the offset is removed and the conversion from flux density (Jy/beam) to surface brightness (MJy/sr) is applied as for nominal maps.

- **Iterations**: *HiRes* is an iterative procedure, but excessive iterations can over-process the data. A good compromise is to run *HiRes*for 20 iterations.

- **NaN-detection**: The Fourier deconvolution can over-emphasise pixels which have not been de-glitched (such as at the edge of a map). For this reason, any pixels in resulting *HiRes* maps with flux density greater than 5 times the maximum value in the nominal map are set to NaN value.

Figures 5.13–5.14 show the effect of *HiRes* on a specific observation.

5.11.2 Observation selection

There is a good correlation between the flux density and the signal-to-noise in a SPIRE map. For *HiRes* processing, the primary consideration is the signal relative to the extragalactic background. The selection is made based on the nominal maps in surface brightness units, and which have had the absolute zero point offset applied.

The maps that have been selected to undergo *HiRes* processing have had two criteria applied:

- **Criterion 1:** A sufficient number of pixels (i.e. an area of sky) must be above a threshold surface brightness

- **Criterion 2:** The 99th percentile of the surface brightness must be above a threshold value

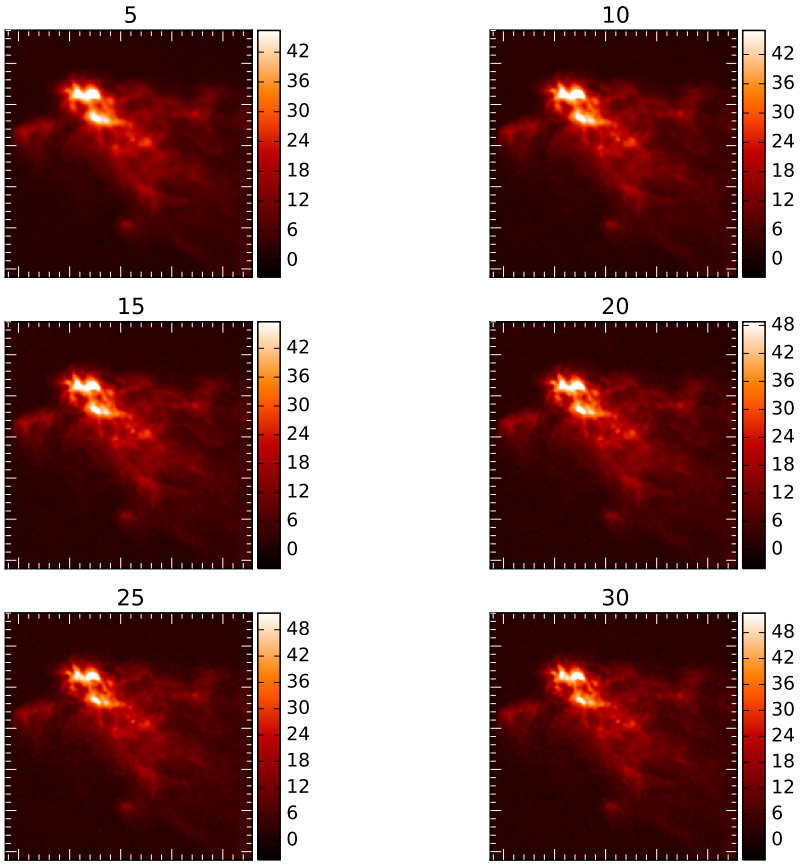

Figure 5.13: Maps of obsid 1342249237 produced by *HiRes* after a range of iterations. See Figure 5.14 for a zoom on the region in the top-left.

This selection criteria were met by around 25% of the SPIRE observations, though a small number have been manually added to or removed from the list after visual inspection. Most of these are galactic observations, though there are some that contain large, bright nearby galaxies. See Figs 5.15–5.16 plots showing the observations SPIRE archive compared with these criteria.

If an observation met the criteria for only one or two SPIRE bands it was processed for all three. The number of pixels over the surface brightness threshold is recorded in the metadata of the FITS file, using keyword ”HRSQUAL”, to give an indication of the quality of the map.

Where an observation is paired with one or more others (e.g. in SPIRE/PACS Parallel mode), *HiRes* was applied to all observations together, after the aggregation and destriping of the detector timelines from each individual observation. In the archive, this appears as a Level 2.5 product, whereas single (un-paired) observations appear as Level 2. The maps are labelled as hiresPSW, hiresPMW, hiresPLW for the PSW (250μm), PMW (350μm) and PLW (500μm).

5.12 Recipes for SPIRE photometry

This section provides practical guidelines on how to follow the framework in Chapter 5 and apply

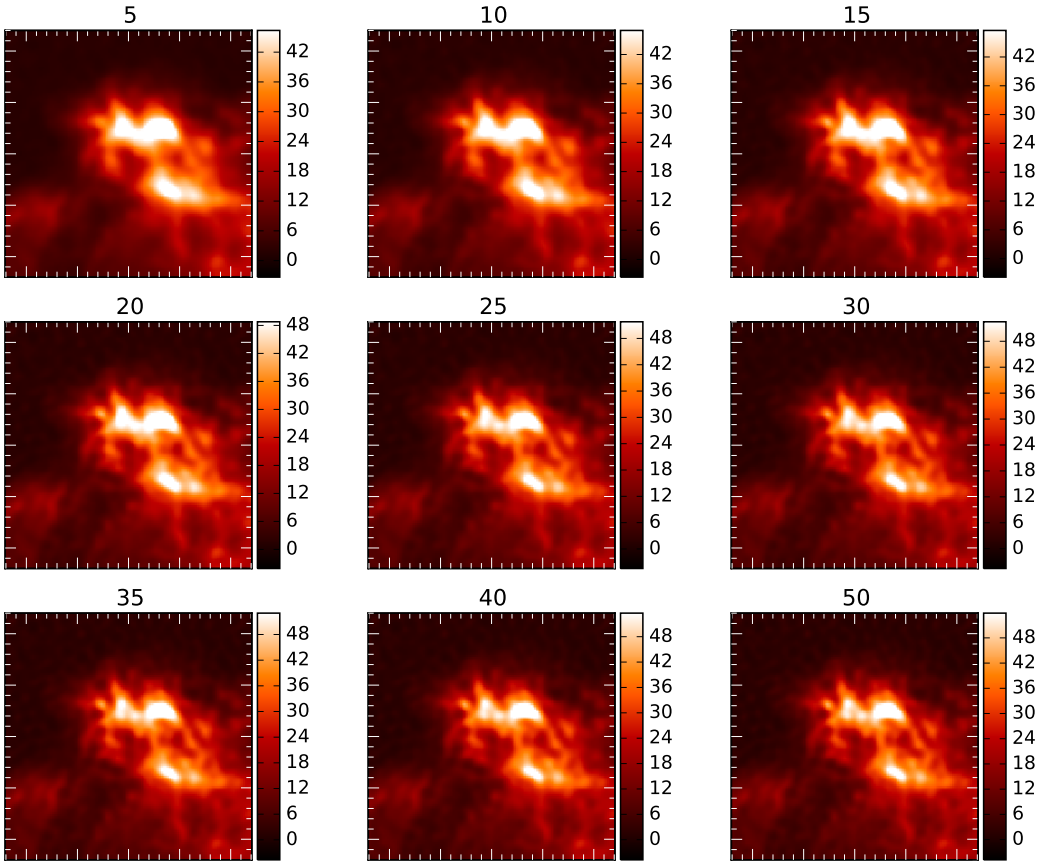

Figure 5.14: Maps of a small region of obsid 1342249237, showing the small-scale improvement after a number of iterations. The noise becomes increasingly visible with the number of iterations.

the appropriate corrections to the extracted flux densities. Much more detailed recipes are provided in the SPIRE Data Reduction Guide, available from the *Herschel* Interactive Processing Environment (HIPE).

Note that we do not discuss how the actual source detection was performed; a detailed overview of the available methods in HIPE are presented in Pearson et al. (2014), as well as in the SPIRE Data Reduction Guide.

5.12.1 Application of colour correction parameters

The flowchart in Figure 5.17 outlines the basic steps that should be followed using the standard pipeline products. The steps are presented in greater detail in the SPIRE Data Reduction Guide. The four main procedures are:

Point source fitting from timelines:

1. Use Level 1 timeline products, which give flux densities (in Jy/beam) of for point sources with a $\nu S_\nu = \text{const}$ spectrum.

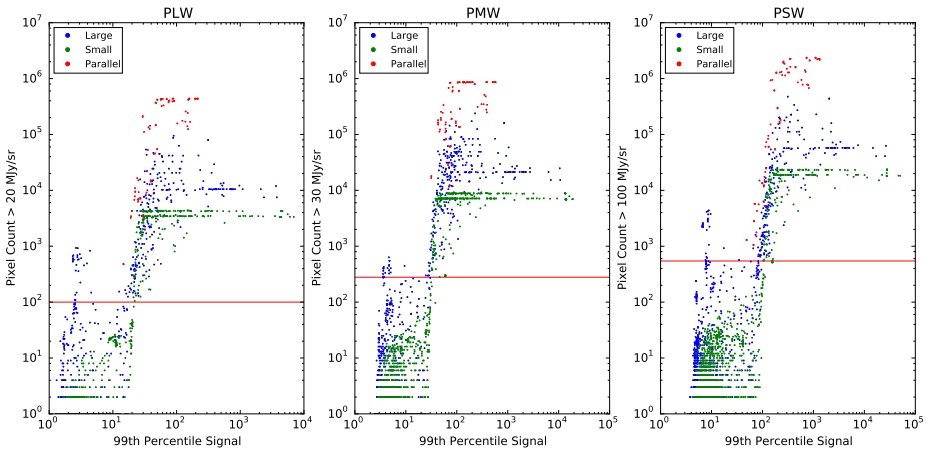

Figure 5.15: The observations SPIRE archive measured against the two criteria. The threshold for Criterion 1 in each band is highlighted as a red horizontal line.

.

2. Use timeline source fitting algorithms and obtain the source flux density.

3. Colour-correct the flux density for the true source spectrum using the point source colour correction parameters in Table 5.6 (or Table 5.7 for a grey body).

4. The source flux density is then provided in the units specified in the source fitting routine (usually Jy or mJy).

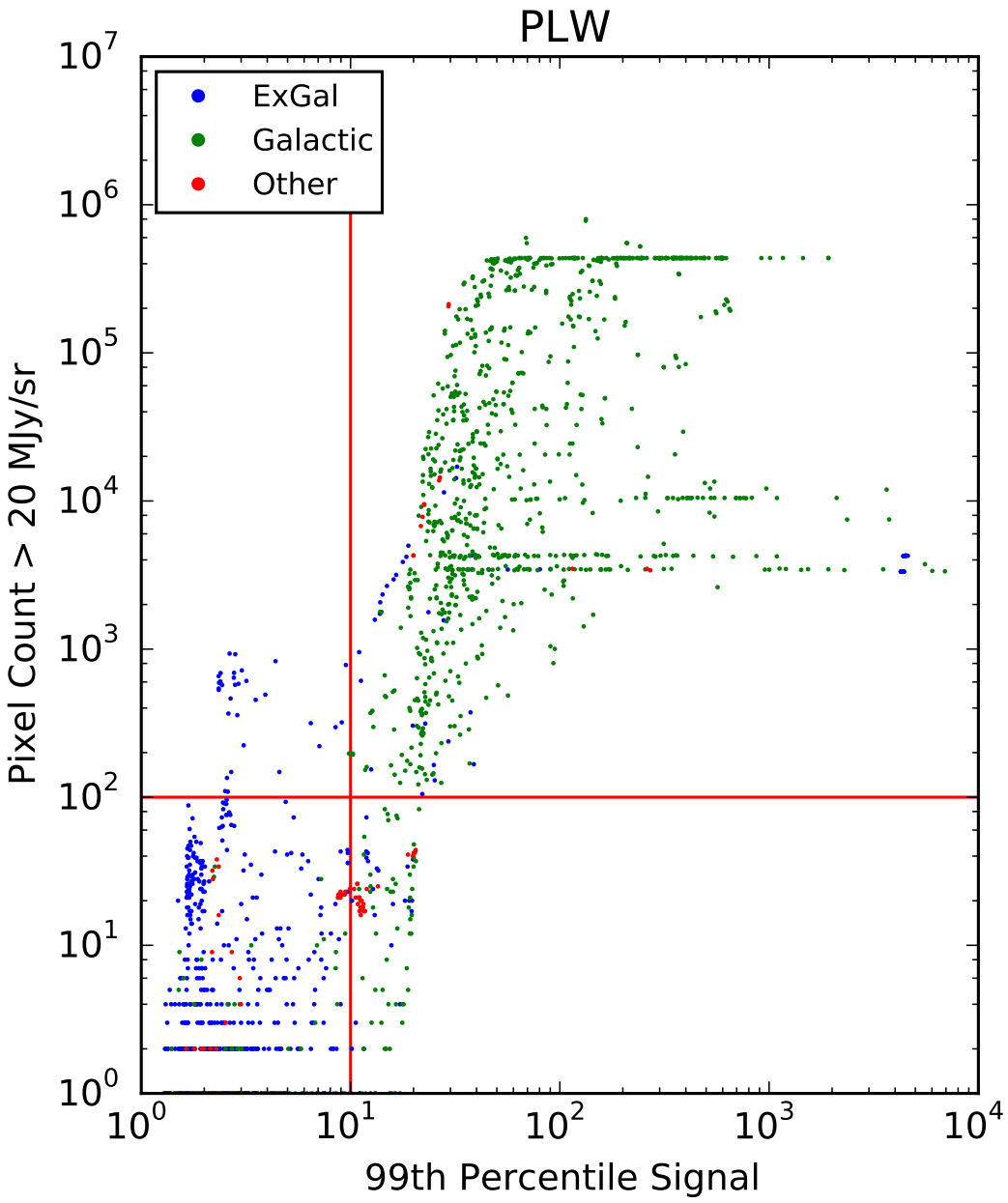

Figure 5.16: The observations SPIRE archive measured against the two criteria for PLW band, with thresholds shown for both criteria.

.

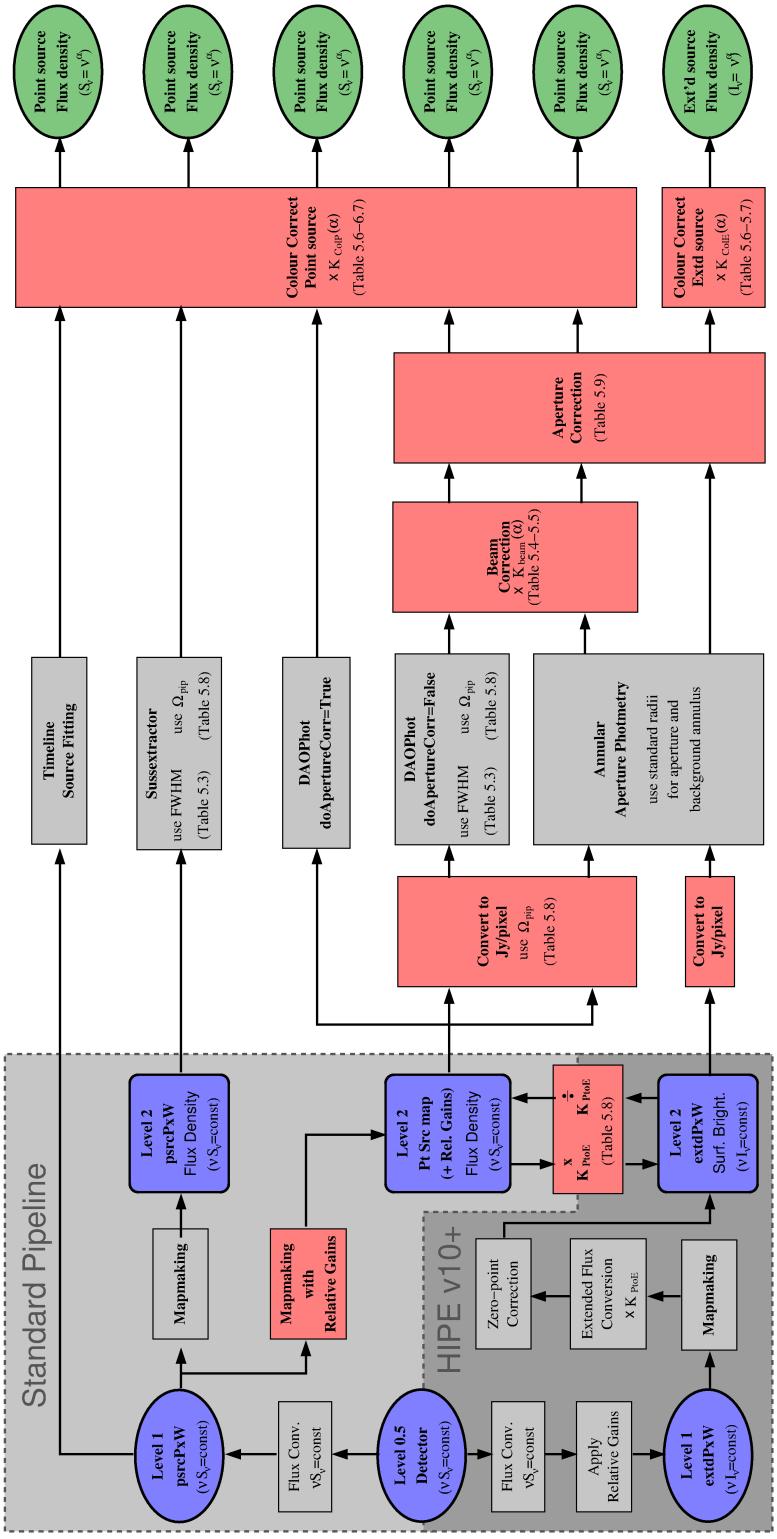

Figure 5.17: Flowchart showing the steps involved in using the standard photometer pipeline products. The standard pipelines are shown in grey; the pipeline products are in blue; the user products are in green. Steps the use should perform are shown in red.

Point source photometry from maps:

1. Use Level 2 point source map products (called "psrcPxW" in HIPE v10 and above), which give flux densities (in Jy/beam) for point sources with a $\nu S_\nu = \mathrm{const}$ spectrum.
2. Use your chosen map-based source extraction/fitting procedure. The beam FWHM should be θ_{Nep} as given in Table 5.2. The beam solid angle (if required) should be the pipeline beam solid angle Ω_{pip} as given in Table 5.1.
3. Colour-correct for the true source spectrum using the point source colour correction parameters in Table 5.6 (or Table 5.7 for a grey body).
4. The source flux density is then provided in the units specified in the source fitting routine (usually Jy or mJy).

Aperture photometry of point sources (starting from point source maps):

1. Use the Level 2 map products, which give flux densities (in Jy/beam) for point sources with a $\nu S_\nu = \mathrm{const}$ spectrum. **NB: To increase the accuracy, the observations should be reprocessed with relative gains applied between Level 1 (timeline fluxes) and Level 2 (map fluxes).**
2. Convert the map to surface brightness using the pipeline beam solid angle (Ω_{pip}) as given in Table 5.1. (Note that most HIPE aperture photometry tasks require a maps in units of Jy/pixel.)
3. Perform the aperture photometry.
4. Apply the beam correction factor as given in Table 5.4 (or Table 5.5 for a greybody).
5. Colour-correct for the true source spectrum using the point source colour correction parameters (K_{ColP}) in Table 5.6 (or Table 5.7 for a grey body).
6. If the recommended apertures are used, then the aperture corrections listed in Table 5.8 should be applied. If a different aperture and/or background annulus is used, then in the SPIRE Calibration Tree, the table Phot/RadialCorrBeam provides the normalised beam area (also known as the Encircled Energy Fraction) for the full range of apertures from $0''$ to $700''$. Note that this normalised beam area is for a source with $\alpha_{\mathrm{pip}} = -1$. For any other non-standard apertures, the aperture corrections could be computed from the beam maps, available on the SPIRE Public wiki.
7. The source flux density is then given in the units specified by the aperture photometry routine (usually Jy or mJy).

Aperture photometry of point sources (starting from extended maps):

This method uses the extended source maps, available for products processed with HIPE v10 and above. These have the relative gains applied (which improve the reliability of the measurements), and so do not require reprocessing, but are calibrated for an infinitely extended source. Relative to the point source calibration, the extended one produces slightly lower fluxes (by 0.5-1%), which is within the uncertainty from the the beam solid angle ($\sim 1\%$).

1. Use the Level 2 extended source map products (called "extdPxW"), which give surface brightness (in MJy/sr) for infinitely extended sources with a $\nu S_\nu = \mathrm{const}$ spectrum.

2. If desired, recalibrate the map for a point source in units of flux density (recommended):

   (a) Convert back to point source calibration by **dividing** by the K_{PtoE} parameter given in Table 5.1. This produces maps in Jy/beam. Ensure that the units of the map are set accordingly.

   (b) Divide the maps by the pipeline beam solid angle (Ω_{pip}) given in Table 5.1, to convert the map units to surface brightness. Note that most aperture photometry tasks require a map in units of Jy/pixel.

3. Perform the aperture photometry.

4. Apply the beam correction factor as given in Table 5.4 (or Table 5.5 for a greybody).

5. Colour-correct for the true source spectrum using the **point source** colour correction parameters (K_{ColP}) in Table 5.6 (or Table 5.7 for a grey body).

6. If the recommended apertures are used, then the aperture corrections listed in Table 5.8 should be applied. If a different aperture and/or background annulus is used, then in the SPIRE Calibration Tree, the table Phot/RadialCorrBeam provides the normalised beam area (also known as the Encircled Energy Fraction) for the full range of apertures from 0″ to 700″. Note that this normalised beam area is for a source with $\alpha_{\mathrm{pip}} = -1$. For any other non-standard apertures, the aperture corrections could be computed from the beam maps, available on the SPIRE Public wiki.

7. The source flux density is then given in the units specified by the aperture photometry routine (usually Jy or mJy).

Extended source photometry (starting from point source maps):

1. Use Level 2 point source map products(called "psrcPxW"), which give flux densities (in Jy/beam) for point sources with a $\nu S_\nu = \mathrm{const}$ spectrum.

2. Multiply by the K_{PtoE} conversion parameter to convert maps to surface brightness (in MJy/sr) for an infinitely extended source with a $\nu S_\nu = \mathrm{const}$ spectrum, as given in Table 5.1.

3. Perform the required photometry.

4. If the recommended apertures are used, then the aperture corrections listed in Table 5.8 should be applied. If a different aperture and/or background annulus is used, then in the SPIRE Calibration Tree, the table Phot/RadialCorrBeam provides the normalised beam area (also known as the Encircled Energy Fraction) for the full range of apertures from 0″ to 700″. Note that this normalised beam area is for a source with $\alpha_{\mathrm{pip}} = -1$. For any other non-standard apertures, the aperture corrections could be computed from the beam maps, available on the SPIRE Public wiki.

5. Colour-correct for the true source spectrum using the extended source colour correction parameter (K_{ColE}) in Table 5.6 (or Table 5.7 for a grey body).

6. The source surface brightness is then given the units specified in the photmetry routine (usually MJy/sr).

Extended source photometry (starting from extended source maps):

1. Use Level 2 extended source map products (called "extdPxW"), which give surface brightnesses (in MJy/sr) for infinitely extended sources with a $\nu S_\nu = \mathrm{const}$ spectrum.
2. Perform the required photometry.
3. If the recommended apertures are used, then the aperture corrections listed in Table 5.8 should be applied. If a different aperture and/or background annulus is used, then in the SPIRE Calibration Tree, the table Phot/RadialCorrBeam provides the normalised beam area (also known as the Encircled Energy Fraction) for the full range of apertures from $0''$ to $700''$. Note that this normalised beam area is for a source with $\alpha_{\mathrm{pip}} = -1$. For any other non-standard apertures, the aperture corrections could be computed from the beam maps, available on the SPIRE Public wiki.
4. Colour-correct for the true source spectrum using the extended source colour correction parameter (K_{ColE}) in Table 5.6 (or Table 5.7 for a grey body).
5. The source surface brightness is then given the units specified in the photmetry routine (usually MJy/sr).

It is important to note that, since the SPIRE photometer flux calibration is performed on the timeline data, the beam areas equivalent to the beams of the timeline data must be used when calibrating extended emission in terms of surface brightness (Jy/pixel or /sr). This means that the beam areas corresponding to the $1''$ pixel scale in Table 5.2 should be used when converting from Jy/beam to Jy/pixel.

For the purposes of point source extraction, beam fitting etc., where the absolute scale of the beam model is unimportant, the appropriate FWHM for a map with a given pixel scale should be used.

5.12.2 Pixelisation correction

The SPIRE flux calibration is time-line based (Jy/beam). As a result, the signal level in a map pixel depends on how the square map pixel size compares to the size of the beam. Only in the limit of infinitely small map pixels would a pixel co-aligned with a point source register the true source flux density. It is important to note that no pixel size correction factors are incorporated in the SPIRE Level 2 map-making. **For a given map pixel, the flux density value represents the average in-beam flux density measured by the detectors while pointed within that area**. Taking the pixel value for the flux density of an isolated co-aligned point source in an otherwise blank map would thus yield an underestimate of the true flux density.

The necessary correction factor is a function of the map pixel size and the beam size, and is a simple multiplicative factor. For a symmetrical Gaussian beam of FWHM θ_{Beam}, a square pixel of side θ_{Pix}, and a co-aligned source, the correction factor is:

$$P = \frac{\pi}{4\ln(2)} \left(\frac{\theta_{\mathrm{Beam}}}{\theta_{\mathrm{Pix}}}\right)^2 \mathrm{erf}^2 \left[\left(\frac{\theta_{\mathrm{Pix}}}{\theta_{\mathrm{Beam}}}\right) [\ln(2)]^{1/2}\right], \tag{5.44}$$

where erf is the error function $\mathrm{erf(x)} = \frac{2}{\pi}\int_0^x e^{-t^2}\,\mathrm{d}t$.

However, in the general case the source will be randomly aligned with respect to the map pixel resulting in a slightly different correction, and a small random uncertainty corresponding to the actual offset of the source with respect to the pixel centre for a particular observation. Moreover, the source is not completely covered on infinitesimal scales, because the source signal is only sampled at a finite set of detector locations.

Tests of how the measured flux densities of point sources in map data depend on the pixel size have been performed using standard large and small scan map observations of Neptune (for 500 μm only) and γ Dra (for all three bands). Maps from these data were generated at various pixel scales, the data were fitted with Gaussian functions, and then the resulting median flux densities (in the case of the γ Dra data) or median measured/model flux density ratios (in the case of Neptune) were examined to understand how the measured flux densities vary as a function of pixel size.

For 250 μm data, these tests demonstrated that Eq. (5.44) provides an accurate correction for point source flux densities measured by PSF fitting in maps in all situations. For 350 μm data, these tests demonstrated that Eq. (5.44) provides an accurate correction for point source flux densities measured by PSF fitting in maps for only sources at the centres of small scan maps. The results from the 350 μm large scan map data indicate that the measured flux densities may be lower (by a few percent) than what is implied by Eq. (5.44) if the source is not centered within scan legs, although the exact decrease in flux density depends on the location of the source relative to the scan legs. For 500 μm, we found that Eq. (5.44) did not provide an accurate correction. Instead, the following empirical equation should be used:

$$P = 1 - 0.0018\,\theta_{\mathrm{Pix}} - 0.00037\,\theta_{\mathrm{Pix}}^2, \tag{5.45}$$

where θ_{Pix} is the pixel size in arcsec.

Performing the pixelisation correction introduces an additional uncertainty which it is best to determine empirically. At this time, this has only been characterised for 500 μm maps. The fractional uncertainty due to the pixelisation correction is given by

$$U_P = 0.0023 - 0.00113\,\theta_{\mathrm{Pix}}. \tag{5.46}$$

The default HIPE pixel sizes for (250, 350, 500) μm are $\theta_{\mathrm{Pix}} = (6, 10, 14)$ arcsec. The corresponding pixel size correction factors, given by Eqs. (5.44) and (5.45), are $P = (0.951, 0.931, 0.902)$. From Eq. (5.46), the corresponding percentage uncertainties introduced into the point source flux density estimation at 500 μm is 1.5%. This uncertainty should be added in quadrature to the other statistical uncertainties of the measurement. Note that similar uncertainties may be appropriate to apply to 250- and 350-μm data but have not yet been derived.

The pixelisation corrections presented here have been derived for and tested on images created by the naive mapmaker incorporated in HIPE, which uses a nearest-neighbour mapping algorithm. Other mapping techniques may not necessarily recreate beams with the same shape, and so it may not be appropriate to apply the same pixelisation corrections.

The following approach will yield the correct flux density of an isolated point source in an otherwise blank map:

1. Associate each map pixel flux density value with the central position of the pixel.

2. Derive the map pixel flux density that would have been recorded had the source been co-aligned with a pixel centre. This can be done by fitting the appropriate function to these data points and deriving the peak value. This function to be fitted is the beam profile convolved with the map pixel size. If the true beam profile were a 2-D Gaussian, the constrained parameters of this function would be (major axis, minor axis, position angle) and the free parameters would be (peak value, position of peak value).

3. Divide the resulting peak value by the pixelisation correction factor P.

This method may not be feasible or appropriate in all cases due to various effects such as limited S/N, sky background, confusion noise, astrometric errors, non-Gaussianity of the beam shape, etc. Any adopted method must take into account the definition of map pixel flux density given in boldface text above.

5.12.3 Appendix: tables for various conversions

A script for the *Herschel* Interactive Processing Environment (HIPE) is available and can be used to calculate the conversion parameters shown in the following tables[8]. The script uses the framework presented in this subsection and allows calculation of correction parameters for power low indices α_S or modified blackbody parameters (β, T) that are not shown in the tables. The values are derived using the calibration products (aperture efficiency, beam solid angles etc) in SPIRE_CAL_14_3. For any problems in using the script in HIPE please contact the *Herschel* Science Centre helpdesk.

Table 5.4: Effective beam solid angle, $\Omega_{\rm eff}$, and beam correction factor, $K_{\rm Beam}$, for a source with spectral index α_S. The values used in the pipeline, for $\alpha_S \equiv \alpha_{\rm pip} = -1$, are shown in bold. These values should be used to convert between flux density and surface brightness, using the same spectral index as for the colour correction.

	Effective beam solid angle $\Omega_{\rm eff}$ (arcsec^2)			Beam correction factor $K_{\rm Beam}$		
α_S	PSW	PMW	PLW	PSW	PMW	PLW
-4.0	489.28	865.62	1937.91	0.9593	0.9603	0.9311
-3.5	485.96	860.02	1915.69	0.9658	0.9666	0.9419
-3.0	482.66	854.35	1893.37	0.9724	0.9730	0.9530
-2.5	479.36	848.63	1871.01	0.9791	0.9795	0.9643
-2.0	476.04	842.87	1848.66	0.9860	0.9862	0.9760
-1.5	472.70	837.08	1826.40	0.9929	0.9931	0.9879
-1.0	**469.35**	**831.27**	**1804.31**	**1.0000**	**1.0000**	**1.0000**
-0.5	466.00	825.46	1782.44	1.0072	1.0070	1.0123
0.0	462.64	819.65	1760.89	1.0145	1.0142	1.0247
0.5	459.28	813.86	1739.71	1.0219	1.0214	1.0371
1.0	455.93	808.11	1718.97	1.0294	1.0287	1.0496
1.5	452.60	802.39	1698.75	1.0370	1.0360	1.0621
2.0	449.30	796.72	1679.09	1.0446	1.0434	1.0746
2.5	446.02	791.12	1660.03	1.0523	1.0508	1.0869
3.0	442.78	785.60	1641.62	1.0600	1.0581	1.0991
3.5	439.58	780.16	1623.90	1.0677	1.0655	1.1111
4.0	436.42	774.81	1606.87	1.0755	1.0729	1.1229
4.5	433.32	769.56	1590.56	1.0832	1.0802	1.1344
5.0	430.28	764.43	1574.97	1.0908	1.0875	1.1456

Note: $K_{\rm Beam}$ is available in the SPIRE calibration context, in a table called Phot/ColorCorrBeam. To recover $\Omega_{\rm eff}$ one can multiply $K_{\rm Beam}$ by $\Omega_{\rm pip}$ which is provided in the metadata of the table.

[8]The script is under HIPE menu
`Scripts => SPIRE Useful scripts => Photometer Calibration Bundle point.`

Table 5.5: Effective beam solid angle, $\Omega_{\rm eff}$, and beam correction factor, $K_{\rm Beam}$, for a source with grey body spectrum for emissivity indices $\beta = 1.5$ and $\beta = 2.0$. These values should be used to convert between flux density and surface brightness, using the same temperature and emissivity as for the colour correction. The effective beam solid angles and beam correction factors are integrated over the RSRF and source spectrum, following Eq. (5.35) and Eq. (5.40).

	Effective beam solid angle $\Omega_{\rm eff}(T,\beta)$ (arcsec^2)			Beam correction factor $K_{\rm Beam}(T,\beta)$		
Temp (K)	PSW	PMW	PLW	PSW	PMW	PLW
	$\beta = 1.5$					
3.0	542.20	915.31	1970.37	0.8656	0.9082	0.9157
4.0	520.40	883.72	1874.02	0.9019	0.9407	0.9628
5.0	506.15	862.30	1814.28	0.9273	0.9640	0.9945
6.0	495.45	847.26	1774.96	0.9473	0.9811	1.0165
7.0	487.24	836.29	1747.70	0.9633	0.9940	1.0324
8.0	480.82	828.03	1727.97	0.9762	1.0039	1.0442
9.0	475.72	821.65	1713.18	0.9866	1.0117	1.0532
10.0	471.58	816.61	1701.78	0.9953	1.0180	1.0602
15.0	459.22	802.14	1670.34	1.0221	1.0363	1.0802
20.0	453.33	795.55	1656.49	1.0353	1.0449	1.0892
25.0	450.01	791.89	1648.87	1.0430	1.0497	1.0943
30.0	447.92	789.59	1644.08	1.0479	1.0528	1.0975
35.0	446.50	788.03	1640.82	1.0512	1.0549	1.0996
40.0	445.48	786.90	1638.45	1.0536	1.0564	1.1012
	$\beta = 1.5$					
3.0	538.99	910.94	1950.22	0.8708	0.9125	0.9252
4.0	517.98	878.61	1852.82	0.9061	0.9461	0.9738
5.0	503.41	856.85	1793.14	0.9323	0.9702	1.0062
6.0	492.48	841.65	1754.18	0.9530	0.9877	1.0286
7.0	484.14	830.62	1727.32	0.9695	1.0008	1.0446
8.0	477.64	822.34	1707.95	0.9827	1.0109	1.0564
9.0	472.48	815.96	1693.48	0.9934	1.0188	1.0654
10.0	468.32	810.93	1682.35	1.0022	1.0251	1.0725
15.0	455.93	796.54	1651.76	1.0294	1.0436	1.0924
20.0	450.06	790.00	1638.34	1.0429	1.0522	1.1013
25.0	446.75	786.38	1630.96	1.0506	1.0571	1.1063
30.0	444.68	784.11	1626.33	1.0555	1.0601	1.1094
35.0	443.27	782.57	1623.18	1.0588	1.0622	1.1116
40.0	442.26	781.46	1620.89	1.0613	1.0638	1.1132

Note: $K_{\rm Beam}$ is available in the SPIRE calibration context, in a table called Phot/ColorCorrBeam, for a larger range of possible β, form 0 to 3. To recover $\Omega_{\rm eff}$ one can multiply $K_{\rm Beam}$ by $\Omega_{\rm pip}$ that is provided in the metadata of the table.

Table 5.6: Colour correction factors $K_{\rm ColP}$ and $K_{\rm ColE}$ (with $\alpha_{\rm pip} = -1$) as a function of assumed source spectral index. Columns (2, 3, 4) give the values for (250, 350, 500) μm for a point source flux density; columns (5, 6, 7) give the values for (250, 350, 500) μm for an extended source surface brightness. The extended source colour corrections include the variation of beam area. The colour-correction factors for a Black-Body in the Rayleigh-Jeans regime (i.e. $S_\nu \sim \nu^2$) are shown in boldface.

	Point Source ($K_{\rm ColP}$)			Extended source ($K_{\rm ColE}$)		
α_S	PSW	PMW	PLW	PSW	PMW	PLW
-4.0	0.9800	0.9791	0.9333	0.9401	0.9403	0.8689
-3.5	0.9884	0.9875	0.9525	0.9546	0.9545	0.8971
-3.0	0.9948	0.9940	0.9687	0.9674	0.9672	0.9231
-2.5	0.9992	0.9986	0.9817	0.9784	0.9782	0.9467
-2.0	1.0016	1.0011	0.9913	0.9875	0.9873	0.9675
-1.5	1.0019	1.0016	0.9974	0.9948	0.9946	0.9854
-1.0	1.0000	1.0000	1.0000	1.0000	1.0000	1.0000
-0.5	0.9960	0.9963	0.9990	1.0032	1.0034	1.0113
0.0	0.9899	0.9906	0.9945	1.0043	1.0047	1.0190
0.5	0.9818	0.9829	0.9864	1.0033	1.0039	1.0231
1.0	0.9716	0.9732	0.9751	1.0002	1.0011	1.0235
1.5	0.9594	0.9615	0.9606	0.9949	0.9962	1.0203
2.0	**0.9454**	**0.9481**	**0.9432**	**0.9876**	**0.9892**	**1.0135**
2.5	0.9296	0.9329	0.9230	0.9782	0.9802	1.0033
3.0	0.9121	0.9161	0.9005	0.9668	0.9693	0.9897
3.5	0.8930	0.8978	0.8757	0.9535	0.9566	0.9730
4.0	0.8725	0.8780	0.8492	0.9383	0.9420	0.9535
4.5	0.8507	0.8571	0.8210	0.9214	0.9258	0.9314
5.0	0.8278	0.8350	0.7916	0.9030	0.9080	0.9069

Note: this table is available in the SPIRE calibration context in Phot/ColorCorrK.

Table 5.7: Colour correction factors $K_{\rm ColP}$ and $K_{\rm ColE}$ as a function of the modified blackbody temperature, T in Kelvins, for a source with emissivity indices $\beta = 1.5$ and $\beta = 2.0$. Columns (2, 3, 4) give the values for (250, 350, 500) μm for a point source flux density; columns (5, 6, 7) give the values for (250, 350, 500) μm for an extended source surface brightness. The extended source colour corrections include the variation of beam area.

	Point source ($K_{\rm ColP}$)			Exte nded source ($K_{\rm ColE}$)		
T	PSW	PMW	PLW	PSW	PMW	PLW
	$\beta = 1.5$					
3.0	0.60	0.85	0.95	0.5235	0.7744	0.8701
4.0	0.82	0.97	1.03	0.7433	0.9168	0.9899
5.0	0.94	1.02	1.04	0.8697	0.9802	1.0339
6.0	0.99	1.03	1.03	0.9408	1.0080	1.0481
7.0	1.02	1.03	1.02	0.9807	1.0195	1.0505
8.0	1.03	1.02	1.00	1.0029	1.0230	1.0481
9.0	1.03	1.01	0.99	1.0148	1.0228	1.0439
10.0	1.03	1.00	0.98	1.0208	1.0207	1.0393
15.0	1.00	0.97	0.94	1.0185	1.0055	1.0198
20.0	0.97	0.95	0.93	1.0068	0.9940	1.0081
25.0	0.96	0.94	0.91	0.9971	0.9864	1.0008
30.0	0.94	0.93	0.91	0.9900	0.9812	0.9960
35.0	0.94	0.93	0.90	0.9846	0.9775	0.9925
40.0	0.93	0.92	0.90	0.9806	0.9747	0.9899
	$\beta = 1.5$					
3.0	0.63	0.88	0.98	0.5479	0.7986	0.9023
4.0	0.85	0.99	1.04	0.7679	0.9361	1.0119
5.0	0.96	1.02	1.04	0.8915	0.9939	1.0470
6.0	1.01	1.03	1.03	0.9586	1.0169	1.0547
7.0	1.03	1.02	1.01	0.9944	1.0246	1.0523
8.0	1.03	1.01	0.99	1.0130	1.0253	1.0464
9.0	1.03	1.00	0.98	1.0220	1.0227	1.0395
10.0	1.02	0.99	0.96	1.0254	1.0188	1.0329
15.0	0.99	0.96	0.92	1.0153	0.9984	1.0079
20.0	0.96	0.94	0.90	0.9998	0.9846	0.9938
25.0	0.94	0.92	0.89	0.9881	0.9757	0.9853
30.0	0.93	0.91	0.88	0.9796	0.9697	0.9796
35.0	0.92	0.91	0.88	0.9734	0.9655	0.9756
40.0	0.91	0.90	0.87	0.9688	0.9623	0.9727

Note: this table is available in the SPIRE calibration context in Phot/ColorCorrK for a larger range of β – from 0 to 3.

Table 5.8: Aperture corrections as a function of assumed source spectral index, assuming apertures of (22, 30, 40)$''$radius at (250, 350, 500) μm. The left three columns assume that the background is removed based on the emission in an annulus within 60-90$''$, while the right three columns assume that no background removal is done as part of the aperture photometry. If different radii for the aperture or annulus are used then the aperture corrections will need to be recalculated from the beam profile.

	Background included			No Background		
α	PSW	PMW	PLW	PSW	PMW	PLW
-4.0	1.2940	1.2550	1.2930	1.2900	1.2460	1.2540
-3.5	1.2930	1.2540	1.2900	1.2880	1.2450	1.2520
-3.0	1.2920	1.2530	1.2870	1.2870	1.2440	1.2490
-2.5	1.2910	1.2510	1.2850	1.2860	1.2430	1.2470
-2.0	1.2900	1.2500	1.2820	1.2850	1.2420	1.2450
-1.5	1.2880	1.2490	1.2790	1.2840	1.2410	1.2430
-1.0	1.2870	1.2480	1.2770	1.2830	1.2400	1.2400
-0.5	1.2860	1.2470	1.2740	1.2810	1.2390	1.2380
0.0	1.2850	1.2460	1.2710	1.2800	1.2380	1.2360
0.5	1.2840	1.2450	1.2680	1.2790	1.2370	1.2340
1.0	1.2820	1.2440	1.2660	1.2780	1.2350	1.2320
1.5	1.2810	1.2430	1.2630	1.2770	1.2340	1.2290
2.0	1.2800	1.2420	1.2610	1.2760	1.2330	1.2270
2.5	1.2790	1.2410	1.2580	1.2750	1.2320	1.2250
3.0	1.2780	1.2400	1.2560	1.2730	1.2310	1.2230
3.5	1.2760	1.2390	1.2530	1.2720	1.2300	1.2210
4.0	1.2750	1.2380	1.2510	1.2710	1.2290	1.2190
4.5	1.2740	1.2360	1.2490	1.2700	1.2280	1.2180
5.0	1.2730	1.2350	1.2470	1.2690	1.2270	1.2160

Note: this table is available in the SPIRE calibration context in Phot/ColorCorrApertureList.

Chapter 6

SPIRE Spectrometer flux calibration

The information in this Section is based on Swinyard et al. (2014), Fulton et al. (2015) and on a set of papers in the special *Herschel* dedicated Volume 37 of Experimental Astronomy.

The calibration of the spectrometer follows a different method to that adopted for the photometer. The FTS detector output is not a direct measurement of the flux density integrated over the passband as in the photometer, but depends on the Fourier components of the spectral content. Therefore Equation (5.8) is not directly applicable but an analogous equation can be used to correct for any non-linearity between absorbed power and bolometer voltage before transforming into the frequency domain. The parameters in this scheme are derived from a thermal model of the bolometer response to absorbed power.

Once a linearised voltage timeline has been obtained, the signal versus optical path difference is calculated using the SMEC position and corrections for phase error in forward and backward scans, due to the time response of the bolometers and electrical filters, are made (see Fulton et al. 2008, 2015). At this stage the timeline is referred to as an interferogram (linearised voltage as a function of the optical path difference).

The next step is to subtract the baseline of the interferogram and apply further phase correction. An apodization function (smoothing function in Fourier space) can be applied if desired. The final interferogram is then Fourier-transformed into the spectral domain, providing the voltage density $V_{\rm obs}$ in units of V/Hz.

6.1 Extended source calibration

The spectrometer bolometers receive radiation from the combination of the astronomical source, the telescope, and the instrument itself:

$$V_{\rm obs} = R_S\, I_S + R_{\rm Tel} M_{\rm Tel} + R_{\rm Inst} M_{\rm Inst}, \tag{6.1}$$

where $V_{\rm obs}$ is the measured voltage density, R_S, $R_{\rm Tel}$, and $R_{\rm Inst}$ are the relative spectral response functions (RSRFs) applicable to the source, telescope and instrument, $I_S(\nu)$ is the source intensity and $M_{\rm Tel}$ and $M_{\rm Inst}$ are the corresponding telescope and instrument models intensities. In the case of the instrument, $M_{\rm Inst}$ is due to the thermal emission from within the ~ 5 K FPU enclosure.

The emission from the telescope, assuming that there is no stray light, and taking account of emission from both the primary (M1) and secondary (M2) mirrors, and reflection from the secondary, is modelled as a sum of two black-bodies:

$$M_{\rm Tel} = (1 - \varepsilon_{\rm M2}) E_{\rm corr} \varepsilon_{\rm M1} \mathcal{B}(T_{\rm M1}, \nu) + \varepsilon_{\rm M2} \mathcal{B}(T_{\rm M2}, \nu), \tag{6.2}$$

where $\mathcal{B}(T, \nu)$ is the Planck function as given in Eq. 5.24, expressed in terms of frequency so that the final units can be easily converted to Jy, ε are the mirror emissivities. During the mission, the emissivity of the primary mirror was found to change with time, and so is corrected by a time dependent factor, $E_{\rm corr}$ (Hopwood et al., 2014). The temperatures of the telescope primary and secondary mirrors, $T_{\rm M1}$ and $T_{\rm M2}$, are measured by thermistors on the spacecraft and these are available as auxiliary products in the observation context. The emissivity of the primary and secondary mirrors were measured before the launch by Fischer et al. (2004) and modelled as

$$\varepsilon = 0.0336 \left(\frac{c}{\nu}\right)^{-0.5} + 0.273 \left(\frac{c}{\nu}\right)^{-1}, \tag{6.3}$$

where ν is the frequency in kHz and c is the speed of light in vacuum.

The emission due to the internal temperature of the instrument is also modelled as a black-body with the instrument baseplate temperature, $T_{\rm Inst}$, measured by FPU thermistors:

$$M_{\rm Inst} = \mathcal{B}(T_{\rm Inst}, \nu). \tag{6.4}$$

To obtain the source spectrum, Eq. 6.1 can be re-arranged, giving

$$I_S = (V_{\rm obs} - R_{\rm Inst} M_{\rm Inst} - R_{\rm Tel} M_{\rm Tel}) / R_S. \tag{6.5}$$

The telescope and instrument RSRFs are derived from observations of a dark region of the sky, which were made throughout the mission and we assume $R_{\rm Tel} \equiv R_S$. The final source spectrum $I_S(\nu)$ has surface brightness units of W m^{-2} Hz^{-1} sr^{-1}, which can be converted to MJy sr^{-1} via multiplication by 10^{20}.

The derived $R_{\rm Tel}$ is the extended source calibration for the FTS. It assumes that $M_{\rm Tel}$ is a good representation of the telescope emission in the SPIRE bands and that the telescope is a fully extended source compared to the beam. Furthermore, for fully extended sources, the far-field feedhorn efficiency $\eta_{\rm ff}$ needs to be taken into account (see Wu et al. 2013; Valtchanov et al. 2016). This correction, $\eta_{\rm ff}$, is the loss of efficiency of feedhorn coupled bolometers for sources that fully fill the aperture. Without correcting for $\eta_{\rm ff}$, the synthetic photometry from $I_S(\nu)$ for flat and fully extended sources, when compared with the corresponding maps from SPIRE Photometer, shows a significant and systematic difference: the spectrometer intensities are factors of (1.4, 1.5, 1.8) than the (250, 350, 500) μm broad band intensities from the extended source *Planck*-HFI zero-level calibrated maps. The far-field feedhorn efficiency correction curves for SSW and SLW shown in Fig. 6.1 were introduced in HIPE v14 and SPIRE_CAL_14_2, and can be accessed from the SPIRE Calibration Tree. In the current pipeline (see Fulton et al. 2015), the final extended calibrated source spectrum is $I_S(\nu)/\eta_{\rm ff}$, where $I_S(\nu)$ comes from Eq. 6.5. Spectra from HIPE versions before 14 can be corrected using the same conversion.

The impact of $\eta_{\rm ff}$ on extended calibrated spectra is significant as all previous studies based on extended-source-calibrated spectra (sparse and mapping mode) are underestimated by 40-100%.

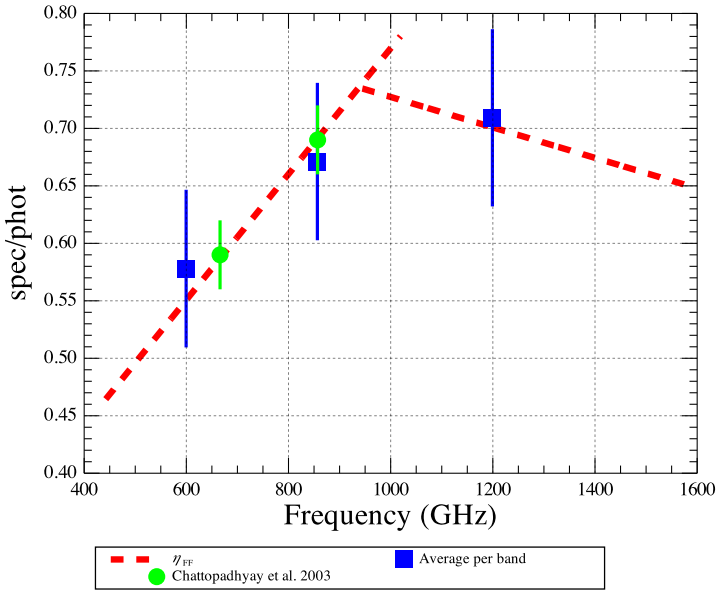

Figure 6.1: The far-field feedhorn efficiency correction, $\eta_{\rm ff}$ (red dashed lines), for SSW and SLW. The filled blue squares are the average per band ratio of the synthetic photometry from $I_S(\nu)$ and the photometry from the SPIRE photometer extended calibrated maps for 24 spatially flat sources (see Valtchanov et al. 2016), before taking into account $\eta_{\rm ff}$. The error bars include the uncertainties from the *Planck*-HFI derived zero offsets for the SPIRE photometer extended source calibrated maps. The two green filled circles are the ground-based pre-flight measurements of $\eta_{\rm ff}$ (Chattopadhyay et al., 2003).

6.2 Point source calibration

A point source conversion factor $C_{\rm point}$ is required to convert from the extended-source-calibrated spectrum to a point-source calibrated one. In the current calibration framework the derivation of $C_{\rm point}$ is invariant with respect to the extended calibration, because it is determined from observations and a model of Uranus:

$$C_{\rm point} = \frac{M_{\rm Uranus}}{I_{\rm Uranus}}, \tag{6.6}$$

where $M_{\rm Uranus}$ is the Uranus model described in Section 4.1 and in Swinyard et al. (2014), and $I_{\rm Uranus}$ is the extended-calibrated spectrum of Uranus, before correcting for $\eta_{\rm ff}$. $I_{\rm Uranus}$ is in units of (W m^{-2} Hz^{-1} sr^{-1}). This conversion $C_{\rm point}(\nu)$ can be accessed from the SPIRE Calibration Tree within HIPE.

6.3 Spectrometer beam properties

The FTS beam profile has been measured directly as a function of frequency by mapping a point-like source (Neptune) at medium spectral resolution (Makiwa et al., 2013), covering a circular region of diameter $90''$ centred on the beam. The beam profile shows a complex dependence on frequency due to the SPIRE FTS optics and the multi-moded nature of the feedhorn coupled detectors. The

feedhorns consist of conical concentrators in front of a circular-section waveguide, and the diameter of the waveguide determines the cut-on frequencies of the electromagnetic modes that are propagated (Chattopadhyay et al., 2003; Murphy & Padman, 1991).

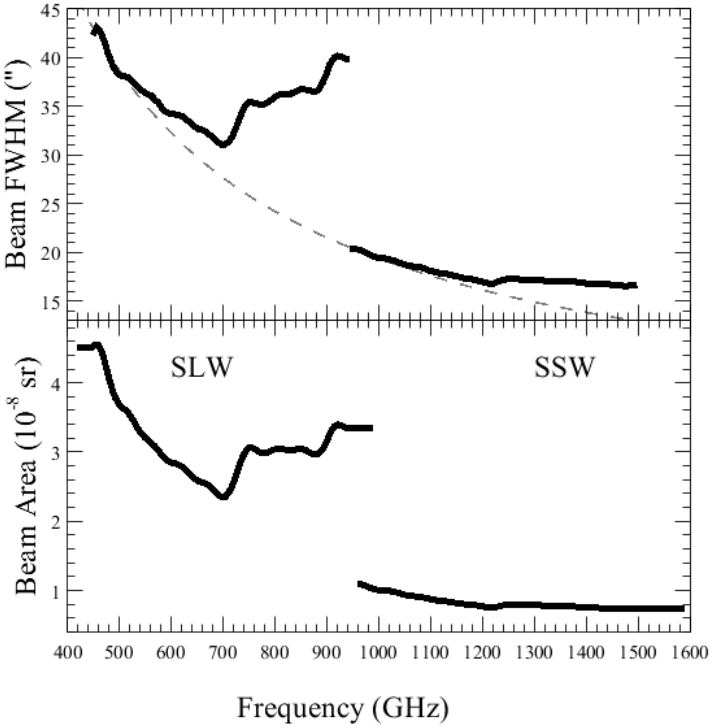

Figure 6.2: Top: the FWHM of the SPIRE FTS beam profile as fitted by Makiwa et al. (2013). The grey dashed line in the top plot shows the expected FWHM from diffraction theory. Bottom: the measured beam area from Makiwa et al. (2013).

Makiwa et al. (2013) fitted the measured Neptune data using a superposition of Hermite-Gaussian functions. They found that within the uncertainties of the measurement, only the zeroth order function (i.e. a pure Gaussian) was required for the SSW band. However, the SLW band required the first three basis functions. These fitted functions are a convenient mathematical description of the beam, rather than directly representing the electromagnetic modes propagating through the waveguides. The beam is well fitted by radially symmetric functions.

The resulting FWHM of the fitted profile is shown in Figure 6.2 together with the expectation for basic diffraction (calculated as the FWHM of an Airy pattern with effective mirror diameter of 3.287 m). The beam size matches the diffraction limit only at the low frequency end of each band, where the waveguide is single-moded. As further modes propagate, their superposition leads to beam FWHM larger than expected from diffraction theory.

The beam solid angles, shown in Fig. 6.2, can be used to convert from point-source and extended-source calibrated spectra via

$$F_S(\nu) = \Omega_{\rm beam} \times I_S(\nu)/\eta_{\rm diff}, \tag{6.7}$$

where $F_S(\nu)$ is the flux density and $I_S(\nu)$ is the intensity, corrected for the diffraction loss of a point source on axis due to the telescope secondary mirror and the support structure, $\eta_{\rm ff}$, which is derived using a simple physical optical model as in Caldwell et al. (2000). Alternatively

$$\eta_{\rm diff} = \frac{I_{\rm Uranus} \times \Omega_{\rm beam}}{F_{\rm Uranus}}, \tag{6.8}$$

where $F_{\rm Uranus}$ is the primary calibrator flux density from the ESSA-4 model and $I_{\rm Uranus}$ is the observed intensity from the extended source calibration. Confirmations of Eq. 6.7 for Uranus (point source) and for a fully extended source are shown in Fig. 6.3. Overall, both calibration schemes agree at a level of $\pm 5\%$, with higher deviations in the noisier parts of the frequency ranges.

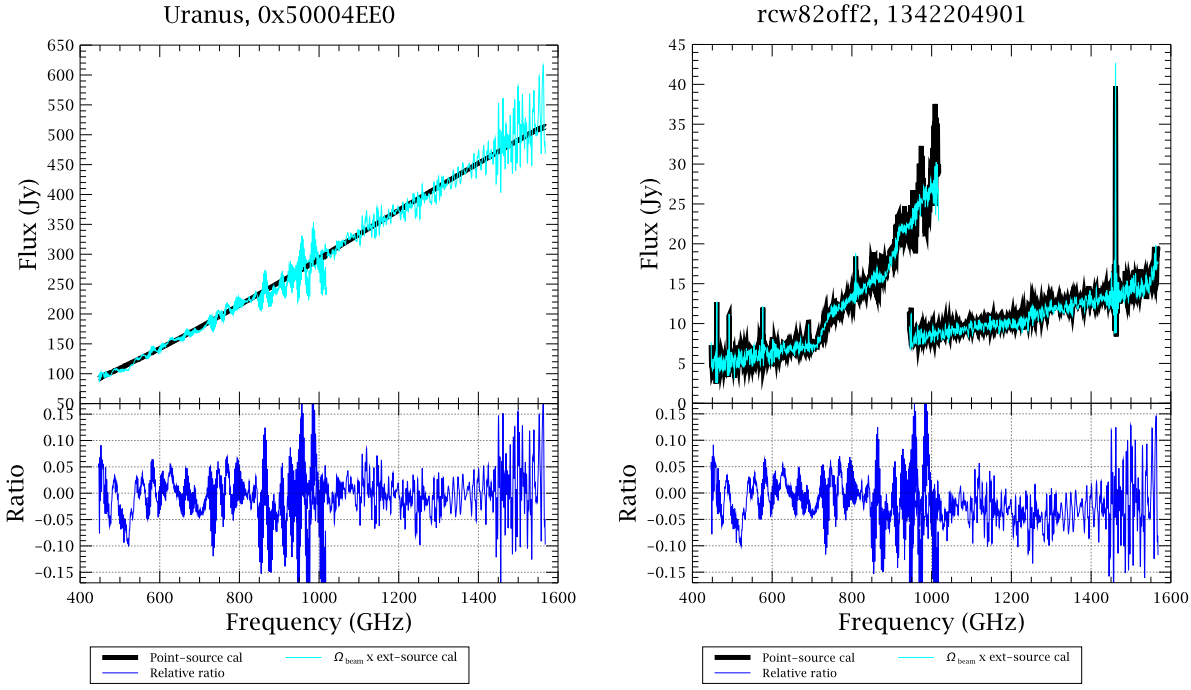

Figure 6.3: Left panel: comparison of the Uranus pipeline derived point-source calibrated flux density $F_S(\nu)$ in Jy (thick black line) with the flux density derived from the extended-source calibrated intensity $I_S(\nu) \times \Omega_{\rm beam}/\eta_{\rm diff}$. The point-source calibrated spectrum of Uranus is equivalent to the Uranus model (primary calibrator). The relative ratio is shown in the bottom panel. The overall agreement, in the less noisy parts of the two bands, is within 5%. Right panel: the same comparison for a fully extended source.

6.4 Spectral mapping

Spectral mapping observations are performed using all of the detectors in the spectrometer arrays. In the case of fully sampled (Nyquist sampled) or intermediate sampled (twice Nyquist spacing) maps, the individual 1-D spectra from all detectors at all jiggle or raster positions can be gridded on a regular sky grid to produce 3-D spectral cubes. The individual spectra from the detectors are extended-source calibrated, therefore corrected for $\eta_{\rm ff}$ (see Sec. 6.1). Two different methods of gridding are used by

the pipeline: naive projection and convolution projection (see Fulton et al. 2015 and The SPIRE Data Reduction Guide). Both are available as standard pipeline products. Flat fielding across detectors is taken into account by deriving a separate RSRF for each bolometer. The uncertainties of the mapping mode for naive cubes are detailed in Benielli et al. (2014).

6.5 Semi-extended sources

The extended calibration assumes a fully extended source in the beam, while the point-source calibration assumes a source much smaller than the beam. Sources with size between these two extremes, i.e. semi-extended sources, need special treatment as neither of the two calibration schemes is appropriate. The theory and some practical applications of the correction method are presented in Wu et al. (2013), while here we briefly outline the main considerations.

Starting from a point-source calibrated spectrum, we correct for the source area and the source-beam coupled area:

$$F_s = F_{\rm point} \times \eta_c \times \frac{\Omega_{\rm source}}{\eta_f(\nu, \Omega_{\rm source})\,\Omega_{\rm beam}(\nu)}, \tag{6.9}$$

and the beam areas are defined as:

$$\Omega_{\rm source} = \iint_{2\pi} D_\nu(\Psi)\mathrm{d}\Psi, \tag{6.10}$$

$$\Omega_{\rm beam} = \iint_{2\pi} P_\nu(\Psi)\mathrm{d}\Psi, \tag{6.11}$$

where $D_\nu(\Psi)$ is the source surface brightness distribution and $P_\nu(\Psi)$ is the beam profile. Both distributions are normalised to have a peak of unity. The source-beam coupling efficiency η_f (also called the forward coupling efficiency, in e.g. Ulich & Haas 1976) is

$$\eta_f = \frac{\iint_{2\pi} P_\nu(\Psi - \Psi_0) D_\nu(\Psi)\mathrm{d}\Psi}{\iint_{2\pi} P_\nu(\Psi)\mathrm{d}\Psi}, \tag{6.12}$$

where Ψ_0 accounts for any offset of the source from the centre of the beam. We assume the source distribution is constant with frequency and the correction efficiency $\eta_c = 1$ (see Wu et al. 2013 for details). Substituting the definitions in Eq. 6.9 we obtain:

$$F_s = F_{\rm point} \times \frac{\iint_{2\pi} D_\nu(\Psi)\,\mathrm{d}\Psi}{\iint_{2\pi} P_\nu(\Psi - \Psi_0)\,D_\nu(\Psi)\,\mathrm{d}\Psi}, \tag{6.13}$$

where the denominator is the source-beam coupling in steradians.

Sometimes it may be desirable to calculate the flux density which would be observed in a reference beam that is constant with frequency, thus enabling the spectrum to be compared with observations using other telescopes with different beams. This could be achieved by replacing the numerator by the source-beam coupling to the reference beam:

$$F_{\rm s-ref} = F_{\rm point} \times \frac{\iint_{2\pi} P_{\rm ref}(\Psi)\,D_\nu(\Psi)\,\mathrm{d}\Psi}{\iint_{2\pi} P_\nu(\Psi - \Psi_0)\,D_\nu(\Psi)\,\mathrm{d}\Psi}, \tag{6.14}$$

where $\iint_{2\pi} P_{\rm ref}(\Psi)\,\mathrm{d}\Psi = \Omega_{\rm ref}$ is the reference beam solid angle; the reference beam is always centred on the source. Setting $\Omega_{\rm ref}$ to a very large value is equivalent to $P_{\rm ref}(\Psi) \approx \max[P_{\rm ref}(\Psi)] \equiv 1$, and consequently we recover the total flux density as given in Eq. 6.13.

The practical implementation of the method is described in the the SPIRE Data Reduction Guide, where some limitations and caveats of the Semi-Extended Correction tool (SECT) are also discussed.

It is interesting to note that source-beam coupling can account for a pointing offset of the beam with respect to the source. Hence, in cases when both the source model and the pointing offset are well known then the latter can be corrected.

6.6 Low resolution observations

For H+LR SLW spectra that have been produced by the standard HIPE v13 pipeline (or with earlier versions), a significant systematic difference can be seen between the high-resolution (HR) and low-resolution (LR) continuum levels. This difference manifests itself as a characteristic double-bump, with peaks at 550 and 900 GHz (as shown in Fig. 6.4). The analysis of sequential pairs of HR and LR dark sky observations (as detailed in Marchili et al. 2016), shows that for LR observations made directly after the use of HR mode, the same double-bump residual is present as for the LR spectra of H+LR. This strongly suggests the problem is linked to the sequence in which the spectra are taken. The amplitude of the double-bump affecting LR spectra depends on the timeline of previous observations, and in particular on the time distance from the most recent HR observation and the integration time of this observation.

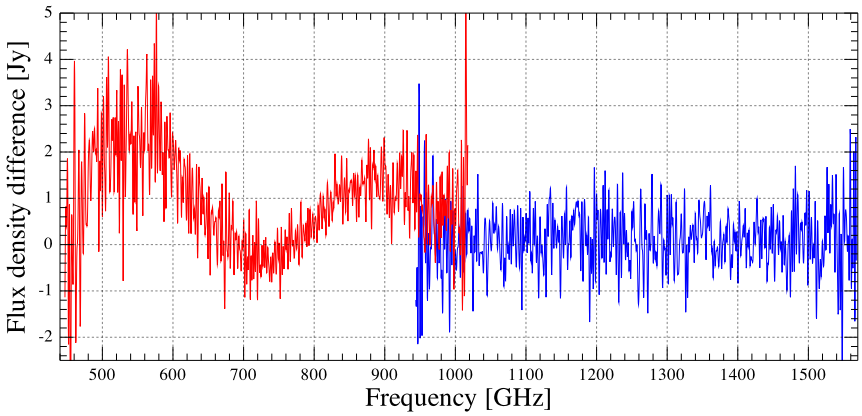

Figure 6.4: The difference between the HR and LR point-source calibrated spectra for the centre detectors of the H+LR observation 1342253971. SSW is essentially flat, whereas there is a bumpy distortion in the difference for SLW. The peaks seen at 500 and 900 GHz are introduced by artefacts in the LR data. The LR data were interpolated onto the HR frequency scale before subtraction from the HR data.

Marchili et al. (2016) attribute this discrepancy between different resolution modes to fast variations of the instrument temperature. The movement of mechanical parts within the instrument (the SMEC) triggers temperature variations. Sudden increases of temperature modify both the instrument and the telescope response functions ($R_{\rm Inst}$ and $R_{\rm Tel}$), and so the calibration is no longer completely effective. After an HR observation is completed, the system returns to its original equilibrium state, however this takes several hours and any LR data taken during this period will suffer from the double-bump artefact in the SLW spectra.

Since the bump amplitudes depend on the history of previous observations, and since no housekeeping parameter can precisely trace this history, this distortion of the spectra cannot be corrected through an analytical procedure. Given that the double-bump shape observed is characteristic of all affected spectra, it is possible to derive an empirical correction that evaluates the amplitude of the double-bump and removes it, without any modification of unaffected spectra. An empirical LR correction for point-source calibrated SLW spectra was introduced in HIPE v14 and the corresponding calibration file is included in SPIRE_CAL_14_2.

The full analysis of this systematic noise and the derivation of the empirical correction to remove it, are presented in Marchili et al. (2016).

6.7 Bright source mode

To avoid saturating the detectors, bright targets, such as Orion, Sgr B2 and Mars, or any target with a continuum level greater than 500 Jy, were observed with the FTS using bright source mode.

In the measured interferogram, the total power received is reflected in the amplitude of the modulation at zero path difference (ZPD). This means that for any particular observations, once a certain source strength is reached, the amplitude of modulation may exceed the dynamic range specified and the interferogram can be clipped. Signal clipping can occur either at the maximum or the minimum of the interferogram, and as a consequence can be corrected only if there are a small number of consecutive samples clipped. For bright sources, the clipping can be severe. And in cases where it is impossible to correct interferograms clipped close to ZPD, the continuum shape and level will be affected across the spectrum. Bright source mode is designed to avoid saturation of the detectors by using a different bias amplitude and phase for the bolometers, which lowers their responsivity and so reduces the maximum modulation in the interferogram. When observing in bright mode, the dynamic range of the detectors was set for every jiggle position of an intermediate or fully sampled mapping observations. Whereas the range was set once at the beginning of nominal mode mapping observations.

For sources up to the strength of Mars ($\sim 15,000$ Jy), bright mode significantly reduces clipping and in most cases it is completely avoided for the central detector pair.

The impact of clipping on spectral lines is minimal. Clipping only occurs around the peak modulation in the interferogram, whereas information relating to spectral lines is spread throughout the interferogram, up to large optical path differences.

The calibration of the FTS bright source mode is presented in greater detail in Lu et al. (2014).

6.8 Comparison with the SPIRE photometer

Synthetic photometry can be extracted from FTS spectra following Eqs. 5.10 and 5.11, for point-source calibration, and Eqs. 5.14, 5.19 and 5.39 for extended-source calibration.

Comparison of the monochromatic flux densities extracted from point-source calibrated Spectrometer spectra and Photometer maps, is presented in Hopwood et al. (2015). A good agreement was found at a level of 3-5% for the three photometer wavebands (see Section 7 and Figures 28-29 in Hopwood et al. 2015).

Eqs. 5.14 and 5.19 can be used to compare extended-source calibrated spectra and photometer maps at the three photometer bands. $K_{\rm MonE}$ should be applied to derive the synthetic monochromatic intensity for a source with constant νI_ν. This synthetic photometry can be directly compared with photometry taken from the extended calibrated photometer maps, which have been corrected with the *Planck* derived zero offsets.

Prior to HIPE version 14, the FTS extended calibration did not account for the far-field feed horn efficiency ($\eta_{\rm ff}$). As a consequence, any Spectrometer and Photometer comparison made with data reduced with an earlier version of HIPE will show a discrepancy, with the photometer intensity higher by a factor of 1.4-2.0. Applying $\eta_{\rm ff}$ for a selection of 24 sources that are spatially flat within the FTS beam, gives median Photometer to Spectrometer ratios of 0.99 ± 0.04, 1.05 ± 0.04 and 0.97 ± 0.08, at 250, 350 and 500 μm (see Figure 6.1 and Valtchanov et al. 2016 for further details). This result is at a comparable level to the 3-5% found for the point-source calibrated data in Hopwood et al. (2015). This result only applies to truly extended sources, i.e. sources spatially flat within the FTS beam. If there is surface brightness structure within the beam, or the source is semi-extended, the results of a similar comparison are likely to be significantly worse, as in these cases the source-beam coupling cannot be fully accounted for with the extended-source calibration scheme.

Chapter 7

SPIRE calibration accuracy

7.1 Photometer calibration accuracy

SPIRE photometer observations are subject to several kinds of uncertainty.

Absolute calibration uncertainty: This component is associated with our knowledge of the brightness of the primary calibrator, Neptune, and is estimated at $\pm 4\%$ (ESA-4 model, R. Moreno, private communication). It is correlated across the three bands, i.e. flux densities in the three bands will move up or down in a linearly correlated manner in the event of this calibration being revised.

Relative calibration uncertainty: This uncertainty arises from the ability of the instrument to reproduce a measurement of the same flux at the same time. This is a random contribution and has been estimated by careful analysis of repeated measurements of a bright source (actually Neptune itself, e.g. Bendo et al. 2013). It should be noted that the flux of Neptune actually varies due to its well known distance from the observatory. With more systematic effects potentially contributing, this is a more realistic estimate of random uncertainty than repeated observations of a bright source at constant flux. The results show that this component is of the order of 1.5% (Bendo et al., 2013).

At present, we recommend that the overall calibration uncertainty for the SPIRE photometer, taking these two contributions into account, should be taken conservatively as $\pm 5.5\%$ (the direct rather than quadrature sum of the absolute and relative calibration uncertainties). It should be noted that this is dominated by the absolute component and is thus largely correlated across the three bands.

Photometric uncertainty: This component is due to the source measurement errors. The photometer pipeline produces timelines representing the the in-beam flux density, and some random detector noise will be present in the timelines. Any astrometric errors will also introduce additional noise when timelines are combined in mapmaking. In addition, in order to derive estimates of, for example, the flux density of a point or compact source, users will need to employ some suitable fitting or aperture photometry technique, and additional uncertainties can be introduced due to confusion or source crowding. In addition, slight differences in the choice of pipeline parameters (e.g., for the deglitching and baseline subtraction modules) may produce slightly different results (at the level of a few percent).

It is important to note that these photometric uncertainties will be significant or dominant except for sources which stand out very clearly above any confusion noise or local sky background fluctuations (in which case the calibration uncertainties described above will become significant or dominant).

Assessment of the photometric uncertainties will depend on the particular sky brightness distribution and on the source extraction or background subtraction methods, and is is therefore something to be done carefully by the user.

See Section 5.12.2 for some additional considerations relating to the process of point source extraction.

Extended source calibration uncertainty: In addition to the components described above, the calibration accuracy of extended sources is limited by the uncertainty on the SPIRE beam solid angle (Griffin et al., 2013), and for absolute surface brightness measurements, from the uncertainty in the *Planck*-derived map offsets. The beam solid angle measurements are based on observations of Neptune, with a diffuse and point source backgrounds removed from the resulting maps using shadow observations (Schultz et al, in prepraion). This background removal leaves an uncertainty of $< 1\%$ on the resulting beam solid angles. The uncertainties associated with the *Planck*-derived offsets are of the order of 10%, depending on the source distribution in the maps as the *Planck*-HFI beam is relatively large, comparable to the size of the SPIRE Small Maps.

It should be noted that (i) the offsets are normally small in comparison to the SPIRE signals, so that this 10% uncertainty is not normally a significant contributor to the overall error budget and (ii) for science analysis involving differential measurements on SPIRE maps, such as point source photometry or aperture photometry, the uncertainty associated with the *Planck* offsets has no effect on the results.

7.2 Spectrometer calibration accuracy

The overall error budget for the FTS is summarised in this section, and more details on calibration uncertainties can be found in Swinyard et al. (2014) and Hopwood et al. (2015). We break the uncertainties into three categories: point sources observed in the sparse mode, extended sources observed in the sparse mode, and extended sources observed in mapping mode. The calibration described in this paper has been implemented in the pipeline corresponding to HIPE v12.

To summarise for point sources observed on the centre detectors (SSWD4 and SLWC3), the measured repeatability is 6%, with the following contributions:

- Absolute systematic uncertainty in the models from comparison of Uranus and Neptune models – determined to be $\pm 3\%$. The cross-comparison of the SPIRE spectrometer and photometer (Swinyard et al. 2014, section 6.3) indicates good consistency of the Neptune ESA-4 model to both Uranus and Mars.
- The statistical repeatability determined from observations of Uranus and Neptune, with pointing corrected – estimated at $\pm 1\%$.
- The uncertainties in the instrument and telescope model which lead to an additive, average per band, continuum offset error of 0.4 Jy for SLW and 0.3 Jy for SSW, with frequency dependence as shown in Fig. 7.1, right panel.
- The effect of the *Herschel* pointing APE.

Note that the pointing uncertainty results only in a reduction in flux and is therefore not a true statistical uncertainty on the recovered flux level. A large pointing offset also results in a significant distortion

of the SSW spectrum of a point source and a mismatch between the SLW and SSW spectra. Providing one is convinced that the source in question has no spatial extension, the SLW portion of the calibrated spectrum can be used to correct any apparent gain difference between the SLW and SSW spectra.

For sparse observations of truly extended sources, the absolute uncertainty in flux for a reasonably bright fully extended object observed in the central detectors is $\sim \pm 4\%$, with the following contributions:

- The systematic uncertainty in telescope model of 0.06%
- The statistical repeatability estimated at $\pm 1\%$
- An additive continuum offset as shown in Fig. 7.1, left panel, with average values per band of
  - SLW: 9.4×10^{-20} W m^{-2} Hz^{-1} sr^{-1}= 9.4 MJy/sr,
  - SSW: 2.3×10^{-19} W m^{-2} Hz^{-1} sr^{-1}= 23 MJy/sr.
- Uncertainty of the far-field feedhorn efficiency $\eta_{\rm ff}$ estimated at $\pm 3\%$ for SLW. For SSW, $\eta_{\rm ff}$ was not measured and the uncertainty is unknown. But because of the simpler beam properties for SSW we assume the uncertainty to be the same.

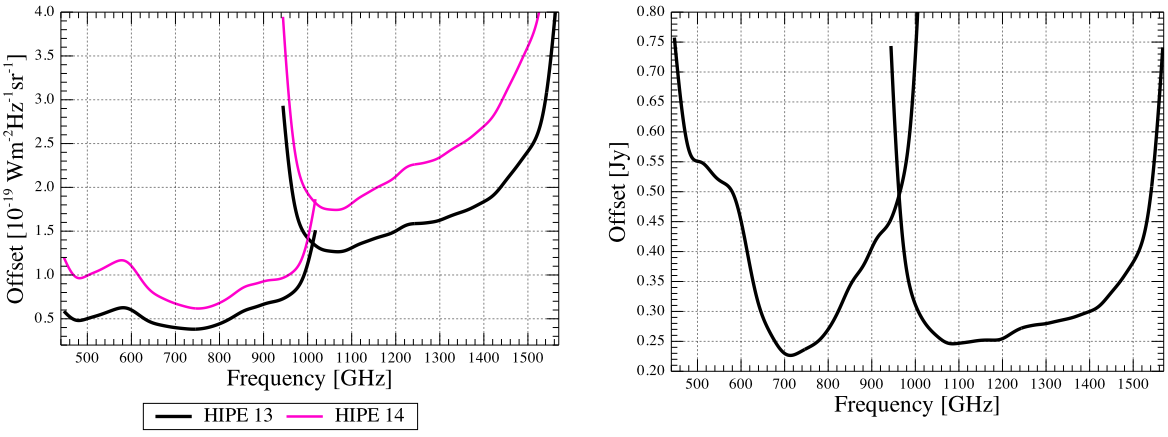

Figure 7.1: Additive continuum offsets for extended-source (left) and point-source calibration (right). The extended calibration offsets were significantly underestimated for processing before HIPE v14 due to the missing far field feedhorn efficiency correction (see Section 6.1 for more details).

In practice, truly extended sources tend to be faint and the uncertainty is therefore dominated by the additive offsets. When the source extent is larger than the beam size, but not fully extended, or if there is structure inside the beam, then the uncertainties are dominated by the source-beam coupling (see Wu et al., 2013) and significantly greater than 4%.

Comparison of the synthetic photometry for 24 selected extended and spatially flat sources with extended calibrated maps shows an agreement at 3-5% level, bearing in mind the 10% uncertainty of the maps zero-offsets derived from *Planck*-HFI.

For spectral maps, the variations between detectors become important and the overall repeatability has been measured to be $\pm 7\%$ (see Benielli et al., 2014, for a full discussion of mapping mode observations). The off axis detectors are less well calibrated, especially outside the unvignetted part of the field.

The level of absolute flux accuracy and repeatability for point-source calibrated spectra obtained with the SPIRE FTS compares favourably with the SPIRE photometer: 1.5% repeatability and 4% absolute, initially presented in Bendo et al. (2013) and extended to all FTS calibrators in Hopwood et al. (2015).

The level of calibration accuracy achieved is due to the nature of an FTS, where both the continuum and narrow spectral features are observed in the same measurement. Thus, spectral features with a wide frequency structure are observed together and can be analysed and corrected for simultaneously. This is not possible with monochromatic devices where essentially only a single frequency structure is observed leading to possibly unknown spectral features causing calibration uncertainties (for instance standing waves or broad spectral features in the instrument response function). The penalty in instantaneous sensitivity due to the increased photon noise in an FTS is therefore compensated to some extent by the much higher level of calibration fidelity achieved.

7.3 Future updates

The current calibration and pipelines for the SPIRE photometer, as introduced in HIPE v14 and SPIRE_CAL_14_3, are considered stable.

For the photometer, the ESA-4 model for the primary calibrator Neptune is not expected to change in the near future, at least not in a significant way as to require new calibration parameters and products. For extended calibrated maps, the current estimates for the beam solid angles are accurate to better than 1% (HIPE v14 and SPIRE_CAL_14_3) and it is unlikely that a significantly higher accuracy could be achieved. Post HIPE v14 changes are more likely for the *Planck*-HFI derived zero-point offsets, which are currently uncertain at a level of $\pm 10\%$. In case of an update of the *Planck* zero-point calibration by the *Planck* team, an overall change by a constant offset per filter band is most likely, given the much higher relative accuracy within a *Planck* map. Possible changes in relative photometric gain between *Planck*-HFI and *SPIRE* resulting from a new zero-point calibration are expected to be negligible.

For the spectrometer, significant improvements to the point-source calibration are not envisaged in the future. The basis of the calibration, the Uranus ESA-4 model, is considered accurate enough in the SPIRE bands and further small improvements in the model, even at a percentage level, have to be evaluated carefully before accepted for implementation.

Chapter 8

SPIRE observations in the Herschel Science Archive

In this chapter we briefly describe the data products and the data structure coming from SPIRE observations. A comprehensive description, and practical guidelines for accessing the data, running the pipeline and doing quick interactive analysis can be found in the SPIRE Data Reduction Guide, which can be accessed also from the help documentation inside the *Herschel* Interactive Processing Environment (HIPE).

The data structure for the *Herschel* mission is unusual for astronomers as it is object-oriented – the underlying pipeline processing and the database that hold all the data are based on Java. Before *Herschel*, no other ground-based or space observing facility provided similar access to the collected data. In some situations the data access and the data structure may seem confusing. In such cases please do not hesitate to contact the helpdesk of the *Herschel* Science Centre.

8.1 SPIRE processing levels and structure of the observational context

All standard *Herschel* SPIRE observations are now publicly available in the *Herschel* Science Archive (HSA). Guidance on getting observations from the HSA is given in greater detain in Section 1.4 of the HIPE Data Analysis Guide. In order for the user to know where to look for the products of interest (maps, spectra, spectral maps), one has to be a familiar with the data structure of the archive file downloaded from the HSA.

All SPIRE data products are grouped into contexts. A context is a special kind of product linking other products in a coherent description and can be thought of as an inventory or catalogue of products. The SPIRE processed observation consists of many such contexts enclosed within one observation context. Each processing level in the SPIRE pipeline has a context and the entire observation has a context. Thus a complete observation may be thought of as a big SPIRE onion as depicted in Figure 8.1. Moreover, contexts are not just for higher level pipeline processed data products, but there are contexts for Calibration Products, contexts for Auxiliary Products (e.g. telescope pointing, mirror temperatures etc.) and a context for a high level Quality Control. The entire SPIRE Observational Context is shown in Figure 8.1 for all products from the raw building block data to the final high-level-processed end-products from the pipeline.

Figure 8.1: The complete Observation Context of a SPIRE observation.

Each SPIRE observation in the HSA has already been processed through the standard pipelines to several levels, this processing is known as Systematic Product Generation (SPG). All observations are regularly reprocessed in bulk, whenever there is a new release of the *Herschel* Common Software System (HCSS). The SPG version, present in the metadata of any Observational Context, reflects the HCSS version of the reprocessing.

The different processing levels of the SPIRE pipeline and user deliverables are outlined in Figure 8.2. In general, Level 0 data corresponds to the raw data, formatted from the raw telemetry by an external pre-processing stage. These Level 0 Data Products are then passed through a processing stage referred to as the Engineering Conversion that creates the Level 0.5 Data Products in a meaningful and manageable form. The SPIRE AOT specific pipelines then process these Level 0.5 Data Products to produce the science usable, calibrated Level 1 Data Products. Further advanced processing to create products such as maps produce the high-level Level 2, Level 2.5 and Level 3 Data Products. Quality Control is carried out by the *Herschel* Science Centre and quality summary is included in the observation, only if there are some concerns regarding the science grade of the final products. With a few exceptions, no quality checks were performed on calibration observations.

Level 2.5 and Level 3 products are only available for the SPIRE photometer, starting from HIPE v11 and later. Level 2.5 is for the combined maps from Parallel mode in separated nominal and orthogonal

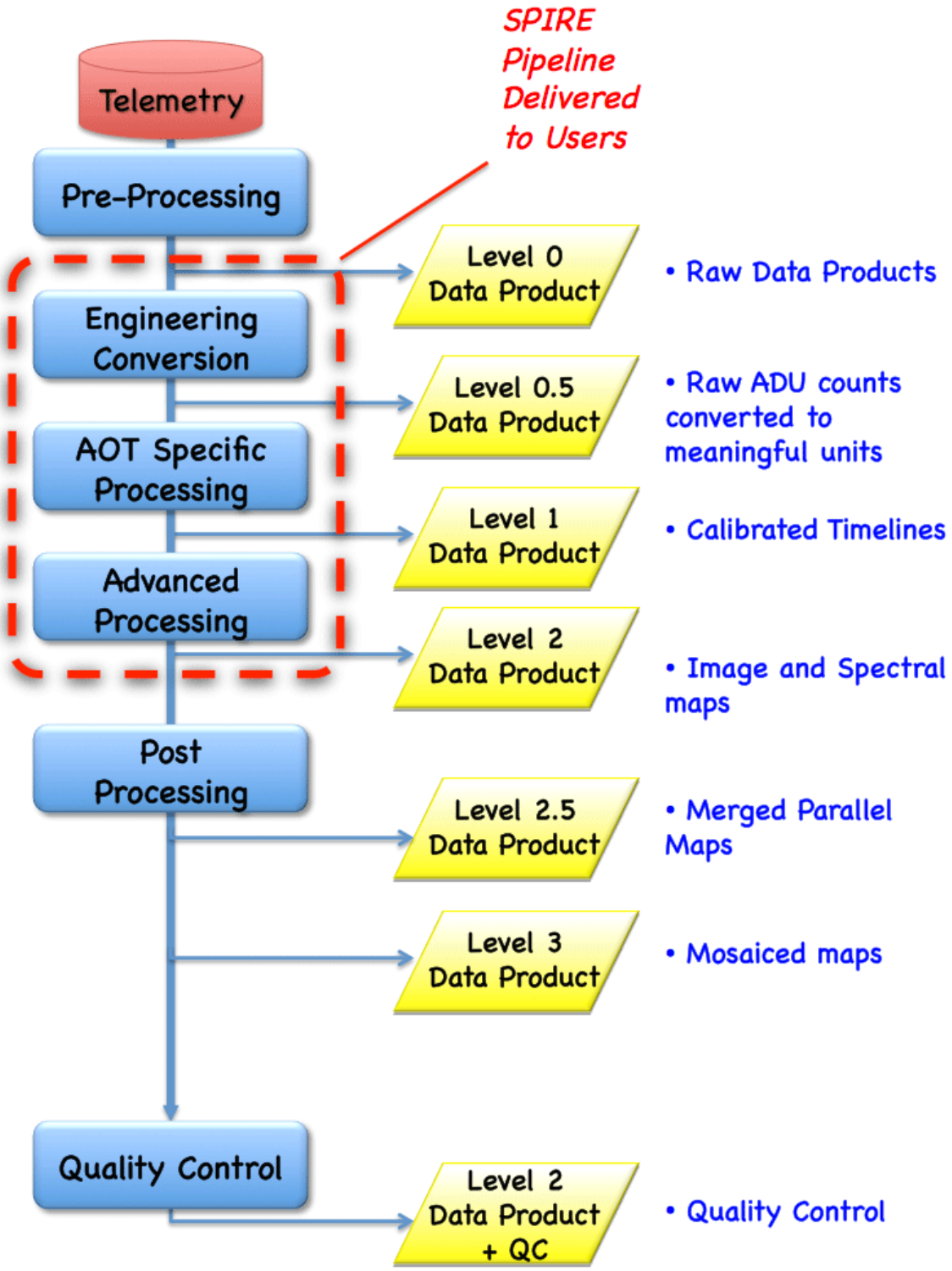

Figure 8.2: The processing levels of the SPIRE pipeline and user deliverables. Level 2.5 and Level 3 are only available for the Photometer and for subsets of observations.

scan directions or SPIRE-only observations, when there is a suitable overlap. Note that all Level 2.5 maps are made using the timelines at Level 1, while Level 3 maps are a naive mosaic of maps over a contiguous area.

8.2 Quality Control on SPIRE observations

Quality Control (QC) was carried out incrementally on all SPIRE observations, excluding calibration observations. During the active phase of the *Herschel* mission, high level quality checks were performed at the *Herschel* Science Centre, in order to react and reschedule any observation that may have failed due to instrument or spacecraft commanding problems. The pipelines also calculate different QC parameters, which are described in greater detail in the SPIRE Quality Control Metrics document. The final thresholds, based on trend analysis on all observations, are incorporated in the pipeline and in the QC Metrics table. The QC parameters are calculated for all relevant products and the values are available in the corresponding metadata. In the Quality Context, however, only those above the threshold are listed, together with a QC summary text message. For SPIRE observations, the HSA only shows the QC Summary Message in the QC Report block. Usually, QC Summary text only appears if there are some concerns with the science quality of an observation. The message can be informing of an effect with no significant impact on the science products (INFO), with potential minor impact on the science quality (WARNING) or major impact on the science quality (SEVERE). Examples of INFO messages are when some QC parameters are slightly over the empirical thresholds. Examples of WARNING messages are when there is potentially a significant pointing offset or some pipeline module is not optimally correcting some effects due to some peculiar conditions (e.g. the instrument is too cold or too warm). SEVERE messages are usually for observations that are impossible to calibrate because non-standard instrument settings were used, as well as for spectroscopy observations known to suffer significant pointing offsets. In some cases, expert processing of the observation could remedy the quality problem, and these are provided as Highly Processed Data Products (HPDP). This is indicated in the QC Summary message.

8.3 HSA Archive File for SPIRE Observations

Anyone can browse the HSA but to download any data you have to be already registered as *Herschel* user, and to login with your *Herschel* user name and password. The full SPIRE observation context (or a subset at a particular processing level) can be downloaded from the *Herschel* Science Archive. When you select and add observations to the "shopping basket" then you can submit a request to get the data. When the data are ready to download, an e-mail with an ftp link to the tar file will be provided in the message. Note that the e-mail will be sent to the one used to register as a *Herschel* user, so it is important to keep it up to date.

The HSA archive file matches exactly the structure of the SPIRE observation context as described in the SPIRE Data Reduction Guide, Chapter 4.

Note that the relevant FITS file names in the tar file are not "human readable". But the names of the higher level folders should match the corresponding context.

For example, the Photometer maps, calibrated for extended emission (see Section 5.5) are under level2/extdPxW and the point-source calibrated ones (see Section 5.4) under level2/psrcPxW, where

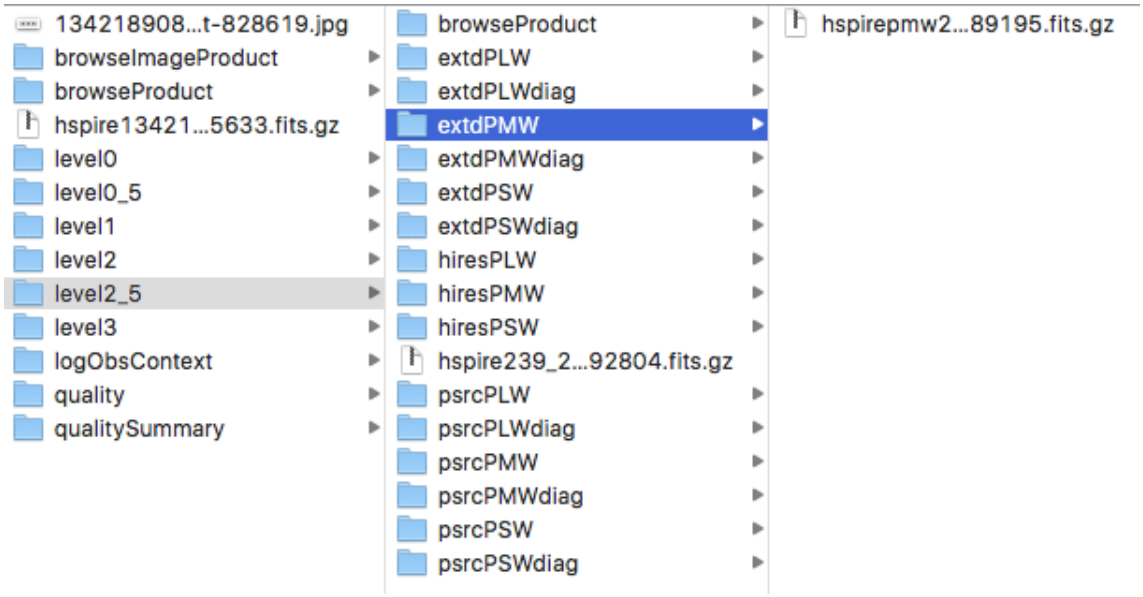

Figure 8.3: The folder structure and content of an HSA tar file for SPIRE photometer observation.

"x" is S/M/L for 250/350/500 μm correspondingly. A screenshot of the structure of a Photometer observations is shown in Figure 8.3.

The Spectrometer products are available in a similar folder structure, with the exception that there are no Level 2.5 or Level 3 folders as there are no such contexts for the FTS. An example is shown in Figure 8.4.

Detailed description of the SPIRE products and the FITS file structure are available in the SPIRE Products Explained document.

8.4 HSA Default Products for SPIRE Observations

The Default Products (also known as Standalone Browse Products, SBPs) provide quick access to the highest level standard pipeline processing FITS files. Access to the SBPs is provided through a right-click on the HSA postcard image for a particular observation. Only a subset of the Level-2 or above products are provided as SBPs. The SPIRE SBPs can be used for scientific data analysis, taking into account their characteristics, which are listed in Table 8.1:

When the default products do not match the science case, e.g. photometer point-source calibrated maps are needed, then the relevant files at Level-2 or above (or the full observation context) can be downloaded from the HSA.

8.5 Which products should I use for data analysis?

If the Standalone Browse Products match the science case, as explained in Section 8.4, then this is the most straightforward way to get the best science grade data. If this is not the case, then in most cases, Level-2 or above are of a sufficient scientific quality to be used as a starting point for any further data

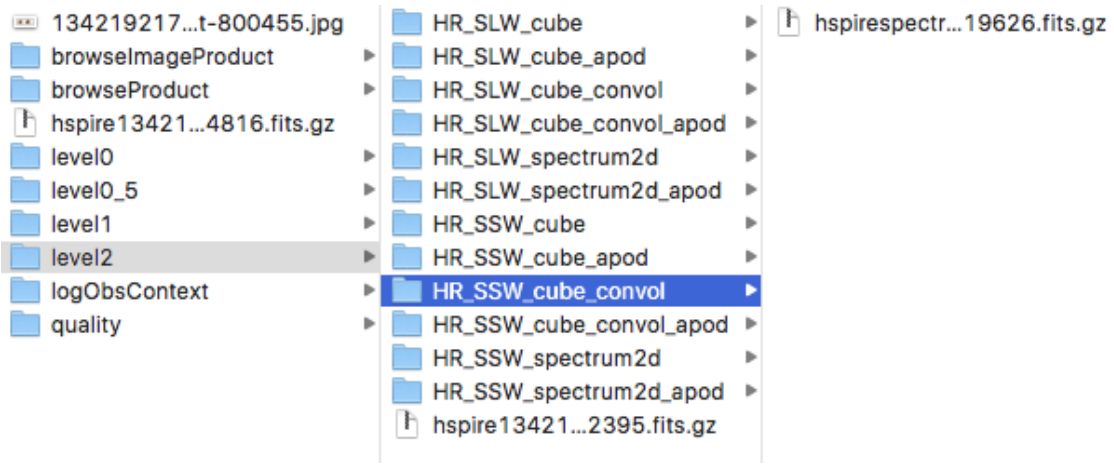

Figure 8.4: The folder structure and content of an HSA tar file for SPIRE spectrometer HR mapping observation.

Table 8.1: SPIRE Default Products per observing mode. The pattern in the FITS file is also shown, '*' is a wildcard. Note that only one of the possibilities is available in the SBP archive file, i.e. cannot have both *_25pxmp_* and *_20pxmp_*.

Mode	FITS file regex	SBP selection
SPIRE Photometry	*_25pxmp_* *_20pxmp_* *_20ssopmp_*	Level-2 maps processed with the version of the pipeline for absolute *extended source calibrated* maps in MJy/sr. When there are overlapping SPIRE single scan direction maps or the SPIRE component of SPIRE/PACS parallel mode observations, then the SBPs are the Level-2.5 products. For Solar System Objects, the SBPs are Level-2 *point-source calibrated* maps in Jy/beam, corrected for the proper motion of the object.
SPIRE Spectroscopy	*_20spss_* *_20sc_*	For observations in sparse mode the Level-2 *point-source calibrated* spectra for the central detectors. For spectral maps the Level-2 convolution projection spectral cubes, using *extended source calibration*.

analysis (e.g. photometry, line flux measurements, etc). The exceptions are Level-3 maps, which are a mosaic of individual Level-2 maps. The individual maps are already binned on sky pixels, moreover they are not corrected for astrometry offsets or registered to have the same relative astrometry. Hence, the combined Level-3 map may not be of a sufficient science quality. In Table 8.2 we summarise the final products and where they can be found in the HSA tar file.

Table 8.2: The high level folders in the *Herschel* Science Archive file. Each of the folders should contain one multi-extension compressed FITS file. For the photometer, the structure is also applicable for Level-2.5 and Level-3, when available. For the Spectrometer, only the high resolution (HR) case is shown, replace "HR" with "LR" for observations performed in low resolution. There will be both the "HR" and the "LR" variants for the observations with the "H+LR" mode. Similarly, only an "unapodized" example is given, if the smoothed (apodized) spectra are needed then use "apodized" instead.

	Photometer	
Level 2	psrcPxW	Point source calibrated maps, in units of Jy/beam
	extdPxW	Extended source calibrated maps, with *Planck* zero level offset, in units of MJy/sr
	ssoPxW	Point source calibrated maps in the moving object rest-frame
	hiresPxW	Extended source calibrated hi-resolution maps
	Spectrometer, sparse mode	
Level 2	Point_0_Jiggle_0_HR/ unapodized_spectrum	Extended source calibrated spectra per FTS detector, in units of $\mathrm{W\,m^{-2}\,Hz^{-1}\,sr^{-1}}$
Level 2	HR_unapodized_spectrum	Point source calibrated spectra per detector, in units of Jy
	Spectrometer, mapping mode	
Level 2	Point_0_Jiggle_x_HR/ unapodized_spectrum	Extended source calibrated spectra per FTS detector per jiggle position "x", in units of $\mathrm{W\,m^{-2}\,Hz^{-1}\,sr^{-1}}$. "x" can be from 0 to 3 for intermediate sampling maps and from 0 to 15 for fully sampled maps.
Level 2	HR_SxW_unapodized_spectrum	SxW spectral cubes, in units of $\mathrm{W\,m^{-2}\,Hz^{-1}\,sr^{-1}}$. "x" can be "S" for the spectral cube from the short-wavelength array (197–313 μm) or "L" for the long-wavelength array cube (303–671 μm).

8.6 User reprocessing and further data analysis of SPIRE data

User reprocessing scripts are available in HIPE, and these are explained in greater detail in the SPIRE Data Reduction Guide.

In addition to the reprocessing user pipelines, there are a number of utility scripts in HIPE which are useful for a number of further data analysis steps, like astrometry correction for the timeline data and the subsequent map making, removal of background from spectra, correction of the spectra for semi-extended sources, etc. Please consult the SPIRE Data Reduction Guide.

8.7 Access to calibration files

Each SPIRE observation context downloaded from the HSA also contains the calibration tree and some auxiliary products. The calibration tree in an observation context only contains calibration files that are relevant for the particular sub-instrument, i.e. for a Spectrometer observation only the calibration files with relevance for the Spectrometer pipeline or data analysis are available. A standalone calibration tree can also be downloaded from the Herschel Science Centre[1] as a java archive file (with extension jar). The jar archives are similar to tar archive and can be un-archived with a similar command: for example, `jar xvf spire_cal_14_3`, which will extract the individual calibration products in a folder structure like this: `herschel/spire/ia/cal/data/SCal/`. The products are FITS files, tables or images, that are available in the calibration context in the tar file from the HSA, which in general can be opened with any FITS viewer (topcat, fv, ds9, Aladin, etc). The FITS files have all the relevant metadata keywords with descriptions and the table columns have the correct units, so these should be straightforward to use. Most of the calibration files are only useful for the low level pipeline processing (see e.g. the SPIRE Data Reduction Guide.

All calibration products and and their descriptions are listed in the SPIRE Calibration Products Table.

[1] The latest standalone SPIRE calibration tree is available at
ftp://ftp.sciops.esa.int/pub/hsc-calibration/latest_cal_tree/

Bibliography

Ade, P. et al., 2006, *Proc. SPIE* 6275, 62750U

Audley, D. et al., 2007, *in Proc. Exploring the Cosmic Frontier, Astrophysical Instruments for the 21st Century*, Springer-Verlag, p. 45

Aumann, H. et al., 1990, *A maximum correlation method for image construction of IRAS survey data*, AJ , 99, 1674

Bendo G. et al, 2013, *Flux calibration of the Herschel-SPIRE photometer*, MNRAS, 433, 3062

Benielli D., et al., 2014, *Herschel SPIRE FTS spectral mapping calibration*, Experimental Astronomy, 37, 357

Caldwell M., Swinyard B., Richards A., & Dohlen K., 2000, Proc. SPIE, 4013, 210

Cantalupo C.M., Borrill J.D., Jaffe A.H., Kisner T.S., Stompor R., 2010, *MADmap: A Massively Parallel Maximum Likelihood Cosmic Microwave Background Map-maker*, ApJS, 187, 212

Chattopadhyay, G. et al, 2003, IEEE. Trans. Microwave Theory and Techniques, 51, 2139

Decin, L. & Eriksson, K., 2007, *Theoretical Model Atmosphere Spectra Used for the Calibration of Infrared Instruments*, A&A, 472, 1041

De Graauw, Th. et al., 2010, *The Herschel-Heterodyne Instrument for the Far-Infrared (HIFI)*, A&A, 518, L6

Dohlen, K. et al., 2000, Proc. SPIE 4013, 119

Dowell, D. et al., 2003, Proc. SPIE, 4855, 73

Duband, L. et al., 1998, Cryogenics, 48, 95

Fischer, J. et al., 2004, *Cryogenic far-infrared laser absorptivity measurements of the Herschel Space Observatory telescope mirror coatings*, Applied Optics, 43, 3765

Fulton, T. et al., 2008, Proc. SPIE, Vol. 7010, 70102T

Fulton, T., 2012, *SPIRE Spectrometer pipeline description*, SPIRE-BSS-DOC-002966, Issue 4.0.1

Fulton, T. et al., 2014, *Herschel SPIRE FTS relative spectral response calibration*, Experimental Astronomy, 37, 381

Fulton, T. et al., 2015, *The data processing pipeline for the Herschel SPIRE Fourier Transform Spectrometer*, MNRAS, submitted

Griffin, M. J., 2007, *Sensitivity of the SPIRE Detectors to Operating Parameters*, SPIRE-UCF-DOC-002901

Griffin, M. J., 2008, *The SPIRE Analogue Signal Chain and Photometer Detector Data Processing Pipeline*, SPIRE-UCF-DOC-002890, Issue 6, November 2008

Griffin, M.J. & Orton, G.S., 1993, *The Near Millimeter Brightness Temperature Spectra of Uranus and Neptune*, Icarus, 105, 537

Griffin, M.J. et al., 2002, Applied Optics, 31, 6543

Griffin, M.J. et al., 2006, *Herschel-SPIRE: Design, Performance, and Scientific Capabilities*, Proc. of SPIE 6265, 7

Griffin, M.J. et al., 2010, *The Herschel-SPIRE Instrument and its in-flight performance*, A&A, 518, L3

Griffin, M.J. et al., 2013, *Flux calibration of broad-band far-infrared and submillimetre photometric instruments: theory and application to Herschel-SPIRE*, MNRAS, 434, 992

Hargrave, P. et al., 2006, Proc. SPIE 6275, 627513

Hartman R.C. et al.1996, *Simultaneous Multiwavelength Spectrum and Variability of 3C 279 from* 10^9 *to* 10^{24} *Hz*, ApJ, 461, 698

Hildebrand, R., 1983, *The Determination of Cloud Masses and Dust Characteristics from Submillimetre Thermal Emission*, QJRAS, 24, 267

Hildebrand, R. et al., 1985, *Far-infrared and Submillimeter Brightness Temperatures of the Giant Planets*, Icarus, 64, 64

Hopwood R., et al., 2014, *Herschel SPIRE FTS telescope model correction*, Experimental Astronomy, 37, 195

Hopwood R., et al., 2015, *Systematic characterisation of the Herschel SPIRE Fourier Transform Spectrometer*, MNRAS, in press (arXiv:1502.05717).

Jarrett, T. et al., 2012, *Constructing a WISE High Resolution Galaxy Atlas*, AJ , 144, 68

Lebofsky, L.A. et al., 1986 *A Refined Standard Thermal Model for Asteroids Based on Observations of 1 Ceres and 2 Pallas*, Icarus, 68, 239

Lindal, G.F., et al., 1987, *The Atmosphere of Uranus: Results of Radio Occultation Measurements with Voyager 2*, J. Geophys. Res., 92, 14987

Lindal, G., 1992, *The Atmosphere of Neptune: an Analysis of Radio Occultation Data Acquired with Voyager 2*, Astron. J., 103, 967

Lu N., et al., 2014, *Herschel SPIRE Fourier Transform Spectrometer: calibration of its bright-source mode*, Experimental Astronomy, 37, 239

Lucy, L. B. 1974, AJ, 79, 745

Mandel, L. & Wolf, E., 1995, *Optical coherence and quantum optics*, CUP

Mather, J.C., 1982, *Bolometer noise: nonequilibrium theory*, Applied Optics 21, 1125

Makiwa G., et al., 2013, *Beam profile for the Herschel-SPIRE Fourier transform spectrometer*, Applied Optics 52, 3864

Marchili N. et al., *Calibration of Herschel SPIRE FTS observations at different spectral resolutions*, in preparation

Marth, A., 1897, *On the Apparent Disc and on the Shadow of an Ellipsoid*, MNRAS, 57, 442

Moreno, R., 1998 PhD Thesis, Université Paris VI.

Moreno, R., *Neptune and Uranus planetary brightness temperature tabulation*, available from ESA *Herschel* Science Centre ftp://ftp.sciops.esa.int/pub/hsc-calibration, 2010

Müller, Th. & Lagerros, J.S.V., 2002, *Asteroids as Calibration Standards in the Thermal Infrared for Space Observatories*, A&A, 381, 324

Müller, Th. et al., 2014, *Herschel celestial calibration sources*, Experimental Astronomy, 37, 253

Murphy J.A.& Padman R., 1991, Infrared Physics, 31, 291

Müller, Th, 2009, *Asteroid Calibration Quality Information for COP and Early PV*, 8 May 2009, Asteroid_quality_TM_08052009.pdf (available from ESA *Herschel* Science Centre)

Naylor, D. & Tahic, K., 2007, J. Opt. Soc. Am. A. 24, 3644

Naylor, D. et al., 2010, *In-orbit performance of the Herschel/SPIRE imaging Fourier transform spectrometer*, SPIE, 7731, 29

Nguyen, H., et al., 2010, *HerMES: The SPIRE confusion limit*, A&A, 518, L5

Oliver, S., et al., 2012, *The Herschel Multi-tiered Extragalactic Survey: HerMES*, MNRAS, 424, 1614

Orton, G.S., et al., 1986, *Submillimeter and Millimeter Observations of Uranus and Neptune*, Icarus, 67, 289

Orton, G.S., et al., 2014, *Mid-infrared spectroscopy of Uranus from the Spitzer Infrared Spectrometer: 1. Determination of the mean temperature structure of the upper troposphere and stratosphere*, Icarus, 243, 494

Pearson C., et al., 2014, *SPIRE point source photometry: within the Herschel interactive processing environment (HIPE)*, Experimental Astronomy, 37, 175

Pilbratt, G. et al., 2010, *Herschel Space Observatory – An ESA facility for far-infrared and submillimeter astronomy*, A&A, 518, L1

Pisano, G. et al., 2005, Applied Optics IP, 44, 3208

Planck Collaboration VIII, 2014, *Planck 2013 results. VIII. HFI photometric calibration and mapmaking*, A&A, 571, 8

Poglitch, A. et al., 2010, *The Photodetector Array Camera and Spectrometer (PACS) on the Herschel Space Observatory*, A&A, 518, L2

Richardson, W. H. 1972, Journal of the Optical Society of America (1917-1983), 62, 55

Rownd, B. et al., 2003, *Design and performance of feedhorn-coupled arrays coupled to submillimeter bolometers for the SPIRE instrument aboard the Herschel Space Observatory*, Proc. SPIE 4855, 510

Sandell, G., Jessop, N., and Jenness, 2001, *SCUBA Map Reduction Cookbook*, http://www.starlink.rl.ac.uk/star/docs/sc11.htx/sc11.html

Sudiwala, R.V, Griffin, M.J. and Woodcraft, A.L., 2002, *Thermal modelling and characterisation of semiconductor bolometers*, Int. Journal of Infrared and mm Waves, 23, 545

Swinyard, B. et al., 2003, Proc. SPIE 4850, 698

Swinyard, B. M. et al., 2010, *In-flight calibration of the Herschel-SPIRE instrument*, A&A, 518, L4

Swinyard, B. M. et al., 2014, *Calibration of the Herschel-SPIRE Fourier-Transform Spectrometer*, MNRAS 440, 3658

Teanby, N. A. & Irwin, P. G. J., 2013, *An External Origin for Carbon Monoxide on Uranus from Herschel/SPIRE?*, ApJ, 775, 49

Turner, A.D. et al., 2001, *Si_3N_4 micromesh bolometer array for sub-millimeter astrophysics*, Applied Optics 40, 4921

Ulich, B.L. & Haas, R.W., 1976, *Absolute Calibration of Millimeter-Wavelength Spectral Lines*, ApJS, 30, 247

Valtchanov I., et al., 2016, *Extended source calibration for the Herschel-SPIRE FTS*, in preparation

Wu R., et al., 2013, *Observing extended sources with the Herschel SPIRE Fourier Transform Spectrometer*, A&A, 556, 116

Xu K., et al., 2014, *SPIRE Map-Making Test Report*, arXiv:1401.2109.